Charles University in Prague
Faculty of Mathematics and Physics

**DOCTORAL THESIS**

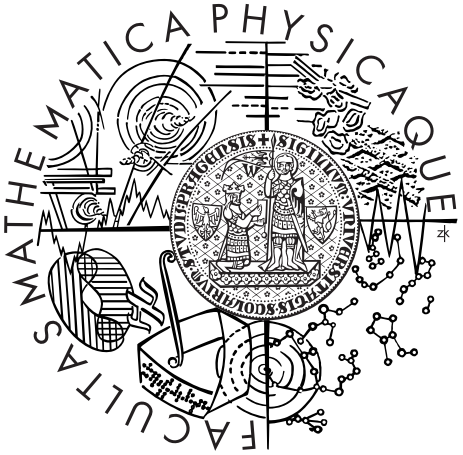


Vjačeslav Sochora

# Astrophysical processes near compact objects: studying extremal energy shifts from accretion rings

Academy of Sciences of the Czech Republic
Astronomical Institute

| | |
|---|---|
| Supervisor of the doctoral thesis: | doc. RNDr. Vladimír Karas, DrSc. |
| Study programme: | Physics |
| Specialization: | Theoretical physics, astronomy and astrophysics |

Prague 2013

I would like to thank my supervisor Vladimír Karas, colleagues Jiří Svoboda and Michal Dovčiak for their ideas, advices and cooperation. Also, I would like to thank Zuzana Hrbáčková for her support.

I declare that I carried out this doctoral thesis independently, and only with the cited sources, literature and other professional sources.

I understand that my work relates to the rights and obligations under the Act No. 121/2000 Coll., the Copyright Act, as amended, in particular the fact that the Charles University in Prague has the right to conclude a license agreement on the use of this work as a school work pursuant to Section 60 paragraph 1 of the Copyright Act.

In Prague, 2 July 2013 .....

Název práce: Astrofyzikální procesy v blízkosti kompaktních objektů: studium extremálních posuvů energie z akrečních prstenců

Autor: Vjačeslav Sochora

Pracoviště: Astronomický ústav AV ČR

Vedoucí disertační práce: doc. RNDr. Vladimír Karas, DrSc., Astronomický ústav AV ČR

Abstrakt: Rentgenové záření z vnitřních oblastí akrečního disku okolo černých děr poskytuje velké množství informací o hmotě v extrémních podmínkách. Spektrální profil záření z úzkého, kruhového prstence má charakteristický tvar s dvěma maximy. Červený a modrý vrchol profilu leží blízko extremálních hodnot energetického posuvu čáry. Popisujeme užitečný postup výpočtu extremálních energetických posuvů v režimu silné gravitace. Diskutujeme, zda radiální struktura emise disku může být rekonstruována užitím extrémních energetických posuvů jednotlivých prstenců. Za tímto účelem simulujeme umělá data z jasného galaktického jádra a ukazujeme, že požadované citlivosti a energetického rozlišení může být dosaženo s navrženou misí LOFT.

Klíčová slova: fyzika černých děr, akreční disky, galaktická jádra

Title: Astrophysical processes near compact objects: studying extremal energy shifts from accretion rings

Author: Vjačeslav Sochora

Department: Academy of Sciences of the Czech Republic, Astronomical Institute

Supervisor: doc. RNDr. Vladimír Karas, DrSc.; Academy of Sciences of the Czech Republic, Astronomical Institute

Abstract: The X-ray emission from inner regions of an accretion disk around black holes provides wealth of information about matter in extreme conditions. A spectral profile of radiation from a narrow circular ring has a characteristic double-horn profile. Red and blue peaks of the profile are close to the extremal values of the energy shift. We describe a useful approach to calculate the extremal energy shifts in the regime of strong gravity. We discuss if the radial structure of the disk emission could be reconstructed using extremal energy shifts of the individual rings. For this purpose, we simulate artificial data from a bright active galactic nucleus and show that the required sensitivity and energy resolution can be reached with the proposed LOFT mission.

Keywords: black hole physics, accretion disks, galactic nuclei

# Acknowledgments

I acknowledge the Astronomical Institute of the Academy of Sciences of the Czech Republic for providing me a stimulating work environment and appropriate computational equipment.

Part of the work was supported by the Czech Science Foundation and Deutsche Forschungsgemeinschaft collaboration project (GACR-DFG 13-00070J), the European Union Seventh Framework Programme under the grant agreement No. 312789, the student research grant of the Charles University (SVV-267301), and grant GAUK 621912 (116-10/253158).

# Contents

# Chapter 1

# Introduction

The thesis is built on the research work that was done during my PhD studies, and on the obtained results. Most of the results were published in the papers Karas & Sochora (2010), and Sochora et al. (2011), and in several proceedings Sochora & Karas (2010a), Sochora & Karas (2010b).

This work is divided in several parts, where the reader will be acquainted with the progress of the research and with the obtained results. The introduction contains motivation and goals of the thesis and the reader can gain the idea about the studied problem. It mainly discusses the relativistic iron line, its properties, and the idea of relativistic lines as a superposition of ring profiles. Eventually, the LOFT and Athena+ missions are presented as proposals that could have necessary capability to observer the ring structures in the relativistic profile. For brevity, we omitted the whole physics of black hole accretion from the introduction, because we expect the reader to be familiar with it or find this information in various publications (Shapiro & Teukolsky, 1983; Kato et al., 1998).

The second chapter is a brief introduction to photon propagation in Kerr metric and the mathematical apparatus that is necessary for calculations presented in next chapters. In case of interest for more information about Kerr metric or the whole mathematical theory of black holes, we refer to the book by Chandrasekhar (2004).

Next three chapters present main results of the thesis. The first one speaks about Carter's equations in the form of the elliptic integrals and their solution in a graphical form. The second one shows the connection between Carter's equations and extremal energy shifts, and how the resultant values were calculated. The last chapter from these three ones presents a model spectrum and a discussion about a reconstruction of parameters from this spectrum.

Last two chapters are the conclusion and view of future perspective. We can also find an appendix at the end of the thesis. The appendix contains all equations needed to calculate the extremal energy shifts and it is an important part of the work by that the reader can reconstruct the procedure to obtain the extremal energy shifts as described in appropriate chapters.

## 1.1 Relativistic spectral lines from accretion rings and disks

Emission from inner regions of accretion disks around black holes in both, black hole binaries and active galactic nuclei (AGNs), provides wealth of information about matter in extreme conditions. It is emitted as primary X-rays with an exponential cutoff at high energy ($E \approx 300$ keV) from accretion disk corona in active or flaring regions, and as a secondary (reprocessed) component. The soft optical/UV (in case of AGNs) or soft X-ray (in case of black hole binaries) disk photons are comptonized by the hot corona (Thorne & Price, 1975; Haardt & Maraschi, 1991) (optically thin accretion disk atmosphere with hot relativistic electrons that are possibly heated up by the magnetic dissipation processes; Galeev et al., 1979; Haardt et al., 1994) and the power-law X-ray spectrum is produced. These photons escape directly to an observer. The X-ray reflection and iron line fluorescence are understood as a case when the hard X-ray (power-law) continuum illuminates the gas in the disk. Once a hard X-ray photon enters the disk, possible interactions occur: Compton scattering by free or bound electrons, photoelectric absorption followed by fluorescent line emission, or photoelectric absorption followed by Auger de-excitation. The reprocessed spectrum is characterized mainly by the Compton hump at $E \geq 10$ keV and the fluorescent iron line at $E \geq 6 - 7$ keV.

Due to the energy dependence of photoelectric absorption, incident soft X-rays are mostly absorbed, whereas hard photons are rarely absorbed and tend to Compton scatter back out of the disk. Figs. 1.1 and 1.2 show the results of a Monte Carlo calculation where we can see that the iron K$\alpha$ line at 6.4 keV is the strongest of these lines.

These processes are thought to be situated near a central black hole, no more than few tens gravitational radii from the event horizon, giving rise to the relativistic effects in 6–7 keV iron line complex and the underlying continuum. The standard scheme of accretion disks (Novikov & Thorne, 1973; Page & Thorne, 1974) captures the main properties of accreting black holes surprisingly well, nevertheless, the model omits some important aspects. In particular, the radial profile of the source intrinsic emissivity is represented by a smooth function (decaying as a power law $\propto r^{-3}$ at large distance), while the realistic profile is likely to be more complicated.

Different approaches have been pursued in order to understand how accretion disk X-ray spectra are formed. Generally, these include the investigations of accretion disk instabilities as well as the interpretation of spectra to constrain the model parameters (such as the black hole spin, the source orientation, and the location and size of the accretion disk), and to determine the radial profile of accretion disk emissivity (Fabian et al., 2004). Recently, Wilkins & Fabian (2011) discussed an interesting approach to the inversion problem of determining the radial emissivity bulk profile of the relativistic broad iron line in Seyfert galaxy 1H 0707-495.

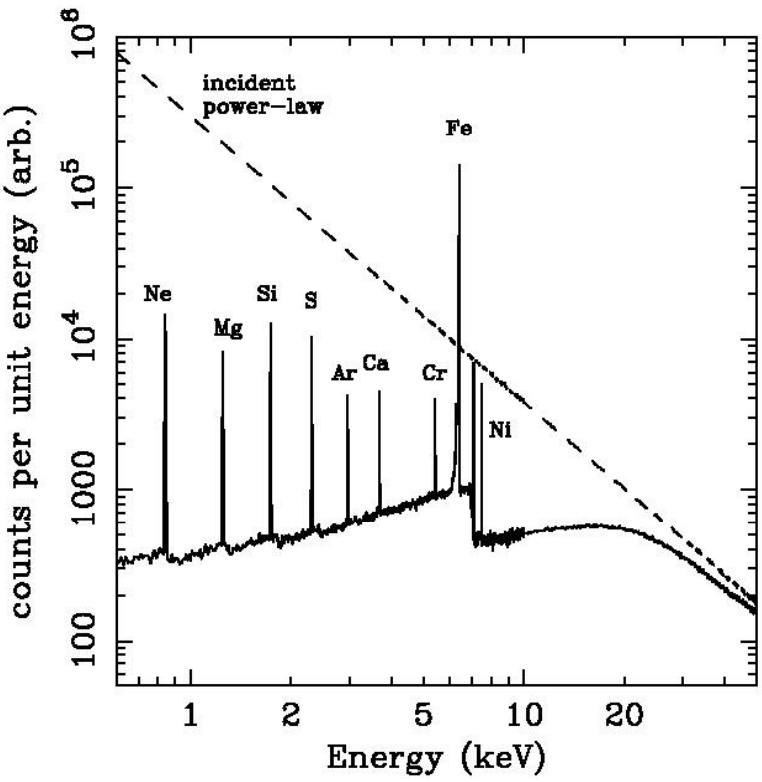


Figure 1.1: X-ray reflection from an illuminated slab. Dashed line shows the incident continuum and solid line the reflected spectrum (integrated over all angles). Monte Carlo simulation from Reynolds (1996).

Relativistic spectral line of iron, broadened and skewed by fast orbital motion and redshifted by strong gravitational field, has been used to constrain the parameters of the black hole, both in active galactic nuclei (Fabian et al., 2000; Reynolds & Nowak, 2003; Miller, 2007) and Galactic black holes (Miller et al., 2002; McClintock & Remillard, 2006). The first candidates of black holes were binary systems. Today, these types of systems are classified into two classes: High-Mass (HMXBs) and Low-Mas X-ray Binaries (LMXBs). Both classes contain a compact object and an orbiting star as a companion. The accretion is formed by a strong stellar wind from the companion star or it is created by Roche lobe over-flow. HMXBs are very young objects ($< 10^7$ years) with luminosities $\sim 10^{37}$ erg.s$^{-1}$ and the first established black hole binary was Cygnus X-1 (Webster & Murdin, 1972; Bolton, 1972). LMXBs belong to old systems ($> 10^9$ years) without a strong stellar wind. Fig. 1.3 represents a schematic view on a binary system with a compact object surrounded by an accretion disk, and a companion that is a source of an accreting matter. AGNs are systems with super-massive black holes (SMBHs) in the dynamical centers of galaxies. They are divided in many groups (quasar, Seyfert galaxy, Broad Line Region Galaxy and other, see fig. 1.4). All have the same intrinsic structure but are viewed under a different inclination.

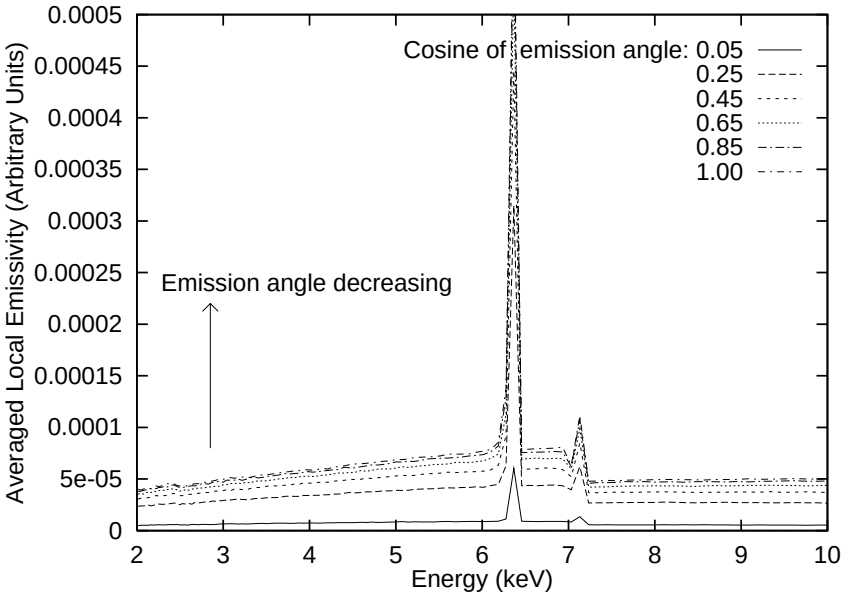


Figure 1.2: Examples of local spectra $F(E)$ around the iron line rest energy, $E_0 = 6.4$ keV. $F$ represents the radiation flux averaged over the incident angle of the photons from the primary source. Taken from Martocchia et al. (2000).

For more information, we kindly refer the reader to references above.

The iron K$\alpha$ line is an intrinsically narrow line, but the observed profile is shaped by the effects of Doppler shifts and gravitational redshifting. The special relativistic beaming enhances the blue peak of the line for each radius. The transverse Doppler effect and gravitational redshifting shift the contribution from each radius to a lower energy. Fig. 1.5 shows us the behavior of the iron line on spin of a black hole, inclination of an observer, and an emitting radius. The blue peak of the line is a strong function of the inclination of the disk if the spin and emitting radius are fixed, and provides a way to measure the inclination of the disk. The red wing of the profile is a sensitive function of the inner radius of the emitting ring or belt. The spectral line moves to lower energies when the emitting radius is closer to the black hole.

Zakharov et al. (2004) described a procedure to estimate an upper limit of the magnetic fields in regions from which X-ray photons are emitted. These authors then simulated typical profiles of the iron K$\alpha$ line in the presence of magnetic field and compared them with observational data in the framework of the widely accepted accretion disk model. A better resolution of the blue peak structure of iron K$\alpha$ line will allow to evaluate the magnetic fields with higher accuracy.

During recent years, much discussions have revolved round the question of how close to the innermost stable circular orbit (ISCO[1], Misner et al., 1973) an

[1]i.e., $r_{\rm ISCO} = 6\,r_{\rm g}$ for Schwarzschild black hole, and $r_{\rm ISCO} = 1\,r_{\rm g}$ for an extreme Kerr black hole, gravitational radius $r_{\rm g} \equiv GM/c^2 \doteq 1.48 \times 10^{12} M_7$ cm with $M_7$ being the mass of the

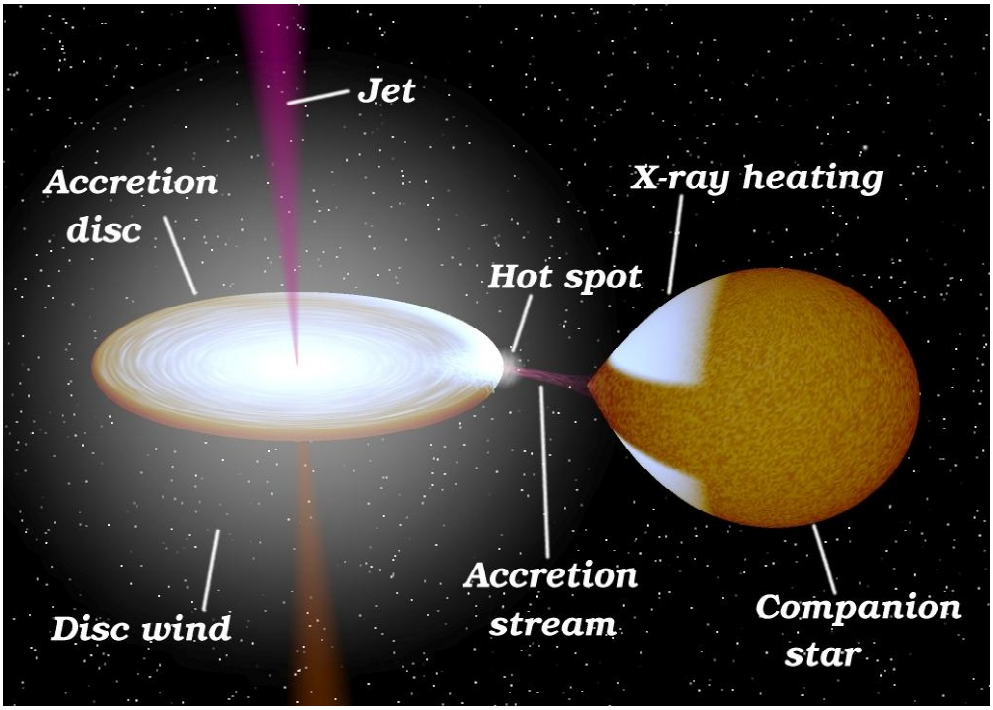


Figure 1.3: A standard picture of a binary system with a compact object and its companion. The companion is a star that fills its Roche lobe and is a source of an accreting matter around the compact object. (An artist impression of an X-ray binary by R. Hynes)

accretion disk extends, whether the line is produced all the way down to the inner edge, and if the emission from an accretion disk can be approximated by a smooth radial profile.

Reynolds & Begelman (1997) point out that there could be some non-negligible contribution to the reflection line originating even below ISCO. This idea has been put in a more specific context of magnetized accretion flows, as discussed e.g. by Beckwith et al. (2008). On the other hand, Reynolds & Fabian (2008) explored the flow properties close to the black hole and they demonstrated that the presence of ISCO leaves a strong imprint on the X-ray reflection spectrum of the accretion disk due to the rapid increase in ionization parameter. Furthermore, Martocchia et al. (2002a) conclude, on the basis of the X-ray iron line modeling in GRS 1915+105 microquasar that the line production is limited to the region above the ISCO. Also Svoboda et al. (2010) found a convincing case for a disk being truncated rather far above the ISCO (this time in a Seyfert 1.5 galaxy IRAS 05078+1626), whereas Turner et al. (2010) suggest that a persistent 5.44 keV feature exhibited by another Seyfert 1 AGN, NGC 4051, could originate from a preferred radius of the order of a few ISCO.

The Seyfert 1 galaxy MCG–6-30-15 is a unique source in which the broad and

supermassive black hole in units of $10^7 M_\odot$, also called the marginally stable orbit, $r = r_{\rm ms}$.

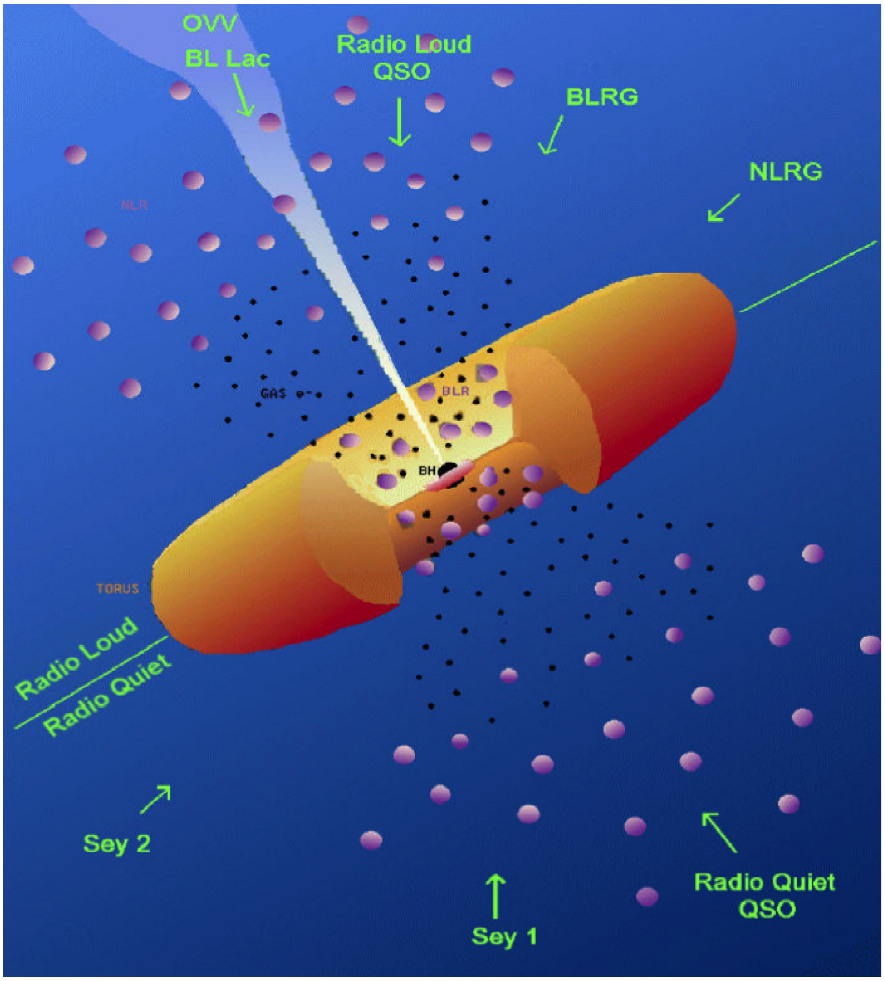


Figure 1.4: A schematic picture of AGN (Urry & Padovani, 1995). The view angle of an observer define the type of AGN. (QSO = quasar, Sey = Seyfert galaxy, BLRG = Broad Line Region Galaxy, NLRG = Narrow Line Region Galaxy, OVV = Optically Violent Variables, BL Lac = BL Lac objects.)

skewed iron line is very prominent and was first reported with ASCA observation (Tanaka et al., 1995; Iwasawa et al., 1996). This has lead to the wide acceptance of the model with an accreting black hole in the nucleus. The original results were largely confirmed by extending the energy interval of the continuum to the Beppo-SAX range (Guainazzi et al., 1999; Martocchia et al., 2000). Furthermore, XMM-Newton unprecedented sensitivity allowed to constrain the model parameters with better confidence (Fabian et al., 2002; Fabian & Vaughan, 2003; Martocchia et al., 2002a; Dovčiak et al., 2004a; Brenneman & Reynolds, 2006).

Despite the progress, several factors contribute to uncertainties in spectral line fitting and interpretation: (i) unknown distribution of inhomogeneities and patches that must be present in the accretion flow on small scales; (ii) transient and random obscuration of the disk by clouds lying above it or inhomogeneous

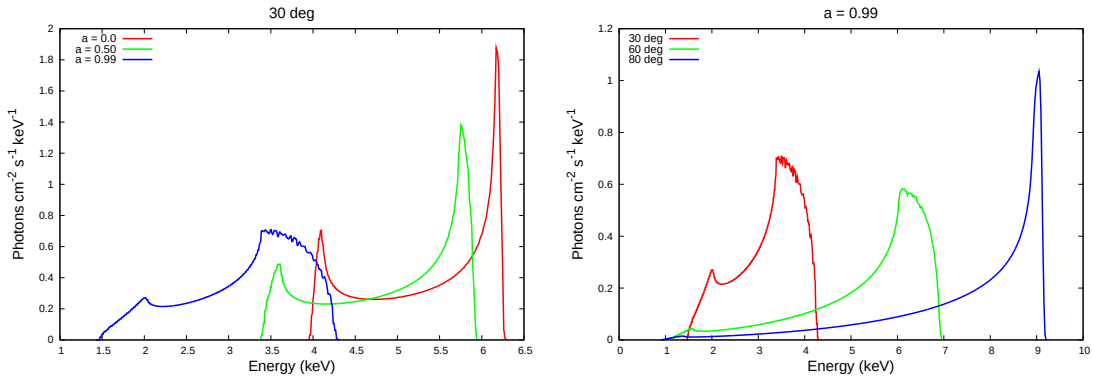


Figure 1.5: Theoretical profile of a relativistic spectral line from an accretion ring, influenced by fast orbital motion and gravitational shift of energy. Left panel: the profile of K$\alpha$ line for three different spins and corresponding radii ($a = 0.0$, $r_{\rm em} = 7\ r_{\rm g}$; $a = 0.5$, $r_{\rm em} = 5\ r_{\rm g}$; $a = 0.99$, $r_{\rm em} = 2\ r_{\rm g}$), the inclination is 30 deg. Right panel: the profile of iron line for $a = 0.99$ and $r_{\rm em} = 2\ r_{\rm g}$ with changing inclination. In both graphs the width of the emitting ring is $\Delta r = 0.5\ r_{\rm g}$.

winds in the disk corona; (iii) light-bending effects, which depend in a complicated manner on the black-hole spin and the source orientation. It is very likely that the mentioned effects share some part of responsibility for unmodeled curvature of the broad line profile, however, their impact cannot be disentangled with the limited quality of the current X-ray spectra.

In some cases a small but statistically significant "bump" occurs superposed on the red wing of the broad line. An example is shown in fig. 1.6. Understanding the origin of such features is essential for proper fitting and accuracy of the model parameters. Dovčiak et al. (2004a) noticed the presence of this excess and suggested that it may arise due to enhance emissivity of the line (above the level prescribed by the standard disk model) at very small radii very near the horizon. Possibility of such an increased emission was previously discussed in somewhat different context by Fabian et al. (2002, sec. 3.4), and it is also consistent with the Wilms et al. (2001) scheme, according to which the electromagnetic processes could be responsible for such an enhancement arising at small radii.

This non-standard emissivity profile can be modeled in terms of a broken radial power-law dependence with a certain value of break radius, $r_{\rm b}$, where the radial power-law index changes. The double power-law emissivity arises naturally in the lamp-post model (Martocchia et al., 2000) in which the disk irradiation and the resulting Fe K reflection are substantially anisotropic owing to fast orbital motion in the inner ring. Unfortunately, it has been impossible to confirm or reject this scenario because the dual-ring model has obviously additional parameters, so the model prediction for time averaged spectrum is not unique.

Here we notice that spectro-polarimetric information in X-rays would be very helpful to reveal the origin of these features. The reason for superiority of such approach is that the observed polarization angle is affected as the photons pass

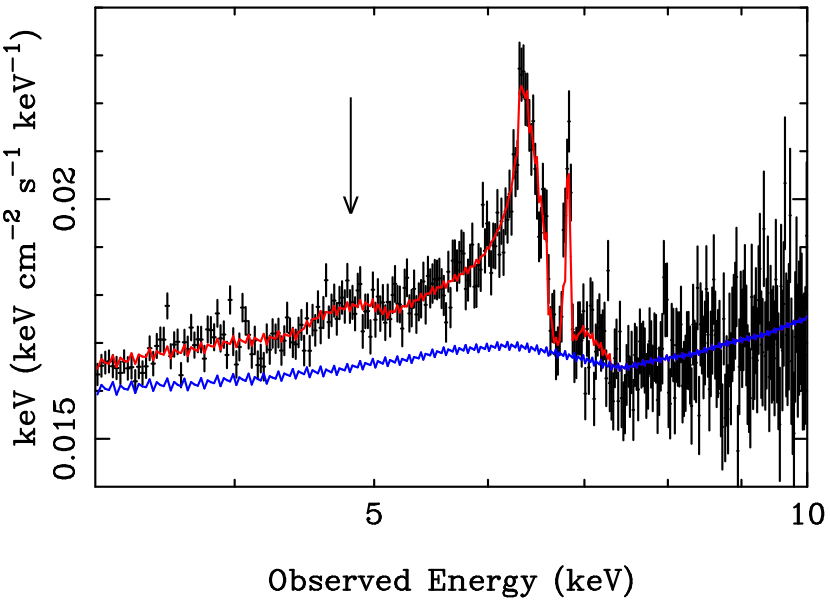


Figure 1.6: XMM–Newton spectrum of MCG–6-30-15 in which the Fe K line originates from an accretion disk with the radial emissivity representing a dual-ring (Dovčiak et al., 2004a). Notice a small excess (indicated by arrow) at about $\sim 1\%$ level of the profile around $E \sim 4.8$ keV. This model fits the residuals which remain unmodeled with a more simple scheme (such as the uniform disk with emissivity decreasing as power-law of radius). The inner ring, contributes to the red tail of the line, while the outer ring forms its main body.

through the gravitational field of the black hole, and this effect is very strong near the horizon (Connors et al., 1980; Bao et al., 1996). In consequence, the changing polarization angle diminishes the final polarization degree as the observed signal is obtained by integration over the accretion disk. Perhaps the most interesting attribute of the proposed mechanism is that it requires the action of strong gravitational field which according to general relativity can be created only by a black hole.

## 1.2 Localized excess in line red wing

Spectral lines from a black hole accretion disk are broadened, shifted and skewed by relativistic effects (Fabian et al., 1989). The theoretical profiles have been studied in great detail (e.g. Fanton et al., 1997; Karas, 2006, and references cited therein). The typical double-horn profile of a narrow ring is well-known, however, the expected shapes integrated over the range of radii are far more rich and they reflect an interplay of different effects.

As the inclination of the accretion disk increases, the spectral profile may incur some additional peaks caused by gravitational lensing (Matt et al., 1993; Beckwith & Done, 2004). We take lensing into account, however, in case of Seyfert

galaxies, very high ($\theta_{\rm o} \gtrsim 80$ deg, i.e. almost edge-on) inclinations are not expected because in that case the nuclear region becomes obscured by the outer torus. For example the inner disk of MCG–6-30-15 is thought to be oriented at inclination not exceeding 40 deg; the most likely value is about $\theta_{\rm o} \simeq 30$ deg (Dovčiak et al., 2004a). Therefore, the explanation of these secondary peaks needs to be sought elsewhere.

General relativistic magnetohydrodynamic simulations (Agol & Krolik, 2000; Beckwith et al., 2008) suggest that in some situations a significant magnetic stress affects the accretion flow near and inside ISCO. Such flows could dissipate energy and produce radiation in a manner noticeably different from the predictions of the standard model; namely, the inner edge of the radiating region could disagree with ISCO and it could be shifted towards smaller radii. It is not clear if this mechanism modulates also the line emission, however, it motivates us to resurrect the phenomenological dual-ring model of the non-standard accretion emissivity of the line (Dovčiak et al., 2004a) to verify if its prediction about the details of the broad red wing are still consistent with present data and if the test can be improved.

Because of the interplay among fast orbital motion of the radiating gas, strong gravitational attraction and growing effects of frame-dragging (in case of a spinning black hole) near horizon, the observational consequences of such enhanced radiation are not easy to estimate. On one side, it has been argued that frame-dragging helps to focus radiation near an extreme Kerr black hole (the signal is modulated by indirect photons at additional 10–15% level; Fukumura & Kazanas 2008). On the other hand, much of radiation falls into the loss cone and is captured by the black hole (Noble et al., 2009), thus escaping any chance of the observational detection.

For MCG–6-30-15, Dovčiak et al. (2004a, model 2b) found that the mentioned 4.8 keV spectral curvature can be modeled as a contribution from an inner ring below $r \lesssim 2.1\, r_{\rm g}$ around an $a = 0.72$ spinning black hole. In that work we had to conclude that the origin of residuals near cannot be clarified with the time-averaged data. Given the value of $a$, the corresponding ISCO radius is about $r_{\rm ISCO} = 3.5\, r_{\rm g}$, so the inner ring is entirely immersed within the plunging region where matter is assumed to be radially infalling with roughly constant angular momentum. Despite the close proximity of the horizon, the visible contribution to the observed spectral profile persists.

The inferred proximity of the inner ring to the black hole horizon can be tested as the future polarimetric data become available. The idea is based on two well-founded considerations. Firstly, because the Fe K line complex arises by reflection of the primary X-rays on the accretion disk, the signal should be intrinsically polarized, with the degree of polarization reaching $P \simeq$ 10–30% (Dovčiak et al., 2004b). Secondly, because gravitational field rotates the observed polarization by different angle as the light propagates along rays in the curved space-time, the final polarization becomes diminished. The depolarizing influence depends on how effective the rotation of the polarization angle is, and how much it varies over the source (Dovčiak et al., 2008).

The change of polarization angle is very sensitive to the radius of the footpoint from which the light ray originates in the accretion disk. A critical radius, $r = r_c$, occurs in the disk plane (Connors et al. 1980; Dovčiak et al. 2008 – see their figure 3). As the footpoint moves along a ring of constant radius, $r > r_c$, the observed polarization angle sways by certain amount. Once the emission radius drops below the critical point, $r < r_c$, the observed direction of polarization turns around by full angle. Therefore the depolarizing effect is much stronger if the signal comes from a ring in close vicinity of the black hole.

We remind the reader that another explanation of the redshifted component would be to understand it as the red wing of the traditional double-horn profile. In this case the component would be produced at the same radius as the core of the line and its blue wing, and the expected polarization should correspondingly reflect the different radius. Notice that the latter interpretation of the redshifted component requires different fit to the underlying continuum, so the distinction between the two possibilities is quite important for correct determination of the model parameters, such as the black hole spin. Finally, the absorption scenario (Turner et al., 2006; Miller et al., 2009) has been widely discussed during recent years as an alternative explanation of the broad spectral features.

It is worth noticing that Faraday rotation may influence the results for polarization from a magnetized accretion disk (Silantev & Gnedin, 2008). However, this effect can be taken account thanks to its specific dependency on the energy. In fact, the change of polarization angle by Faraday rotation decreases with the square of photon energy, so the X-rays are less susceptible.

## 1.3 Relativistic lines as superposition of ring profiles

Intermittent episodes of a localized disk irradiation can naturally lead to a radially stratified emission profile rather than monotonic, continuous dependence of a standard accretion disk. We can approximate this configuration by radially constrained zones, which can be called "rings". Let us remark that we are concerned with a spectral line emissivity, which is only partly related to the gas density; the essential quantity here is the ionization state of matter and how this varies with radius. Localized coronal irradiation of the disk material enhances the line emission above the mean value in the neighborhood of a certain point. Integration of detected signal over a period of time then effectively produces a ring-type source (Goosmann et al., 2007).

In other words, one need not imagine physically separate rings and gaps emerging within the disk, even if this possibility has been also discussed; e.g. Cuadra et al. (2009) show a temporary density ring in an accretion disk surrounding a black-hole binary, while Artymowicz et al. (1993) and Karas & Šubr (2001) examine the process of gap formation by a secondary satellite embedded within the disk.

According to the standard (stationary) accretion disk scenario (Novikov &

Thorne, 1973; Page & Thorne, 1974), most radiation is produced within just a few gravitational radii above ISCO (up to $\simeq 20\,r_{\rm g}$). Also various X-ray spectral features and the power-law component of the disk corona are believed to originate in that region. This main flux-producing area of the accretion disk is still rather wide in radius, hence it is thought to be the origin of the broad component of the line, which we include by employing the relativistic `kyrline` model (Dovčiak et al., 2004b).

Some reports suggest transient structures that are localized in radius and exhibit themselves as narrow features in the spectrum (e.g. Guainazzi, 2003; Dovčiak et al., 2004a; de Marco et al., 2009, and references cited therein). In our picture of time-integrated spectra these are represented by rings. Although the significance of these features is still debated, their origin fits in the scenario of magnetic flares as sites of primary local illumination.

Magnetic flares are thought to occur above the accretion disk (Czerny et al., 2004; Uzdensky & Goodman, 2008); in this context the line emission of the rings would arise not because the accretion disk develops such a physical structure, but instead the localized emission by reconnection flares illuminates the underlying disk at a certain place, affecting there its ionization and producing the observable reflection features in spectrum. Rotation of the disk matter and time integration of the signal during observation produce belts out of point-like sites of illumination. In fact, we could then call these structures as reflection rings.

Although the mentioned scheme is our preferred way of effectively producing the rings, similar effects can arise by different mechanisms operating near a black hole. They can be broadly distinguished in two categories. Firstly, during the period of intermittent accretion the flow of material varies and the density profile and other variables (ionization state profile) can change along (e.g. King et al., 2006; Ballantyne et al., 2011). In another context, global spiral waves were suggested as a possible source of light curve modulation of accreting black holes (Tagger & Varnière, 2006). Unlike ideal rings these spirals structures have a non-negligible radial extent, although to certain extent they could mimic rings in case of significant wounding in azimuthal direction (Karas & Šubr, 2001). The formation of separate annuli occurs also in some models of strongly magnetized plasma disks (Coppi & Rousseau, 2006). Finally, confined radii of enhance emission are a consequence of avalanche models (Pecháček et al., 2008) where multiple flares arise in mutually connected families and gradually propagate towards the center before decaying at some characteristic distance.

In contrast to the model of major flares mentioned formerly, the latter alternatives appear to be unable of modulating the outgoing spectrum in any significant manner for a required period of time (Schnittman et al., 2006). Nonetheless, the current modeling has not yet provided a definitive answer and different options should be investigated further. In fact, the topic for debates is the expected level of the electromagnetic signal modulation above the noise and the ability to detect it by a given technology, rather than the existence of the modulation at a certain small level.

The existence of ring structure could be revealed by future detailed spec-

troscopy of the spectral line wings. To this end we develop a rigorous method of calculating the expected energy range of a spectral line, taking into account the effects of strong gravity on photons proceeding from the disk to the observer. These photons may follow complicated routes, but we assume that they do not cross the equatorial plane of the black hole and are neither absorbed nor scattered by environment outside the accretion disk. We give accurate extremal shifts over a wide range of parameters (see chap. 4).

The adopted setup is relevant for geometrically thin, planar accretion disks. Needless to say, the method will require high energy resolution together with a sufficient number of counts in the observed spectrum. The former condition is achievable with X-ray calorimeters. The latter one imposes a more serious limitation, however, bright Galactic black holes seem to be appropriate sources. Even if an immediate application of the idea is not possible at present, the calculation of the extremal energy shifts is by itself an interesting addition and of practical use in future.

Relativistic spectral lines have been modeled via various approaches, analytical and numerical ones. But one may also ask a simpler question about the extremal energy shifts, which basically give only the line width and the position of the two horns rather than a detailed spectral shape. A double-horn spectral profile is a specific feature of a ring positioned at a given radius. Although the calculation providing just the extremal shifts should seemingly be easy, it has not yet been brought out in a systematic manner.

Fine substructures of the relativistic line from the accretion disk can be used to constrain the inclination angle, radial emissivity distribution in the disk plane, and even the angular momentum of the central black hole (Beckwith & Done, 2004). Fig. 1.7 illustrates this by showing the formation of a model spectrum originating as a superposition of several ring profiles. Blue and red horns of the separate rings rise up above the central body of the line. They can be recognized in the wings of the total profile (relative normalization of the rings fluxes has been set proportional to $r^{-3}$). Sharp peaks of the spectral profile from a narrow ring occur at the maximum and minimum values of the observed energy.

Let us note that the idea of studying the signatures of black holes via spectroscopy of radiation sources in relativistic orbital motion has a long history (Cunningham & Bardeen, 1973). Theoretical light curves and spectral line profiles were calculated including various effects of general relativity: the frame-dragging, extreme light-bending, and multiple images (Kojima, 1991; Laor, 1991; Karas et al., 1992; Matt et al., 1993; Fanton et al., 1997, and further references cited therein).

We concentrate on direct evaluation of the extremal shifts, while the available numerical tools can be used to test our results. To this end, we employ the KY suit of codes (Dovčiak et al., 2004b), which includes KYRLINE routine for the desired observed shape of a relativistic line. In order to achieve high accuracy of simulated lines from very narrow annuli ($\Delta r \lesssim 0.1$), we found the KYRLINE code to be superior in the sense that the resulting profiles do not contain artificial numerical oscillations. This high accuracy is important for understanding the interplay of general relativistic effects (energy shifts and the light bending) that

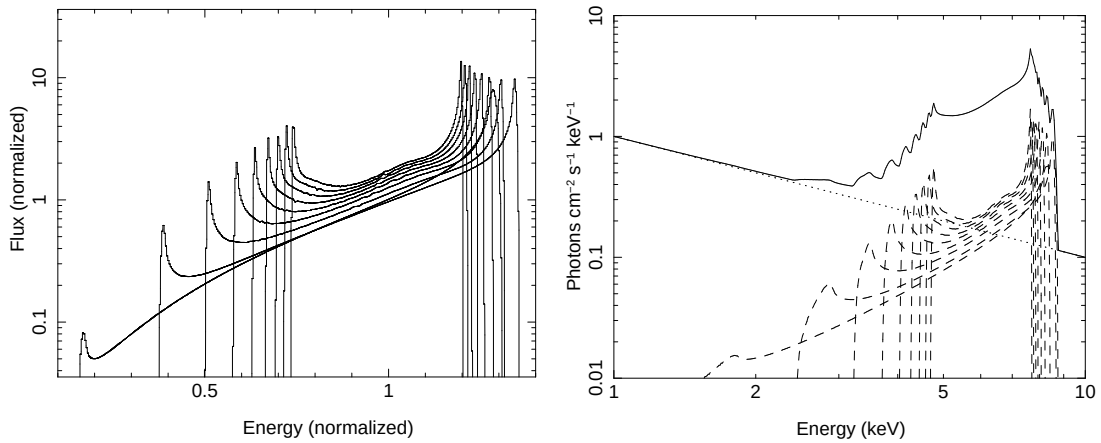


Figure 1.7: Forming a double-horn spectral line by superposing profiles of several narrow-rings. Left: theoretical profiles from a set of nine infinitesimally narrow rings orbiting in the equatorial plane of a Kerr black hole. Radii of the rings increase equidistantly from $r = 2$ to $r = 18$ gravitational radii. Broader and more redshifted profiles correspond to smaller rings, which rotate at faster speed and reside deeper in the gravitational well. Energy is normalized to the unit rest energy of the line; each profile then extends from minimal to maximal energy shift for its corresponding parameters. Background continuum is subtracted. Right: as on the left, but with rings of a small (finite) radial extent of $\Delta r = 1$. The rest energy of the line is set to 6.4 keV and a power-law continuum added to reflect the fact that line profiles in real spectra are obtained by considering the proper underlying continuum. Dashed lines denote the individual components forming the prototypical spectrum; the latter is shown by the solid line. The signature of the individual rings is visible in the wings of the final profile. The common parameters of both plots are: observer inclination 75 deg (i.e. close to the edge-on view), black hole spin $a = 0.998$ (prograde rotation).

form the spectral profile, because the final shape is more complicated than a simple special-relativistic double-horn line.

Aside from the mentioned speculations, one may ask if the actual presence of the rings can be tested. Here we thus presume that the structure develops and modulates the outgoing signal, and we want to verify whether the location of emission rings could be reconstructed from the observed spectrum. By assuming the existence of the modulation we investigate if these structures can be spectrally resolved in present-day or future X-ray spectra (see chap. 5).

In that chapter we discuss whether the proposed Large Observatory for X-ray Timing (LOFT; Feroci et al. 2010, 2012) will have the necessary capability, at least for bright enough sources. To this end we produce artificial data with appropriate properties and then we analyze them by using a preliminary response file.

## 1.4 Prospects of detecting general relativity effects with future X-ray missions

X-ray domain is a suitable part of the electromagnetic spectrum where the effects of strong gravity can be revealed. A significant fraction of light from accreting black holes and compact stars is released and reprocessed in X-rays.

In this section, we introduce two proposals for new X-ray missions: LOFT (medium-size mission) and Athena+ (large-size mission). Currently, these are two particularly relevant X-ray missions that have been selected in the advanced stage of discussion for future development. The two proposals differ in many aspects and they are neutrally complementary, and both are important for physics discussed in this thesis. For definiteness of our examples we futher concentrate of LOFT more closely.

### 1.4.1 LOFT

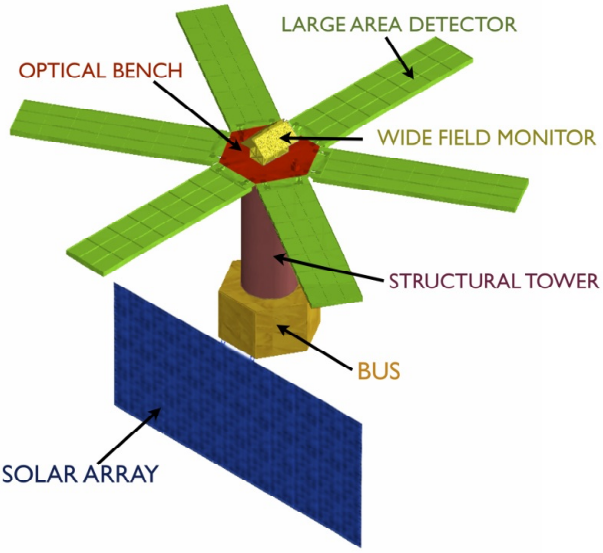


Figure 1.8: Conceptual scheme of the LOFT satellite.

LOFT (Large area Observatory For x-ray Timing) is one of the four space missions concepts of the Cosmic Vision "Call for a Medium-size mission opportunity for a launch at the start of the 2020s" proposed to ESA (Feroci et al. 2010, 2012). Fig. 1.8 shows the conceptual scheme of the LOFT satellite with two mean instruments: LAD and WFM.

The Large Area Detector (LAD) reaches an effective area of $\sim 10$ m$^2$ (@8 keV), which will provide a total of $\sim 200\,000$ cts/s for a 1 Crab source (about 3000 cts/s are expected from the background) and spectral resolution of $\sim 260$ keV in the energy band $2 - 30$ keV. The operational energy band will extend up

to 80 keV, but only a coarse energy resolution ($\geq 2$ keV) is expected in the energy range $30-80$ keV. LAD is going to use 76 cm$^2$ monolithic Silicon Drift Detectors (SDDs) with 854 $\mu$m anodes and a drift distance of 35 mm to achieve a total 10 m$^2$ (goal 12 m$^2$) area.

The Wide Field Monitor (WFM) is the second instrument and completes the scientific payload of LOFT. Its goal is to observe about 50 % of the sky available to the LAD in the same energy band at any time and then to catch good triggering sources that can be pointed with the LAD. The design of the WFM is based on the heritage of SuperAGILE (Feroci et al., 2007), but, instead of microstrip detectors, it exploits the same type of SDDs as the LAD except for a finer pitch ($\sim 300$ $\mu$m). Other specifications of the LAD and WFM can be found in tab. 1.1.

| Parameter | Value (LAD) |
|---|---|
| Energy range | $2-30$ keV ($30-80$ keV extended) |
| Effective area | 10 m$^2$ |
| Field of view | $\leq 1^\circ$ |
| Energy resolution | $\leq 260$ eV at 6 keV |
| Time resolution | $\sim 7$ $\mu$s |
| Dead time | $\leq 1\%$ for 1 Crab source |
| Background | $\sim 10$ mCrab |
| Maximum average source flux (steady, peak) | 0.5 Crab, 15 Crab |
| | Value (WFM) |
| Energy range | $2-50$ keV ($50-80$ keV extended) |
| Effective area | $> 80$ cm$^2$ |
| Field of view | $180^\circ \times 90^\circ + 90^\circ \times 90^\circ$ toward night hemisphere |
| Energy resolution | $< 500$ eV |
| Angular resolution | 5' |
| Point source accuracy | 1' |
| Sensitivity ($5\sigma$, 3 s) | 270 mCrab |
| Sensitivity ($5\sigma$, 58 ks) | 2.1 mCrab |

Table 1.1: The LAD and WFM performance specifications.

The LAD background has been analyzed and computed using Monte Carlo simulations of a mass model of the whole LOFT spacecraft and all known radiation sources in the LOFT orbit by Campana et al. (2012). From the simulations, it is obvious the background is dominated ($> 70\%$) by high energy photons of cosmic X-ray background and Earth albedo leaking and scattering through the collimator structure. These two sources are stable and predictable, although there exist small modulation of these components due to orbital motion of the satellite around the Earth. One of the varying sources is particle induced background ($< 6\%$ of overall background). The largest modulation of the total LAD background is estimated as $< 20\%$ and can be effectively described by a geometrical

model that should predict the background at the level of 1% or better ($1 - 20$ keV).

Ultradense matter in neutron stars, and strong gravity are the main scope of an observation and study. LOFT mission will be capable to study the equation of state from X-ray pulsations or from modeling of photospheric radius expansion events. LOFT could also be possible to confirm (and study) that global seismic oscillations occur during major flares or glitches from magnetars. LOFT project should be ideal to study Galactic black holes and bright AGNs (down to a flux of $\sim 1$ mCrab), including the behavior of matter in the strong gravity regime.

The advantages of LOFT are a big effective are of 10 $m^2$ that should provide a high resolution in 3 and 10 keV energy range; a good time resolution for lightcurves and spectra that will be used to study fast coherent pulsations and quasi-periodic oscillation (QPOs) in the X-ray flux of accreting neutron stars and black holes; and WFM that will monitor the X-ray sky, detect and locate bright X-ray transient. Correct modeling of the background is crucial for the success of the measurements.

### 1.4.2 Athena+

Athena+ (Advanced Telescope for High-ENergy Astrophysics) is a large-mission proposal for late 2020s for the ESA science program (Nandra et al., 2013). The payload of the satellite are three instruments: a single X-ray telescope with a focal length of 12 m and an unprecedented effective area (2 $m^2$ at 1 keV); the X-ray Integral Field Unit (X-IFU), an advanced actively shielded X-ray microcalolimeter spectrometer for high-resolution imaging; and the Wide Field Imager (WFI), a silicon active pixel sensor camera with a large field of view, high counter-rate and moderate resolution spectroscopic capability. Tab 1.2 presents key parameters of the instruments of Athena+ satellite.

| Parameter | Requirements |
|---|---|
| Effective area | 2 $m^2$ 1 keV |
| | 0.25 $m^2$ 6 keV |
| Angular resolution | 5” |
| Energy resolution | $0.3 - 12$ keV |
| Field of view | WFI: 40’ |
| | X-IFU: 5’ |
| Spectral resolution | WFI: $<$ 150 eV 6 keV |
| | X-IFU: 2.5 eV 6 keV |

Table 1.2: The parameters of Athena+ mission.

Athena+ wants to focus on many cosmic processes observable in X-rays, e.g., the formation and evolution of groups and clusters of galaxies, studying warm-hot intergalactic medium, the physics of accretion, etc. Athena+ could be a successor

of XMM-Newton mission and has advantages in the ability of imaging and a better spectral resolution. Athena+ does not need this precise model of the background.

# Chapter 2

# Photon propagation in Kerr metric

## 2.1 Definition and properties of Kerr metric

In our work, we consider a rotating black hole formed by a gravitational collapse of a compact body with an angular momentum. That is why we use Kerr metric (Kerr, 1963; Chandrasekhar, 2004) to describe a gravitational field of a black hole that represents a unique solution of Einstein equations under very general relevant assumptions, such as asymptotical flatness and regularity of the horizon. The metric is both stationary (independent of time, $t$) and axisymmetric about the polar axis (independent of angle, $\phi$), and depends only on two parameters: the mass, $M$, of the black hole, and its angular momentum per unit mass, $a = J/M$. The form of the Kerr metric in Boyer-Lindquist coordinates (Boyer & Lindquist, 1967) $(t, r, \theta, \phi)$ $(c = G = 1)$ is

$$\mathrm{d}s^2 = -\Sigma\frac{\Delta}{A}\mathrm{d}t^2 + \frac{A}{\Sigma}\left(\mathrm{d}\phi - \frac{2ar}{A}\mathrm{d}t\right)^2 \sin^2\theta + \frac{\Sigma}{\Delta}\mathrm{d}r^2 + \Sigma\mathrm{d}\theta^2 \tag{2.1}$$

or, in another form,

$$\mathrm{d}s^2 = -\left(1 - \frac{2r}{\Sigma}\right)\mathrm{d}t^2 - \frac{4ar}{\Sigma}\sin^2\theta\mathrm{d}t\mathrm{d}\phi + \frac{A}{\Sigma}\sin^2\theta\mathrm{d}\phi^2 + \frac{\Sigma}{\Delta}\mathrm{d}r^2 + \Sigma\mathrm{d}\theta^2, \tag{2.2}$$

where

$$\Sigma = r^2 + a^2\cos^2\theta, \tag{2.3}$$

$$\Delta = r^2 - 2r + a^2, \tag{2.4}$$

$$A = (r^2 + a^2)^2 - a^2\Delta\sin^2\theta, \tag{2.5}$$

where we set $M = 1$ without any loss of generality.

The components of the covariant form of the metric tensor, $g_{\alpha\beta}$, are

$$\begin{gathered} g_{tt} = -\left(1 - \frac{2r}{\Sigma}\right);\ g_{rr} = \frac{\Sigma}{\Delta}; \\ g_{\theta\theta} = \Sigma;\ g_{\phi\phi} = \frac{A}{\Sigma}\sin^2\theta; \\ g_{t\phi} = g_{\phi t} = -\frac{2ar}{\Sigma}\sin^2\theta. \end{gathered} \tag{2.6}$$

The contravariant form of the metric tensor, $g^{\alpha\beta}$, has components

$$\begin{aligned} g^{tt} &= -\frac{A}{\Sigma\Delta};\ g^{rr} = \frac{\Delta}{\Sigma}; \\ g^{\theta\theta} &= \frac{1}{\Sigma};\ g^{\phi\phi} = \frac{\Delta - a^2\sin^2\theta}{\Sigma\Delta\sin^2\theta}; \\ g^{t\phi} &= g^{\phi t} = -\frac{2ar}{\Sigma\Delta}. \end{aligned} \tag{2.7}$$

For the case $a = 0$, Kerr metric corresponds to a nonrotating black hole that is described by Schwarzschild metric

$$\mathrm{d}s^2 = -\left(1 - \frac{2}{r}\right)\mathrm{d}t^2 + \left(1 - \frac{2}{r}\right)^{-1}\mathrm{d}r^2 + r^2(\mathrm{d}\theta^2 + \sin^2\theta\mathrm{d}\phi^2) \tag{2.8}$$

and the solutions for a rotating black hole are only if $|a| \leq 1$.

The horizons are roots of the equation $\Delta = 0$, from which it follows that the outer and inner horizons are:

$$r_{\mathrm{h}} = r_+ = 1 + \sqrt{1 - a^2}, \tag{2.9}$$

$$r_- = 1 - \sqrt{1 - a^2}. \tag{2.10}$$

The limiting values are $r_{\mathrm{h}} = 2$ and $r_- = 0$ for $a = 0$; and $r_{\mathrm{h}} = 1$ and $r_- = 1$ for $a = 1$ (maximally rotating black hole). In the case the spin exceeds the mass of the black hole, $a > 1$, the spacetime metric would have a so-called "naked" singularity.

In Schwarzschild metric, the event horizon is identical to the stationary surface, $g_{tt} = 0$, while in Kerr metric the stationary surface, $r_{\mathrm{s}}$, is described by another equation than the horizon, $r_{\mathrm{h}}$,

$$r_{\mathrm{s}} = 1 + \sqrt{1 - a^2\cos^2\theta}. \tag{2.11}$$

This occurs when $r^2 - 2r + a^2\cos^2\theta = 0$. The stationary surface is called the static limit and the region $r_{\mathrm{h}} < r \leq r_{\mathrm{s}}$ the ergosphere.

The four-momentum of a test particle is $p^\mu \equiv \mathrm{d}x^\mu/\mathrm{d}\lambda$, where $\lambda$ is related to proper time by $\lambda = \tau/\mu$ that is an affine parameter in the limit $\mu \to 0$, $\mu$ is the rest mass of the particle (Carter, 1968). It is found that:

$$\begin{aligned} \sqrt{A}\frac{\mathrm{d}r}{\mathrm{d}\lambda} &= \pm\sqrt{V_r};\ \sqrt{A}\frac{\mathrm{d}\theta}{\mathrm{d}\lambda} = \pm\sqrt{V_\theta}; \\ \sqrt{A}\frac{\mathrm{d}\phi}{\mathrm{d}\lambda} &= -\left(a\mathcal{E} - \frac{L_z}{\sin^2\theta}\right) + \frac{aT}{\Delta}; \\ \sqrt{A}\frac{\mathrm{d}t}{\mathrm{d}\lambda} &= -a\left(a\mathcal{E}\sin^2\theta - L_z\right) + \frac{\left(r^2 + a^2\right)T}{\Delta}. \end{aligned} \tag{2.12}$$

Here, $V_r$, $V_\theta$ are effective potentials for a radial and latitudinal motion:

$$\begin{aligned} T(\mathcal{E}, L_z, r) &\equiv \mathcal{E}\left(r^2 + a^2\right) - L_z a; \\ V_r(\mathcal{E}, L_z, r, \theta) &\equiv T^2 - \Delta\left[\mu^2 r^2 + \left(L_z - a\mathcal{E}\right)^2 + Q\right]; \\ V_\theta(\mathcal{E}, L_z, r, \theta) &\equiv Q - \cos^2\theta\left[a^2\left(\mu^2 - \mathcal{E}\right) + \frac{L_z^2}{\sin^2\theta}\right], \end{aligned} \tag{2.13}$$

where $\mathcal{E}$, $L_z$ and $Q$ are three constants of motion, the total energy, azimuthal component of angular momentum aligned with the spin of the black hole and Carter's constant (for more details see sec. 2.3).

We want to study energy shifts of iron line from a disk lying on circular orbits in an equatorial plane of a black hole spacetime, therefore we can set $\theta = \pi/2$, and have the conditions for a circular orbit of a constant radius, $r_0$:

$$V_r(r_0) = 0; \ \frac{\mathrm{d}V_r(r_0)}{\mathrm{d}r} = 0. \tag{2.14}$$

Setting $\theta = \pi/2$ in eq. 2.2 we obtain the Lagrangian

$$2L = -\left(1 - \frac{2}{r}\right)\dot{t}^2 - \frac{4a}{r}\dot{t}\dot{\phi} + \frac{r^2}{\Delta}\dot{r}^2 + \left(r^2 + a^2 + \frac{2a^2}{r}\right)\dot{\phi}^2, \tag{2.15}$$

where $\dot{t} = p^t = \mathrm{d}x^t/\mathrm{d}\lambda$, and so on. The Lagrangian does not depend on the coordinates $t$ and $\phi$, we obtain two first integrals:

$$p_t \equiv \frac{\partial L}{\partial \dot{t}} = \text{constant} = -\mathcal{E}, \tag{2.16}$$

$$p_\phi \equiv \frac{\partial L}{\partial \dot{\phi}} = \text{constant} = L_z. \tag{2.17}$$

The rest of covariant components of the four-momentum, $p_r$ and $p_\theta$, can be found in sec. 2.2, equations in (2.49).

The equations for $\dot{t}$ and $\dot{\phi}$ can be obtained from eq. (2.16) and (2.17), where we set eq. (2.15)

$$\dot{t} = p^t = \frac{\left(r^3 + a^2 r + 2a^2\right)\mathcal{E} - 2aL_z}{r\Delta}, \tag{2.18}$$

$$\dot{\phi} = p^\phi = \frac{(r-2)L_z + 2a\mathcal{E}}{r\Delta}. \tag{2.19}$$

We can also get these equations by setting $\theta = \pi/2$ into eqs. (2.48).

If we substitute eqs. (2.18), (2.19) into $g_{\alpha\beta}p^\alpha p^\beta = -\mu^2$ and make some simplifications, we obtain the third integral of motion

$$r^2\left(\frac{\mathrm{d}r}{\mathrm{d}\lambda}\right) = V_r(\mathcal{E}, L_z, r), \tag{2.20}$$

where $V_r(\mathcal{E}, L_z, r)$ is an effective potential for the radial motion in the equatorial plane

$$V_r(\mathcal{E}, L_z, r) = \mathcal{E}\left(r^3 + a^2 r + 2a^2\right) - 4a\mathcal{E}L_z - (r-2)L_z^2 - \mu^2 r\Delta. \tag{2.21}$$

Now we return to the conditions (2.14). These two equations can be solved to yield conditions on $\mathcal{E}$, $L_z$ for the circular orbit, specifically:

$$\frac{\mathcal{E}}{\mu} = \frac{r^2 - 2r \pm ar^{1/2}}{r\sqrt{r^2 - 3r \pm 2ar^{1/2}}}; \ \frac{L_z}{\mu} = \frac{\pm r^{1/2}\left(r^2 \mp 2ar^{1/2} + a^2\right)}{r\sqrt{r^2 - 3r \pm 2ar^{1/2}}}. \tag{2.22}$$

Here the upper sign refers to prograde and the lower sign to retrograde orbits. The angular velocity of circular orbits, $\Omega$, can be obtained by the combination of eq. (2.22) with the latter two equations of eq. (2.12). We find:

$$\Omega = v^{\phi} = \frac{\mathrm{d}\phi}{\mathrm{d}t} = \frac{1}{a \pm r^{3/2}}. \tag{2.23}$$

Clearly, for circular orbits to be possible at a given radii, the denominator of eq. (2.14) must be real, that is true only if

$$r^{3/2} - 3r^{1/2} \pm 2a \geq 0. \tag{2.24}$$

The root of this equation (cubic equation in $r^{1/2}$), $r_{\rm ph}$, describes an orbit with infinite energy per unit rest mass, which corresponds physically to a photon orbit. Such an orbit is the innermost circular orbit for all particles for a given black hole spin. We find that:

$$r_{\rm ph} = 2 + 2\cos\left[\frac{2}{3}\cos^{-1}(\mp a)\right]. \tag{2.25}$$

Not all of the circular orbits are bound in the region $r > r_{\rm ph}$. An unbound circular orbit has $\mathcal{E}/\mu \geq 1$. With an infinitesimal outward perturbation a particle in such an orbit will escape to infinity on an asymptotically hyperbolic trajectory. The marginally bound radius, $r_{\rm mb}$ is found by considering the limiting case $\mathcal{E}/\mu = 1$:

$$r_{\rm mb} = 2 \mp a + 2\sqrt{1 \mp a}. \tag{2.26}$$

Bound circular orbits exist for $r > r_{\rm mb}$. This radius also represents the minimum periastron of all parabolic orbits ($\mathcal{E}/\mu = 1$). Parabolic orbits that fall within $r_{\rm mb}$ are necessarily captured by the hole.

But not all of the bound circular orbits in the equatorial plane are stable. Stability requires:

$$\frac{\mathrm{d}^2 V_r(r_0)}{\mathrm{d}r^2} \leq 0. \tag{2.27}$$

Applying this condition to eq. (2.21), the stable orbits must satisfy a quartic equation in $r^{1/2}$

$$r^2 - 6r \pm 8ar^{1/2} - 3a^2 \geq 0. \tag{2.28}$$

The root of this equation represents the marginally stable orbit, $r_{\rm ms}$, that takes the form (Bardeen et al., 1972):

$$r_{\rm ms} = 3 + Z_2 \mp [(3 - Z_1)(3 + Z_1 + 2Z_2)]^{1/2}, \tag{2.29}$$

where

$$Z_1 = 1 + (1 - a^2)^{1/3}[(1 + a)^{1/3} + (1 - a)^{1/3}], \tag{2.30}$$

$$Z_2 = (3a^2 + Z_1^2)^{1/2}. \tag{2.31}$$

## 2.2 Separability of Hamilton-Jacobi equation

The description of the geodesic motion in Kerr spacetime can be found by solving the Hamilton-Jacobi equation

$$2\frac{\partial S}{\partial \tau} = g^{\alpha\beta}\frac{\partial S}{\partial x^{\alpha}}\frac{\partial S}{\partial x^{\beta}}, \tag{2.32}$$

where $S$ denotes Hamilton's principal function. The separability of the Hamilton-Jacobi equation and the existence of the fourth integral that is conserved along a geodesic were first discovered by Carter (1968).

Due the knowledge of the components in the metric tensor, $g^{\alpha\beta}$, for Kerr geometry, eqs. in (2.7), the Hamilton-Jacobi equation, eq. (2.32), becomes

$$\begin{aligned} 2\frac{\partial S}{\partial \tau} &= \frac{\Sigma^2}{\rho^2\Delta}\left(\frac{\partial S}{\partial t}\right)^2 + \frac{4ar}{\rho^2\Delta}\frac{\partial S}{\partial t}\frac{\partial S}{\partial \phi} - \frac{\Delta - a^2\sin^2\theta}{\rho^2\Delta\sin^2\theta}\left(\frac{\partial S}{\partial \phi}\right)^2 \\ &\quad -\frac{\Delta}{\rho^2}\left(\frac{\partial S}{\partial r}\right)^2 - \frac{1}{\rho^2}\left(\frac{\partial S}{\partial \theta}\right)^2. \end{aligned} \tag{2.33}$$

The solution is seeked in the form

$$S = \frac{\delta\tau}{2} - \mathcal{E}t + L_z\phi + S_r(r) + S_\theta(\theta), \tag{2.34}$$

because we assume the separable variables. Here, $\delta = 0$ means photons and $\delta = 1$ particles.

The final separable form of the Hamilton-Jacobi equation (after some algebra, more on p. 344-345, Chandrasekhar, 2004) can be written as

$$\begin{aligned} &\left\{\Delta\left[\frac{\mathrm{d}S_r(r)}{\mathrm{d}r}\right]^2 - \frac{1}{\Delta}\left[\left(r^2+a^2\right)\mathcal{E} - aL_z\right]^2 + \left(L_z - a\mathcal{E}\right)^2 + \delta r^2\right\} \\ &\quad + \left\{\left[\frac{\mathrm{d}S_\theta(\theta)}{\mathrm{d}\theta}\right]^2 + \left(\frac{L_z^2}{\sin^2\theta} - a^2\mathcal{E}^2\right)\cos^2\theta + \delta a^2\cos^2\theta\right\} = 0. \end{aligned} \tag{2.35}$$

From this, two equations are obvious

$$\Delta\left[\frac{\mathrm{d}S_r(r)}{\mathrm{d}r}\right]^2 = \frac{1}{\Delta}\left[\left(r^2+a^2\right)\mathcal{E} - aL_z\right]^2 - \left[Q + \left(L_z - a\mathcal{E}\right)^2 + \delta r^2\right] \tag{2.36}$$

and

$$\left[\frac{\mathrm{d}S_\theta(\theta)}{\mathrm{d}\theta}\right]^2 = Q - \left[a^2\left(\delta - \mathcal{E}^2\right) + \frac{L_z^2}{\sin^2\theta}\right]\cos^2\theta, \tag{2.37}$$

where $Q$ is the separation constant (or Carter's constant).

At this moment, we introduce two effective potentials

$$R(r) = \left[\left(r^2+a^2\right)\mathcal{E} - aL_z\right]^2 - \Delta\left[Q + \left(L_z - a\mathcal{E}\right)^2 + \delta r^2\right] \tag{2.38}$$

and

$$\Theta(\theta) = Q - \left[a^2\left(\delta - \mathcal{E}^2\right) + \frac{L_z^2}{\sin^2\theta}\right]\cos^2\theta, \tag{2.39}$$

and the seeked functions $S_r$ and $S_\theta$ in eq. (2.34) can be calculated from eq. (2.36) and (2.37) as

$$S_r = \int^r \frac{\sqrt{R(r)}}{\Delta}\mathrm{d}r \tag{2.40}$$

and

$$S_\theta = \int^\theta \sqrt{\Theta(\theta)}\mathrm{d}\theta, \tag{2.41}$$

then the solution for Hamilton's function $S$ is

$$S = \frac{\delta\tau}{2} - \mathcal{E}t + L_z\phi + \int^r \frac{\sqrt{R(r)}}{\Delta}\mathrm{d}r + \int^\theta \sqrt{\Theta(\theta)}\mathrm{d}\theta. \tag{2.42}$$

To describe the geodesic motion we use the standard procedure of setting to zero the partial derivatives of $S$, eq. (2.42), with respect to the different constants of motion - $Q$, $\delta$, $\mathcal{E}$ and $L_z$ in this instance.

$$\frac{\partial S}{\partial Q} = \frac{1}{2}\int^r \frac{1}{\Delta\sqrt{R(r)}}\frac{\partial R(r)}{\partial Q}\mathrm{d}r + \frac{1}{2}\int^\theta \frac{1}{\sqrt{\Theta(\theta)}}\frac{\partial\Theta(\theta)}{\partial Q}\mathrm{d}\theta = 0 \tag{2.43}$$

leads to the equation

$$\int^r \frac{\mathrm{d}r}{\sqrt{R(r)}} = \int^\theta \frac{\mathrm{d}\theta}{\sqrt{\Theta(\theta)}}. \tag{2.44}$$

Similarly, we find

$$\tau = \int^r \frac{r^2}{\sqrt{R(r)}}\mathrm{d}r + a^2\int^\theta \frac{\cos^2\theta}{\sqrt{\Theta(\theta)}}\mathrm{d}\theta \tag{2.45}$$

$$t = \tau\mathcal{E} + 2\int^r r\left[r^2\mathcal{E} - a\left(L_z - a\mathcal{E}\right)\right]\frac{\mathrm{d}r}{\Delta\sqrt{R(r)}}, \tag{2.46}$$

and

$$\phi = a\int^r \left[\left(r^2 + a^2\right)\mathrm{E} - aL_z\right]\frac{\mathrm{d}r}{\Delta\sqrt{R(r)}} + \int^\theta \left(\frac{L_z^2}{\sin^2\theta} - a\mathcal{E}\right)\frac{\mathrm{d}\theta}{\sqrt{\Theta(\theta)}}. \tag{2.47}$$

Now we introduce the contravariant components of the four-momentum of the geodesic

$$\begin{aligned}
p^r &= \frac{dr}{d\lambda} = \Sigma^{-1}\sqrt{R(r)};\ p^\theta = \frac{d\theta}{d\lambda} = \Sigma^{-1}\sqrt{\Theta(\theta)};\\
p^\phi &= \frac{d\phi}{d\lambda} = \Sigma^{-1}\Delta^{-1}\left[2ar\mathcal{E} + \frac{L_z}{\sin^2\theta}\left(\Sigma - 2r\right)\right];\\
p^t &= \frac{dt}{d\lambda} = \Sigma^{-1}\Delta^{-1}\left(A\mathcal{E} - 2arL_z\right).
\end{aligned} \tag{2.48}$$

The covariant components of the geodesics four-momentum are then found via $p_\alpha = g_{\alpha\beta}p^\beta$

$$p_r = g_{rr}p^r = \frac{\sqrt{R(r)}}{\Delta};\ p_\theta = g_{\theta\theta}p^\theta = \sqrt{\Theta(\theta)};$$
$$p_\phi = g_{\phi t}p^t + g_{\phi\phi}p^\phi = L_z;\ p_t = g_{tt}p^t + g_{\phi t}p^\phi = -\mathcal{E}. \tag{2.49}$$

The relation between Carter constant, $Q$, and the covariant components of the photon four-momentum can be found simply by rearranging the expression for $p_\theta$ in the above

$$Q = p_\theta^2 + \cos^2\theta\left[a^2\left(\mu^2 - p_t^2\right) + \frac{p_\phi^2}{\sin^2\theta}\right]. \tag{2.50}$$

## 2.3 Null geodesics in Kerr metric

The path of photons (null geodesic) is completely described by three constants of motion: the total energy, $\mathcal{E}$, the azimuthal component of angular momentum, $L_z$, and Carter's constant, $Q$. For photons, null geodesics are relevant, and for them the number of free constants can be further reduced by renormalizing $L_z$ and $Q$ with respect to energy:

$$\lambda = \frac{L_z}{\mathcal{E}}, \tag{2.51}$$

$$q^2 = \frac{Q}{\mathcal{E}^2}. \tag{2.52}$$

From now, the parameter $\lambda$ has different meaning than it has in the definition of four-momentum $p^\mu$ (sec. 2.1). For photons propagating from the accretion disk towards a distant observer, the initial point is set at a given radius in the equatorial plane of the black hole, whereas the final point is at radial infinity, along the view angle of the observer.

Carter's equations for light rays are written in the integral form (Carter, 1968)

$$\int^r \frac{\mathrm{d}r}{\sqrt{R(r,\lambda,q^2)}} = \pm\int^\theta \frac{\mathrm{d}\theta}{\sqrt{\Theta(\theta,\lambda,q^2)}}, \tag{2.53}$$

where

$$R(r,\lambda,q^2) = r^4 + (a^2 - \lambda^2 - q^2)r^2 + 2[q^2 + (\lambda - a)^2]r - a^2q^2 \tag{2.54}$$

and

$$\Theta(\theta,\lambda,q^2) = q^2 + (a\cos\theta)^2 - (\lambda\cot\theta)^2. \tag{2.55}$$

Suppose the substitution $\mu = \cos\theta$ (from now, $\mu$ has another meaning than in sec. 2.1), then we can rewrite the equation (2.53) to the form

$$\int^r \frac{\mathrm{d}r}{\sqrt{R(r,\lambda,q^2)}} = \pm\int^\mu \frac{\mathrm{d}\mu}{\sqrt{\Theta(\mu,\lambda,q^2)}}, \tag{2.56}$$

where

$$\Theta(\mu, \lambda, q^2) = q^2 + (a^2 - \lambda^2 - q^2)\mu^2 - a^2\mu^4. \tag{2.57}$$

The dimensionless spin of the black hole, $a$, is in the range $-1 < a < 1$. The left-hand side of eq. (2.56) ($r$-integral) describes the motion in radial coordinates, while the right-hang side ($\theta$-integral) concerns the latitudinal motion. These equations can be integrated in terms of elliptical integrals (e.g. Rauch & Blandford, 1994; Čadež et al., 1998), more in chap. 3.

The two parameters $\lambda$ and $q^2$ are related very simply to the two impact parameters $\alpha$ and $\beta$ that describe the apparent position on the celestial sphere as seen by an observer at infinity who receives the light ray

$$\alpha = -\left(\frac{rp^\phi}{p^t}\right)_{r\to\infty} = -\frac{\lambda}{\sin\theta_\mathrm{o}} \tag{2.58}$$

and

$$\beta = \left(\frac{rp^\theta}{p^t}\right)_{r\to\infty} = (q^2 + a^2\cos^2\theta_\mathrm{o} - \lambda^2\cot\theta_\mathrm{o})^{1/2} = -p_{\theta_\mathrm{o}}, \tag{2.59}$$

where $\theta_\mathrm{o}$ is the angular coordinate of the observer at infinity. Each photon trajectory that reaches the observer is a point in the $(\alpha, \beta)$-plane.

The expression in eq. (2.54) can be rewritten in the form $R = (r - r_1)(r - r_2)(r - r_3)(r - r_4)$ (it is a polynomial of fourth order), where $r_1, r_2, r_3, r_4$ are the roots of $R(r) = 0$

$$r_{1,2} = \frac{1}{2}F \pm \frac{1}{2}(D_-)^{1/2},\ r_{3,4} = -\frac{1}{2}F \pm \frac{1}{2}(D_+)^{1/2}. \tag{2.60}$$

We denote constants:

$$A \equiv a^2 - \lambda^2 - q^2, \tag{2.61}$$

$$B \equiv (a - \lambda)^2 + q^2, \tag{2.62}$$

$$C \equiv A^2 - 12a^2q^2, \tag{2.63}$$

$$D \equiv 2A^3 + 72a^2q^2A + 108B^2, \tag{2.64}$$

$$E \equiv \frac{1}{3}\left[\left(\frac{D - Z}{2}\right)^{1/3} + \left(\frac{D + Z}{2}\right)^{1/3}\right];\ \text{for}\ (-4C^3 + D^2) > 0 \tag{2.65}$$

with $Z \equiv (-4C^3 + D^2)^{1/2}$, or

$$E \equiv \frac{2^{2/3}}{3}\left(D^2 + Z^2\right)^{1/6}\cos\varphi_a;\ \text{for}\ (-4C^3 + D^2) < 0 \tag{2.66}$$

with $Z = |-4C^3 + D^2|^{1/2}$ and $\varphi_a = \frac{1}{3}\arccos\frac{D}{(D^2+Z^2)^{1/2}}$,

$$F \equiv \left(-\frac{2}{3}A + E\right)^{1/2}, \tag{2.67}$$

$$G \equiv \lambda^2 + q^2 - a^2 \tag{2.68}$$

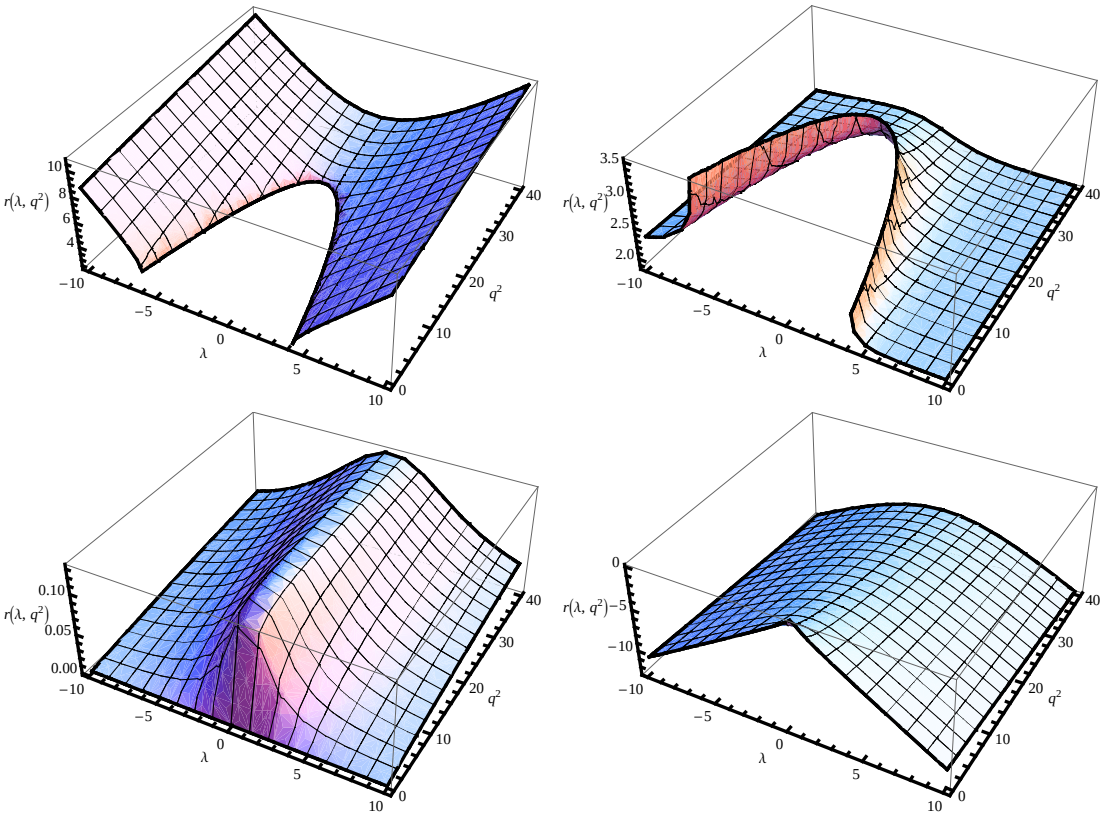


Figure 2.1: The roots $r_1(\lambda, q^2)$ (top left), $r_2(\lambda, q^2)$ (top right), $r_3(\lambda, q^2)$ (bottom left), $r_4(\lambda, q^2)$ (bottom right). All cases are shown for $a = 0.5$.

with $D_\pm \equiv -\frac{4}{3}A - E \pm \frac{4B}{F}$.

The roots $r_1$ and $r_2$ can be real or complex, while the roots $r_3$ and $r_4$ are always real. In case all roots are real, we suppose $r_1 > r_2 > r_3 > r_4$, if the two first are complex then $r_3 > r_4$. We can explain the behavior of the roots via fig. 2.1, where $a = 0.5$ ($r_\mathrm{h} \approx 1.866$; $r_\mathrm{ms} \approx 4.233$). We see that $r_4$ is negative and the value of $r_3$ is lower than the value of horizon event, eq. (2.9), so they have no physical significance. The behavior of the roots $r_1$ and $r_2$ is more complicated. There exists a region of $(\lambda, q^2)$ (the inner parts of the top graphs in the figure), for which the roots, $r_1$ and $r_2$, are complex. The real values of $r_2$ are greater than $r_\mathrm{h}$, but lower than $r_\mathrm{ms}$, and the values of $r_1$ are above $r_\mathrm{ms}$. Physically the real roots $r_1$ and $r_2$ represent the turning points of the radial motion. Because we consider the null geodesics with the emitting radius (or initial radius) $r_\mathrm{e}(\geq r_1) \geq r_\mathrm{ms}$, our photons can pass through one turning point at $r_1$ (if the roots are real) or do not pass (if they are complex). The behavior for other spins of black holes is similar, the roots have only different values.

The latitudinal motion distinguishes three cases $q^2 > 0$, $q^2 = 0$ and $q^2 < 0$. When $q^2 > 0$, the allowed range of $\mu^2$ is $0 \leq \mu^2 \leq \mu^2_\mathrm{max}$. It means that the orbits intersect the equatorial plane and oscillate symmetrically about it. The condition $q^2 = 0$ characterizes the trajectories in the equatorial plane. For the case $q^2 < 0$,

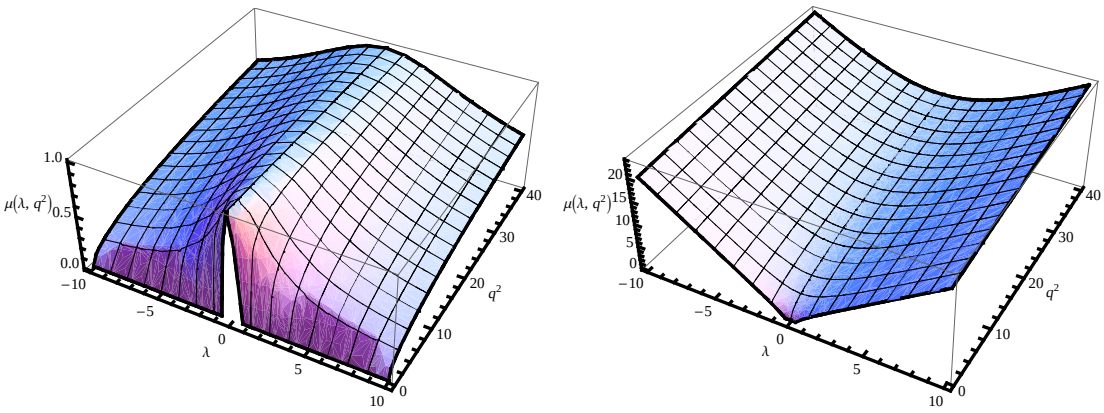


Figure 2.2: The roots $\mu_+(\lambda, q^2)$ (left), $\mu_-(\lambda, q^2)$ (right). All cases are shown for $a = 0.5$.

$\mu^2$ is restricted to an interval $0 < \mu_1^2 \leq \mu^2 \leq \mu_2^2 < 1$ (allowing the possibility that no such interval exists). In other words, the orbits do not intersect the equatorial plane and are confined between two coaxial cones.

We consider the case of $q^2 > 0$ then the expression in eq. (2.57) can be rewritten as $\Theta(\mu) = a^2(\mu_-^2 + \mu^2)(\mu_+^2 - \mu^2)$, where the roots are

$$\mu_\pm^2 = \frac{1}{2a^2}\left[(G^2 + 4a^2q^2)^{1/2} \mp G\right]; \ (0 \leq \mu^2 \leq \mu_+^2). \tag{2.69}$$

The behavior of the roots is shown in fig. 2.2. One root takes always the values in range $0 < \mu_+ < 1$ and physically it is the turning point in the latitudinal direction. The second one ($\mu_-$) has no physically significance for us.

# Chapter 3

# Carter's equations in form of elliptic integrals

Carter's equations of null geodesics in eq. (2.56) can be expressed in a form of an elliptic integral of the first kind (e.g. Rauch & Blandford, 1994; Čadež et al., 1998) that we define as

$$F(\varphi, k) = \int_0^{\varphi} \frac{\mathrm{d}\vartheta}{\sqrt{1 - k\sin^2\vartheta}}, \tag{3.1}$$

and in a form of a complete elliptic integral of the first kind that we define as

$$F\left(\frac{\pi}{2}, k\right) = K(k) = \int_0^{\frac{\pi}{2}} \frac{\mathrm{d}\vartheta}{\sqrt{1 - k\sin^2\vartheta}}. \tag{3.2}$$

For completeness, we define an elliptic integral of the second kind as

$$E(\varphi, k) = \int_0^{\varphi} \sqrt{1 - k\sin^2\vartheta}\,\mathrm{d}\vartheta. \tag{3.3}$$

The detailed information about the elliptic integrals are in Abramowitz & Stegun (1965), Byrd & Friedman (1971) and Gradshteyn & Ryzhik (1971). We point out that our notation differs from the definitions in books cited above. The reason was to be consistent with procedures in program Wolfram's Mathematica (Wellin et al., 2005).

We separate eq. (2.56) into two different parts: the radial direction ($r$-integral) and latitudinal direction of the null geodesic ($\theta$-integral). The expressed form depends on the roots of the polynomial $R(r, \lambda, q^2)$, eq. (2.54), (real or complex) and on the path of photons (passes through the turning point or does not).

## 3.1 Radial motion, four real roots

The path in a radial direction is divided into two parts: (i) $r_{\mathrm{e}} \to \infty$ (the lower sign in eq. (3.4)), the path from an emitting point, $r_{\mathrm{e}}$, to the observer at the

radial infinity, $r_{\rm o}=\infty$; (ii) $r_{\rm e}\to r_1\to\infty$ (the upper sign in eq. (3.4)), the path from an emitting radius to the turning point, $r_1$, and then to the observer

$$\int\limits_{r_{\rm e}}^{\infty}\frac{{\rm d}r}{\sqrt{R(r,\lambda,q^2)}}=\int\limits_{r_1}^{\infty}\frac{{\rm d}r}{\sqrt{R(r,\lambda,q^2)}}\pm\int\limits_{r_1}^{r_{\rm e}}\frac{{\rm d}r}{\sqrt{R(r,\lambda,q^2)}}. \tag{3.4}$$

If $R(r,\lambda,q^2)=(r-r_1)(r-r_2)(r-r_3)(r-r_4)$ and $r_1>r_2>r_3>r_4$ then the integrals in eq. (3.4) can be expressed as

$$\int\limits_{r_1}^{\infty}\frac{{\rm d}r}{\sqrt{R(r,\lambda,q^2)}}=g_rF(\varphi_{\rm o},k_r) \tag{3.5}$$

and

$$\int\limits_{r_1}^{r_{\rm e}}\frac{{\rm d}r}{\sqrt{R(r,\lambda,q^2)}}=g_rF(\varphi_{\rm e},k_r), \tag{3.6}$$

where

$$g_r(\lambda,q^2)=\frac{2}{\sqrt{(r_1-r_3)(r_2-r_4)}}, \tag{3.7}$$

$$k_r(\lambda,q^2)=\frac{(r_2-r_3)(r_1-r_4)}{(r_1-r_3)(r_2-r_4)}, \tag{3.8}$$

$$\varphi_{\rm o}(\lambda,q^2)=\arcsin\left[\frac{(r_2-r_4)(r_{\rm o}-r_1)}{(r_1-r_4)(r_{\rm o}-r_2)}\right]^{1/2}\overset{r_{\rm o}\to\infty}{=}\arcsin\left(\frac{r_2-r_4}{r_1-r_4}\right)^{1/2} \tag{3.9}$$

and

$$\varphi_{\rm e}(\lambda,q^2)=\arcsin\left[\frac{(r_2-r_4)(r_{\rm e}-r_1)}{(r_1-r_4)(r_{\rm e}-r_2)}\right]^{1/2}. \tag{3.10}$$

Finally, the expression of eq. (3.4) via the elliptical integrals is

$$\int\limits_{r_{\rm e}}^{\infty}\frac{{\rm d}r}{\sqrt{R(r,\lambda,q^2)}}=g_r[F(\varphi_{\rm o},k_r)\pm F(\varphi_{\rm e},k_r)]. \tag{3.11}$$

The upper sign in eq. (3.11) refers to the case of light rays passing through a turning point in the radial directions; the lower sign refers to those with no radial turning point.

## 3.2 Radial motion, two complex roots

In case the polynomial $R(r,\lambda,q^2)$ has two complex $r_{1,2}=u\pm{\rm i}v$, where $u=\frac{1}{2}F$, $v=\frac{1}{2}|D_-|^{1/2}$, and two real roots $r_3>r_4$ then the radial integral adopts the form

$$\int\limits_{r_{\rm e}}^{\infty}\frac{{\rm d}r}{\sqrt{R(r,\lambda,q^2)}}=g_{rc}\big[F(\varphi_{\rm oc},k_{rc})-F(\varphi_{\rm ec},k_{rc})\big], \tag{3.12}$$

where

$$g_{rc}(\lambda, q^2) = \frac{1}{\sqrt{A_c B_c}}, \tag{3.13}$$

$$k_{rc}(\lambda, q^2) = \frac{(A_c + B_c)^2 - (r_3 - r_4)^2}{4 A_c B_c}, \tag{3.14}$$

$$\varphi_{oc}(\lambda, q^2) = \arccos\left[\frac{A_c - B_c}{A_c + B_c}\right], \tag{3.15}$$

$$\varphi_{ec}(\lambda, q^2) = \arccos\left[\frac{(A_c - B_c) r_e + r_3 B_c - r_4 A_c}{(A_c + B_c) r_e - r_3 B_c - r_4 A_c}\right], \tag{3.16}$$

$$A_c(\lambda, q^2) = \left[(r_3 - u)^2 + v^2\right]^{1/2} \tag{3.17}$$

and

$$B_c(\lambda, q^2) = \left[(r_4 - u)^2 + v^2\right]^{1/2}. \tag{3.18}$$

These paths do not pass through the turning points in radial direction because the turning points do not exist (they are complex).

## 3.3 Latitudinal motion

The latitudinal integral can be written in the form

$$\int_0^{\mu_e} \frac{\mathrm{d}\mu}{\sqrt{\Theta(\mu, \lambda, q^2)}} = \frac{g_\mu}{|a|} F(\psi, k_\mu), \tag{3.19}$$

assuming that the light ray has no latitudinal turning point. Otherwise, the appropriate form of the integral is

$$\int_0^{\mu_e} \frac{\mathrm{d}\mu}{\sqrt{\Theta(\mu, \lambda, q^2)}} = \frac{g_\mu}{|a|} [2K(k_\mu) - F(\psi, k_\mu)], \tag{3.20}$$

where

$$g_\mu(\lambda, q^2) = \frac{1}{\sqrt{\mu_+^2 + \mu_-^2}}, \tag{3.21}$$

$$k_\mu(\lambda, q^2) = \frac{\mu_+^2}{\mu_+^2 + \mu_-^2}, \tag{3.22}$$

$$\psi(\lambda, q^2) = \arcsin\left[\frac{\mu_o^2(\mu_+^2 + \mu_-^2)}{\mu_+^2(\mu_o^2 + \mu_-^2)}\right]^{1/2}. \tag{3.23}$$

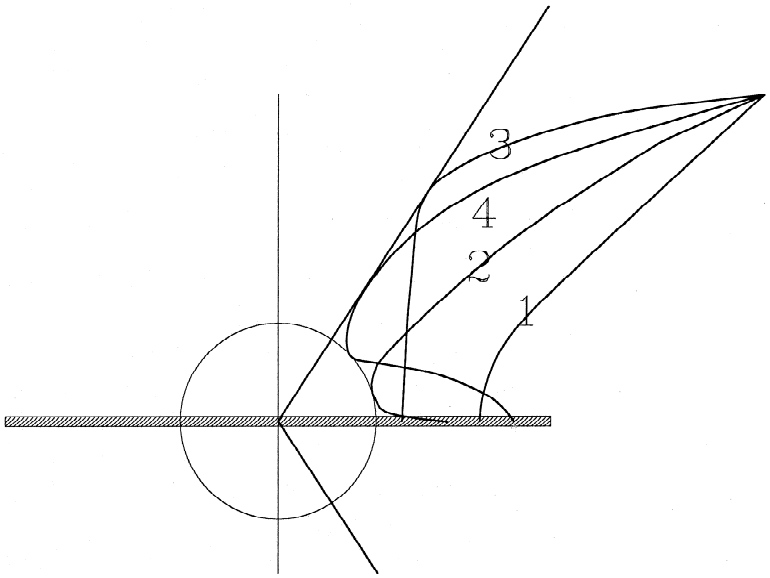


Figure 3.1: The projection of photon trajectories in the $(r, \theta)$-plane is schematically shown for the 4 relevant cases. They depend on the presence of radial and/or latitudinal turning points in the trajectory from the accretion disk to the far observer: (1) no turning points; (2) one radial turning point; (3) one latitudinal turning point; (4) both radial and latitudinal turning points. Taken from Čadež et al. (1998).

## 3.4 Solution of Carter's equations

The explicit form of the Carter's equations (2.56) depends on the roots of the polynomials in denominator and on path of photons we consider. Therefore, we divide the Carter's equations into four types:
(i) no turning points; it is the combination of eqs. (3.11) (lower sign) and (3.19)

$$g_r[F(\varphi_{\rm o}, k_r) - F(\varphi_{\rm e}, k_r)] - \frac{g_\mu}{|a|} F(\psi, k_\mu) = 0 \tag{3.24}$$

or for complex roots it is the combination of eqs. (3.12) and (3.19)

$$g_{rc}\big[F(\varphi_{\rm oc}, k_{rc}) - F(\varphi_{\rm ec}, k_{rc})\big] - \frac{g_\mu}{|a|} F(\psi, k_\mu) = 0; \tag{3.25}$$

(ii) one radial turning point; the combination of eqs. (3.11) (upper sign) and (3.19)

$$g_r[F(\varphi_{\rm o}, k_r) + F(\varphi_{\rm e}, k_r)] - \frac{g_\mu}{|a|} F(\psi, k_\mu) = 0; \tag{3.26}$$

(iii) one latitudinal turning point; the combination of eqs. (3.11) (lower sign) and (3.20)

$$g_r[F(\varphi_{\rm o}, k_r) - F(\varphi_{\rm e}, k_r)] - \frac{g_\mu}{|a|} [2K(k_\mu) - F(\psi, k_\mu)] = 0 \tag{3.27}$$

or for complex roots with the combination of eqs. (3.12) and (3.20)

$$g_{rc}\big[F(\varphi_{\rm oc},k_{\rm rc})-F(\varphi_{\rm ec},k_{\rm rc})\big]-\frac{g_\mu}{|a|}[2K(k_\mu)-F(\psi,k_\mu)]=0; \tag{3.28}$$

(iv) both radial and latitudinal turning points; the combination of eqs. (3.11) (upper sign) and (3.20)

$$g_r[F(\varphi_{\rm o},k_r)+F(\varphi_{\rm e},k_r)]-\frac{g_\mu}{|a|}[2K(k_\mu)-F(\psi,k_\mu)]=0. \tag{3.29}$$

These types of null geodesics are schematically represented in fig. 3.1.

The solution of Carter's equations is a set of all possible pairs $(\lambda,q^2)$ satisfying eqs. (3.24)–(3.29). The graphs in figs. 3.2–3.5 represent these pairs of $(\lambda,q^2)$ depending on the type of null geodesics and the choice of the parameters, the spin of the black hole, $a$, emitting radius, $r_{\rm e}$, and view angle of the observer, $\mu_{\rm o}=\cos\theta_{\rm o}$. The different types of the null geodesics are described by colors in the graphs.

We can see from figs. 3.2–3.4 that the solutions are closed curves with a shape depending on the spin of a black hole, the emitting point and the view angle of an observer. The shape of the curves is almost symmetric around $\lambda=0$ for nonrotating black holes and slightly shifted to right from $\lambda=0$ for negative spins. The spins $a>0$ cause the deformation of the curves and the shift to negative values of $\lambda$.

The range of $(\lambda,q^2)$ gets smaller for increasing spins and decreasing view angles of an observer when the emitting radius is fixed. For example, if we compare the curves of the view angle 78 deg for $a=-0.99$ and $a=0.99$ in figs. 3.2 and 3.4, we can notice that the ranges are $-10\lesssim\lambda\lesssim 10$ and $0\lesssim q^2\lesssim 65$ for $a=-0.99$ while for $a=0.99$ it is only $-4\lesssim\lambda\lesssim 2$ and $0\lesssim q^2\lesssim 16$. For rotating black holes with greater spin, the effects of the gravity are stronger (marginally stable orbit is closer to the horizon) and only minor amount of photons can reach an observer.

The intersections of null geodesics in figs. 3.2–3.4 describe photons with the same constants of motion $(\lambda,q^2)$ but they reach the observers with different view angles and also they are moving on different null geodesics. For example, if we consider a solution of Carter's equations for the view angle of the observer 25 deg (in graphs for $a=-0.50$ and $a=0.01$), it has the intersections with solutions for 45 deg, 60 deg and 78 deg. The photon moving on the geodesic without turning points will reach an observer with the inclination 25 deg, but a photon with same constants of motion $(\lambda,q^2)$ and moving on the geodesic with both radial and latitudinal turning points will reach an observer with the inclination 78 deg. Specially, the graphs for $a=0.50$ and $a=70$ show us that some parts of the solution can be close to each other for different view angles, the values of $(\lambda,q^2)$ are similar but the observers are lying on distinct inclinations. The contours for $a=0.99$ have no intersections and the photons move only on two types of geodesics: without turning point and with one turning point in latitudinal direction; the complex roots of $R(r,\lambda,q^2)$ are dominant.

The solution with $q^2$ near zero describes photons moving close to the equatorial plane of the black hole. It is noticeable for great view angles.

It is obvious from fig. 3.5 that the range of solution of $(\lambda, q^2)$ is wider for increasing values of emitting radius. When the photon is emitted very close to the black hole, it can reach an observer only on geodesics with complex roots of $R(r, \lambda, q^2)$ while the photons emitted in greater distance are moving on geodesics with real roots of $R(r, \lambda, q^2)$. In this case, the intersections describe photons with identical $(\lambda, q^2)$ that always reach an observer with the same view angle but the photons start at different emitting radii and move on different geodesics.

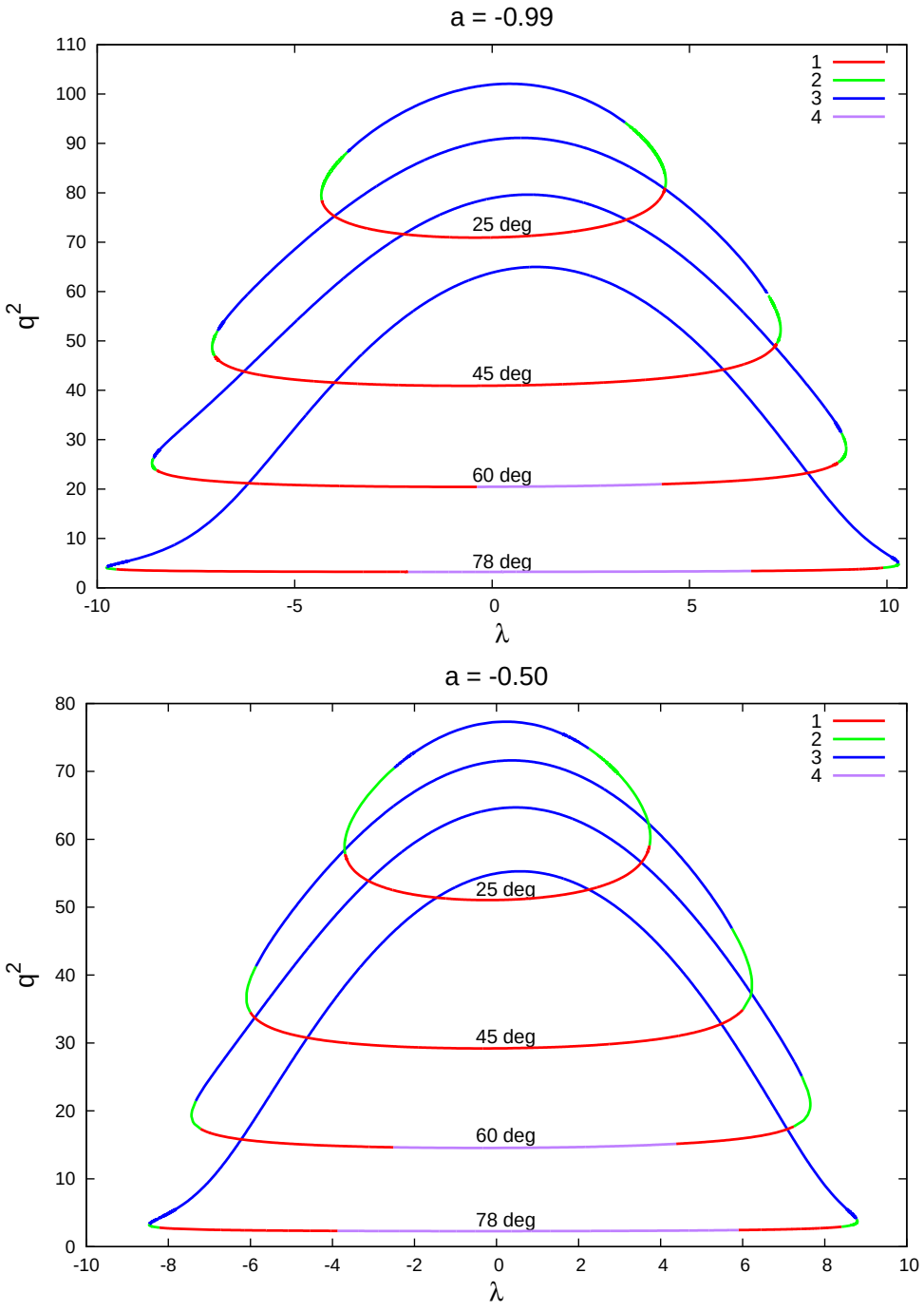


Figure 3.2: The graphical representation of the solution of Carter's equations for different spins of the black hole (given on top of each panel). The colors represent five types of null geodesics: red (1) and purple (4) are without turning points; green (2) and brown (5) with one latitudinal turning point; blue (3) with both radial and latitudinal turning points. The geodesics 1–3 have real roots and 4,5 have complex roots of $R(r, \lambda, q^2)$. The contours were calculated for view angles 25 deg, 45 deg, 60 deg, 78 deg; and the emitting radius corresponds to the marginally stable orbit of the appropriate spin ($a = -0.99, -0.50$). Negative values of spin correspond to the case of a counter-rotating black hole.

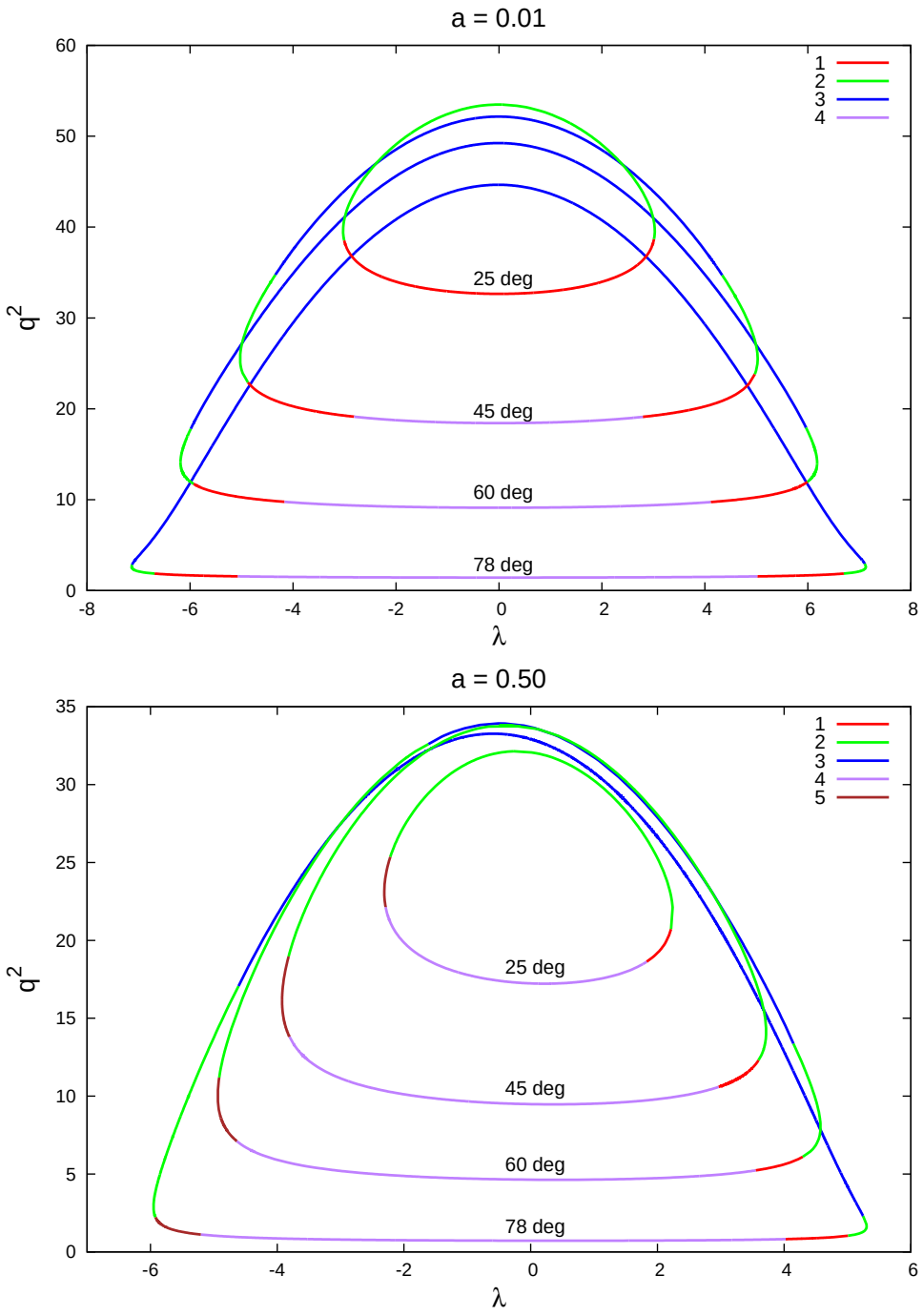


Figure 3.3: As in the previous figure, but for positive spins ($a = 0.01, 0.50$) of the black hole (co-rotating).

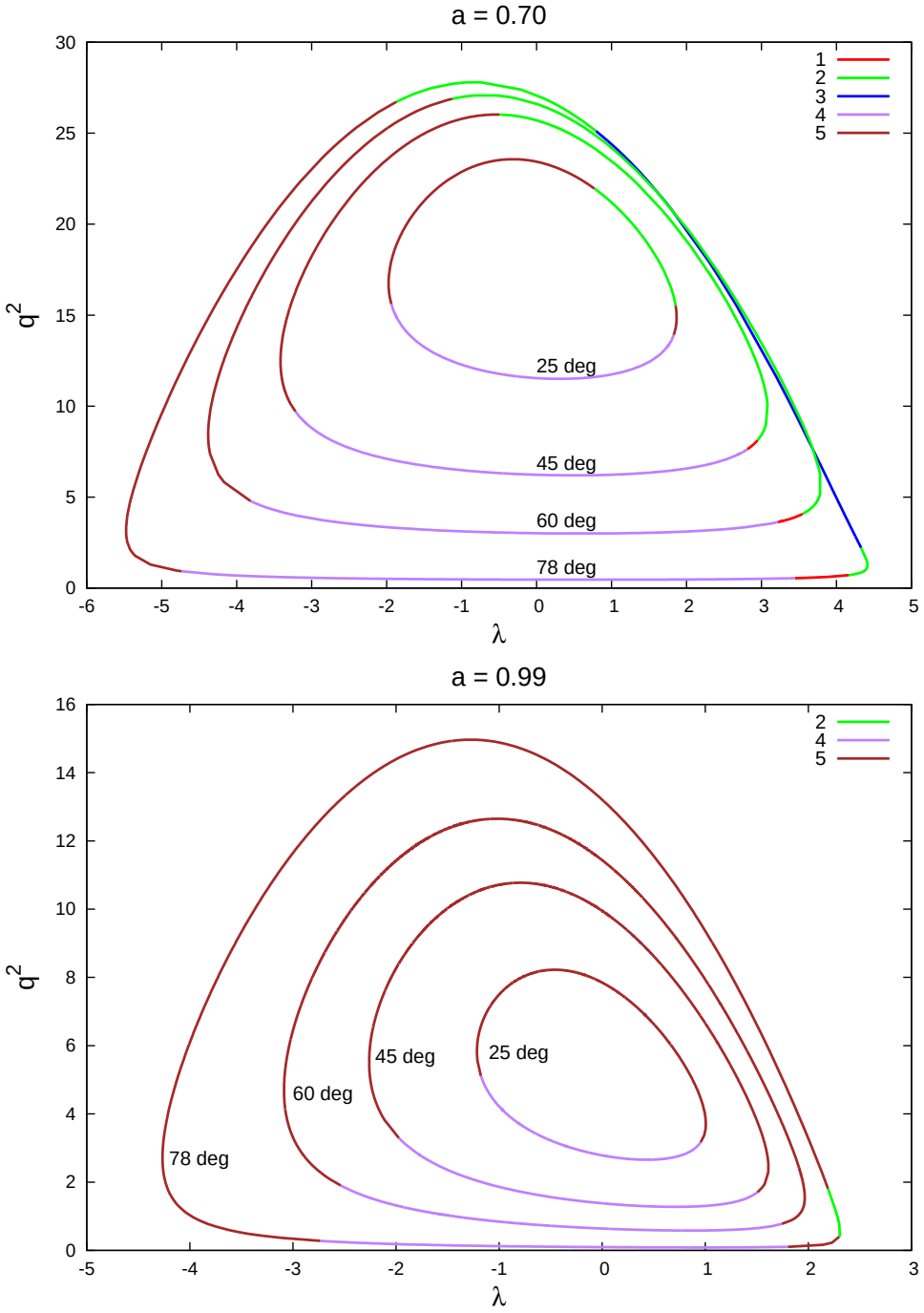


Figure 3.4: As in the previous figure, but for greater spins ($a = 0.70, 0.99$) of the black hole. The case of $a = 0.99$ corresponds to the almost maximally rotating black hole in the prograde orientation.

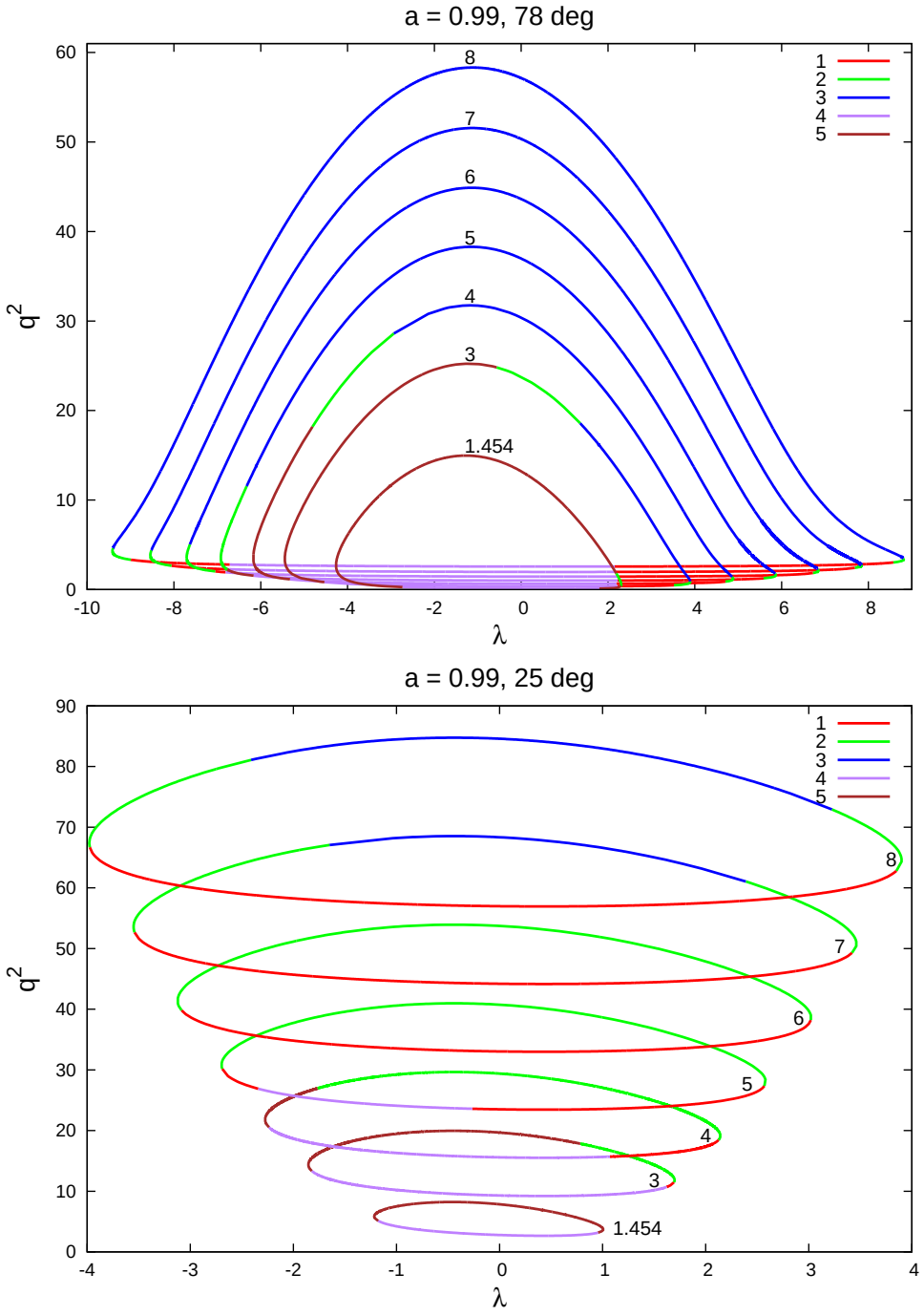


Figure 3.5: The graphical representation of the solution of Carter's equations for fixed spin (a = 0.99) and two inclination $\theta_o = 25, 78$ deg (given on top of each panel). The colors represent five types of null geodesics as in the previous figures. The contours were calculated for emitting radii: $r_{em} = r_{ms}$ ($\doteq 1.454$), 3, 4, 5, 6, 7, 8.

# Chapter 4

# Photon energy shifts in Kerr metric

## 4.1 Energy shifts

The energy shift, $g$, is defined as a ratio between an observed, $\mathcal{E}_{\rm o}$, and emitted, $\mathcal{E}_{\rm e}$, photon energy (or as a ratio between an observed, $\nu_{\rm o}$, and emitted, $\nu_{\rm e}$, frequency):

$$g = \frac{(p_\mu u^\mu)_{\rm o}}{(p_\mu u^\mu)_{\rm e}} = \frac{\mathcal{E}_{\rm o}}{\mathcal{E}_{\rm e}} = \frac{\nu_{\rm o}}{\nu_{\rm e}}. \tag{4.1}$$

The four-velocity of the emission source is $\mathbf{u}_{\rm e} = (u^t, 0, 0, u^\phi) = u^t(1, 0, 0, \frac{u^\phi}{u^t} = \Omega)$, where

$$u^t = \left[1 - \frac{2r_{\rm e}}{\Sigma}(1 - a\Omega\sin^2\theta_{\rm e})^2 - (r_{\rm e}^2 + a^2)\Omega^2\sin^2\theta_{\rm e}\right]^{-1/2}, \tag{4.2}$$

and $\Omega$ is angular velocity of the particle, introduced in eq. (2.23). The observer is assumed to be located at rest at infinity with the four-velocity $\mathbf{u}_{\rm o} = (1, 0, 0, 0)$. Then the ratio $g$ can be expressed as

$$g = \frac{p_t}{p_t u^t + p_\phi u^\phi} = \frac{p_t}{p_t u^t(1 + \frac{p_\phi u^\phi}{p_t u^t})} = \frac{1}{u^t}\frac{1}{1 - \lambda\Omega}, \tag{4.3}$$

where the covariant components of the four-momentum $p_\alpha$ are defined in eqs. (2.49) and $\lambda$ is the combination of two constants of motion (the azimuthal component of angular momentum, $L_z$, and the total energy, $\mathcal{E}$,): $\frac{p_\phi}{p_t} = -\frac{L_z}{\mathcal{E}} = -\lambda$, eq. (2.51).

## 4.2 Extremal energy shifts

We look for extremal values of the function (4.3). The extremes of the redshift function $g$ are not so easy to write in an analytical way. Let us remark that an elegant way of determining the energy shifts was derived by Schee et al. (2005) in terms of the light emission loss cone. However, their approach allows only to find the extremal energy shifts of all photons emitted from the source at a given position. This includes also those which follow indirect light rays and cross the

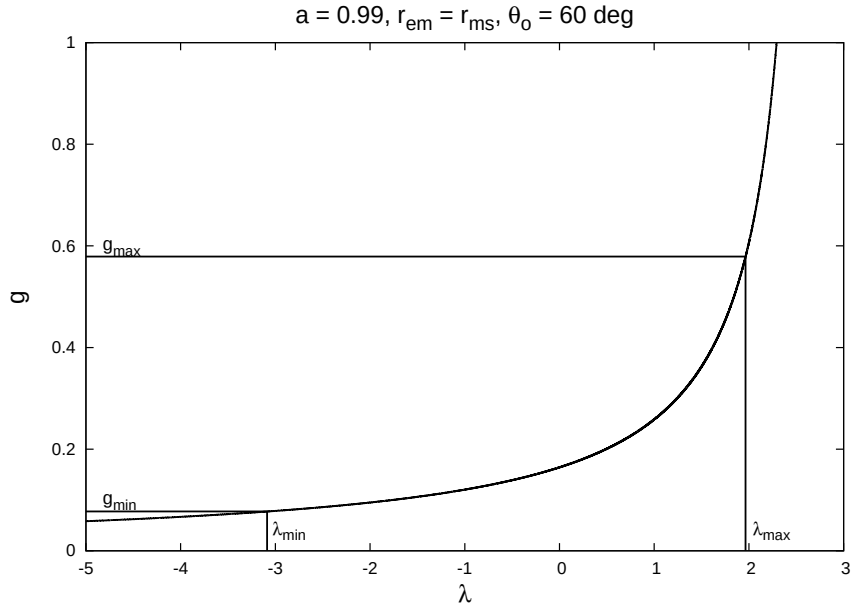


Figure 4.1: The behavior of $g(\lambda)$ with $a = 0.99$, $r_{\rm e} = r_{\rm ms}$ and $\theta_{\rm o} = 60$ deg.

disk plane. Although the family of direct light rays have generally a simpler shape than the indirect rays, the additional condition prevents us from using the loss cone method to determine the range of energy shifts for a source in the accretion disk.

The definition domain of the energy shift as a function of specific angular momentum, $g(\lambda) \sim -\frac{1}{\lambda}$ (monotonically increasing), is an interval $\langle \lambda_{\rm min}, \lambda_{\rm max} \rangle$ that is constrained by the condition of photon reaching the observer, eq. (2.56). Then the minimum of the energy shift, $g_{\rm min}$, corresponds to $\lambda_{\rm min}$, and the maximum, $g_{\rm max}$, to $\lambda_{\rm max}$. Fig. 4.1 shows an example of dependence of the energy shift, $g(\lambda)$, on $\lambda$. The behavior is plotted for a special case of $a = 0.99$, $r_{\rm e} = r_{\rm ms}$ and $\theta_{\rm o} = 60$ deg. The definition domain $\langle \lambda_{\rm min}, \lambda_{\rm max} \rangle$ was calculated by the semi-analytical method that is introduced in the next subsections.

### 4.2.1 Searching extremal shifts via method of Lagrange multipliers

We search for extremal values $g_{\rm min}$, $g_{\rm max}$ of the redshift function (4.3), under a simultaneous constraint by eq. (2.56). In general, Lagrange multipliers provide a suitable strategy for finding the constrained extremal values of function $f(x_1, .., x_n)$ with the constraint $h(x_1, .., x_n) = 0$. The Lagrangian is defined as

$$\Lambda(x_1, .., x_n, \alpha) = f(x_1, .., x_n) - \alpha h(x_1, .., x_n), \tag{4.4}$$

where $\alpha$ are Lagrange multipliers. The partial derivatives of the Lagrange function $\Lambda(x_1,..,x_n,\alpha)$ with respect to $x_1,..,x_n$ and $\alpha$ must vanish identically

$$\begin{aligned}\frac{\partial}{\partial x_1}\Lambda(x_1,..,x_n,\alpha) &= 0\\ &\cdot\\ &\cdot\\ \frac{\partial}{\partial x_n}\Lambda(x_1,..,x_n,\alpha) &= 0\\ \frac{\partial}{\partial \alpha}\Lambda(x_1,..,x_n,\alpha) &= 0.\end{aligned} \tag{4.5}$$

There are $n+1$ unknowns for $n+1$ equations.

In our case, the function $f(x_1,..,x_n)$ corresponds to the energy shift $g(\lambda)$, eq. (4.3), and the constraint $h(x_1,..,x_n)$ to Carter's equation, eq. (2.56), then the Lagrangian is

$$\Lambda(\lambda,q^2,\alpha)=\frac{1}{u^t}\frac{1}{1-\lambda\Omega}-\alpha\int_{r_e}^{\infty}\frac{\mathrm{d}r}{\sqrt{R(r,\lambda,q^2)}}+\alpha\int_{0}^{\mu_o}\frac{\mathrm{d}\mu}{\sqrt{\Theta(\mu,\lambda,q^2)}}, \tag{4.6}$$

and its partial derivatives are

$$\begin{aligned}\frac{\partial}{\partial\lambda}\Lambda(\lambda,q^2,\alpha) &= \frac{1}{u^t}\frac{\Omega}{(1-\lambda\Omega)^2}\\ &- \alpha\frac{\partial}{\partial\lambda}\left[\int_{r_e}^{\infty}\frac{\mathrm{d}r}{\sqrt{R(r,\lambda,q^2)}}-\int_{0}^{\mu_o}\frac{\mathrm{d}\mu}{\sqrt{\Theta(\mu,\lambda,q^2)}}\right]=0;\\ \frac{\partial}{\partial q^2}\Lambda(\lambda,q^2,\alpha) &= \alpha\frac{\partial}{\partial q^2}\left[\int_{r_e}^{\infty}\frac{\mathrm{d}r}{\sqrt{R(r,\lambda,q^2)}}-\int_{0}^{\mu_o}\frac{\mathrm{d}\mu}{\sqrt{\Theta(\mu,\lambda,q^2)}}\right]=0;\\ \frac{\partial}{\partial q^2}\Lambda(\lambda,q^2,\alpha) &= \int_{r_e}^{\infty}\frac{\mathrm{d}r}{\sqrt{R(r,\lambda,q^2)}}-\int_{0}^{\mu_o}\frac{\mathrm{d}\mu}{\sqrt{\Theta(\mu,\lambda,q^2)}}=0.\end{aligned} \tag{4.7}$$

The second condition in eq. (4.7) yields two possibilities: $\alpha=0$ or $\alpha\neq 0$. In the case, $\alpha=0$ we get two equations

$$\frac{1}{u^t}\frac{\Omega}{(1-\lambda\Omega)^2}=0 \tag{4.8}$$

and

$$\int_{r_e}^{\infty}\frac{\mathrm{d}r}{\sqrt{R(r,\lambda,q^2)}}-\int_{0}^{\mu_o}\frac{\mathrm{d}\mu}{\sqrt{\Theta(\mu,\lambda,q^2)}}=0. \tag{4.9}$$

The first one has no solution. The second one is Carter equation that has the solution as a set of pairs $(\lambda,q^2)$. These solutions are presented in chap. 3.

If we consider $\alpha \neq 0$, eqs. (4.7) yield two coupled equations for the unknowns $\lambda$ and $q^2$

$$f_1 = \int_{r_\mathrm{e}}^{\infty} \frac{\mathrm{d}r}{\sqrt{R(r,\lambda,q^2)}} - \int_0^{\mu_\mathrm{o}} \frac{\mathrm{d}\mu}{\sqrt{\Theta(\mu,\lambda,q^2)}} = 0 \tag{4.10}$$

and

$$f_2 = \frac{\partial f_1}{\partial q^2} = \frac{\partial}{\partial q^2}\left[\int_{r_\mathrm{e}}^{\infty} \frac{\mathrm{d}r}{\sqrt{R(r,\lambda,q^2)}} - \int_0^{\mu_\mathrm{o}} \frac{\mathrm{d}\mu}{\sqrt{\Theta(\mu,\lambda,q^2)}}\right] = 0. \tag{4.11}$$

The values of $\lambda$ conforming to eqs. (4.10)–(4.11) correspond to the desired extremes of the energy shift, $g(\lambda)$. Unfortunately, the functions $f_1$ and $f_2$ in eqs. (4.10) and (4.11) cannot be solved analytically, and therefore we used a numerical method to perform the final step in evaluating the extremal values of $g$. The method is called Newton-Raphson (Press et al., 2007) and we present it in the next subsection.

### 4.2.2 Final step in evaluating extremes of shift

In order to evaluate the extremal values of $g$, we solve the set (4.10), (4.11) using the Newton-Raphson method. To this end we write Taylor expansion about the root neighborhood,

$$\begin{aligned} f_1(\lambda,q^2) = 0 \;&=\; f_1(\lambda_\mathrm{n},q_\mathrm{n}^2) + (\lambda-\lambda_\mathrm{n})\frac{\partial f_1}{\partial\lambda}(\lambda_\mathrm{n},q_\mathrm{n}^2) + (q^2-q_\mathrm{n}^2)\frac{\partial f_1}{\partial q^2}(\lambda_\mathrm{n},q_\mathrm{n}^2) \\ &+\; \mathcal{O}(\lambda-\lambda_\mathrm{n})^2 + \mathcal{O}(q^2-q_\mathrm{n}^2)^2, \end{aligned} \tag{4.12}$$

$$\begin{aligned} f_2(\lambda,q^2) = 0 \;&=\; f_2(\lambda_\mathrm{n},q_\mathrm{n}^2) + (\lambda-\lambda_\mathrm{n})\frac{\partial f_2}{\partial\lambda}(\lambda_\mathrm{n},q_\mathrm{n}^2) + (q^2-q_\mathrm{n}^2)\frac{\partial f_2}{\partial q^2}(\lambda_\mathrm{n},q_\mathrm{n}^2) \\ &+\; \mathcal{O}(\lambda-\lambda_\mathrm{n})^2 + \mathcal{O}(q^2-q_\mathrm{n}^2)^2, \end{aligned} \tag{4.13}$$

where $n$ is the order of the expansion (to be determined by the desired accuracy of the solution). We define $\Delta\lambda_\mathrm{n} = \lambda - \lambda_\mathrm{n}$ and $\Delta q_\mathrm{n}^2 = q^2 - q_\mathrm{n}^2$ to obtain two relations for $\Delta\lambda_\mathrm{n}$ and $\Delta q_\mathrm{n}^2$,

$$\Delta\lambda_\mathrm{n}\frac{\partial f_1}{\partial\lambda}(\lambda_\mathrm{n},q_\mathrm{n}^2) + \Delta q_\mathrm{n}^2\frac{\partial f_1}{\partial q^2}(\lambda_\mathrm{n},q_\mathrm{n}^2) \approx -f_1(\lambda_\mathrm{n},q_\mathrm{n}^2), \tag{4.14}$$

$$\Delta\lambda_\mathrm{n}\frac{\partial f_2}{\partial\lambda}(\lambda_\mathrm{n},q_\mathrm{n}^2) + \Delta q_\mathrm{n}^2\frac{\partial f_2}{\partial q^2}(\lambda_\mathrm{n},q_\mathrm{n}^2) \approx -f_2(\lambda_\mathrm{n},q_\mathrm{n}^2), \tag{4.15}$$

where

$$\Delta q_\mathrm{n}^2 = \frac{f_1 f_2^\lambda - f_2 f_1^\lambda}{f_1^\lambda f_2^{q^2} - f_1^{q^2} f_2^\lambda}, \tag{4.16}$$

$$\Delta\lambda_\mathrm{n} = \frac{-f_1 - \Delta q_\mathrm{n}^2 f_1^{q^2}}{f_1^\lambda}, \tag{4.17}$$

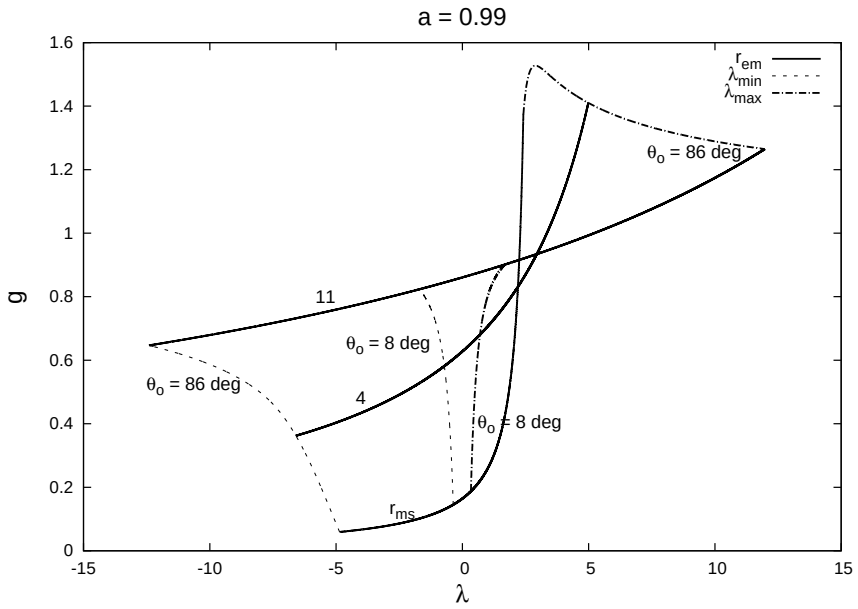


Figure 4.2: The behavior of $g(\lambda)$ for $a = 0.99$. The solid lines represent energy shifts for constant radii, the dashed lines correspond to constant view angles.

the upper indexes, $\lambda$ and $q^2$, mean the first derivatives with respect to $\lambda$, respectively $q^2$.

Eqs. (4.14)–(4.15) are linear in $\Delta\lambda_{\rm n}$ and $\Delta q^2_{\rm n}$. The solution can be found by successive iterations,

$$\lambda_{\rm n+1} = \lambda_{\rm n} + \Delta\lambda_{\rm n}, \quad q^2_{\rm n+1} = q^2_{\rm n} + \Delta q^2_n. \tag{4.18}$$

The energy shift, $g$ in eq. (4.3), depends on $a$ (spin of a black hole), $r_{\rm em}$ (emitting radius) and $\lambda$ (the combination of the azimuthal component of angular momentum and the total energy). The solution $(\lambda, q^2)$ of Carter's equations, eq. (2.56), depends on $a$, $r_{\rm em}$ and $\theta_{\rm o}$ (view angle of an observer). Because $\lambda$ is given from the Carter's equations, the energy shift depends implicitly also on $\theta_{\rm o}$.

Figs. 4.2 and 4.3 show us the behavior of $g(\lambda)$ according to $r_{\rm em}$ and $\theta_{\rm o}$ when the spin is fixed. The solid lines represent all energy shifts and its shape depends on the value of the emitting radius, dashed lines determine the minimum and maximum of $\lambda$ (they correspond to extremal values of $g$) and depend on $\theta_{\rm o}$. The energy shift achieves the minimal values for the marginally stable orbit and for inclinations near the equatorial plane while the maximum is achieved for radii a little greater than $r_{\rm em}$ (only for case $a = 0.99$). We can also notice that the width of the line is very narrow for the view along the rotating axis of the black hole. The minimum changes slightly for constant radii while the difference of maximum between $\theta_{\rm o} = 8$ deg and $\theta_{\rm o} = 86$ deg is significant. If we compare figs. 4.2 and 4.3, we see that the behavior of $g$ does not differ for different spins and large radii.

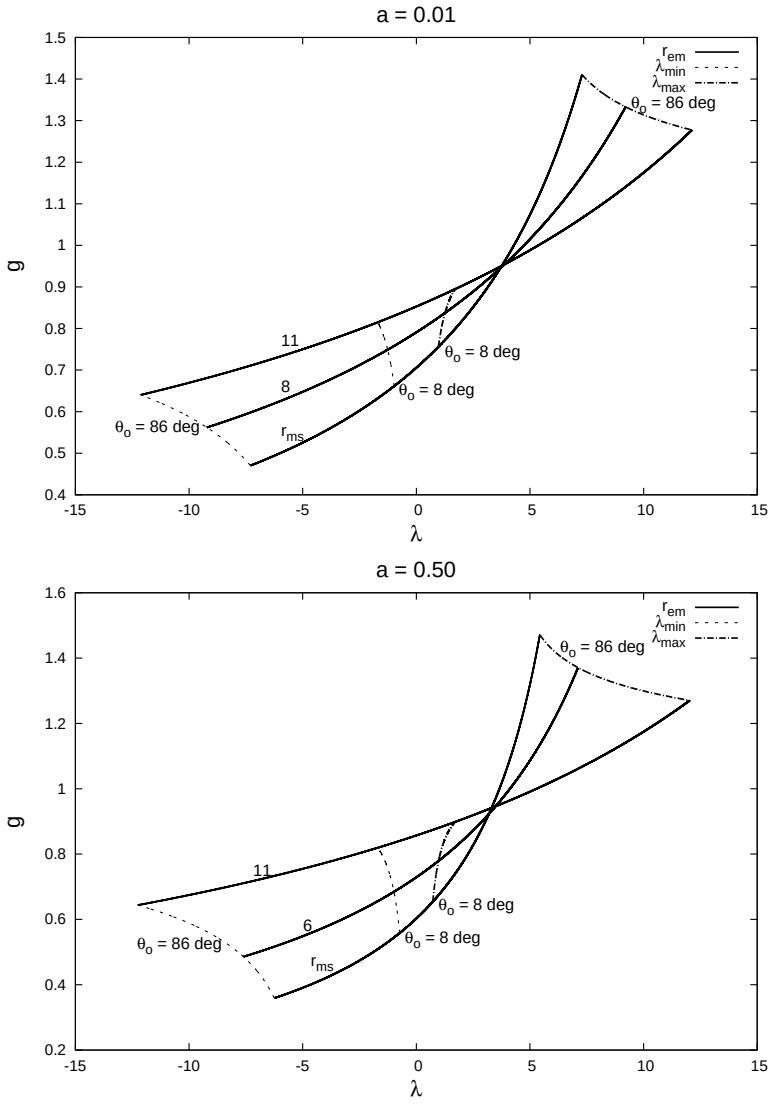


Figure 4.3: As in the previous figure, but for spins $a = 0.01$ and $a = 0.50$.

### 4.2.3 Graphical representation of results

Results are plotted in figs. 4.6–4.9, where we show the extremal shifts as a function of the two main parameters: (i) dimensionless spin of the black hole ($-1 \leq a \leq 1$); and (ii) emission radius, $r_{\rm em}$, of the ring ($r_{\rm ms} \leq r_{\rm em}$, expressed in units of gravitational radii). The inclination angle, $\theta_{\rm o}$, stands as a third parameter that we keep fixed in each of the figures (on top of each panel, $0 \leq \theta_{\rm o} \leq 90^{\rm o}$; edge-on view of the disk corresponds to $\theta_{\rm o} = 90$ deg).

The behavior of the curves is determined by the interplay of Doppler effect, strong-gravity lensing, and light aberration near the black hole. By increasing $r$ (with $a$ and $\theta_{\rm o}$ fixed) both $g_{\rm min}$ and $g_{\rm max}$ increase when $\theta_{\rm o}$ is small, showing that the dominant factor is the gravitational redshift rather than the relativistic beaming. On the other hand, the latter becomes important for large inclinations.

The method of solution is efficient enough and it allows us to explore parameters in a systematic way. On the other hand, because the parameter space is quite rich and the plots contain wealth of information, one may need to get accustomed to the actual meaning of the presented curves. Broadly speaking, the approaching side of the ring produces photons around $g_{\rm max}$ energy, whereas the receding part gives $g_{\rm min}$ for the given radius and spin. These trends are further influenced by the overall gravitational redshift, which eventually prevails as the emission radius approaches the horizon, and the light bending effect, which enhances the signal from a region of the disk around the radiation caustic at high view angles.

We remind the reader that the extremal shifts $g_{\rm min}$ and $g_{\rm max}$ play a role of observable quantities. It is convenient to have them given directly on the axis. Given $g_{\rm min}$, $g_{\rm max}$ one can immediately find the corresponding values of the emission radius and the black hole spin. The set of figs. 4.6–4.9 covers the parameter values usually considered when modeling the accreting black hole sources, i.e. the emission originating from near above the ISCO.

We also constructed the normalized plots, where $g_{\rm max}(a)$ on the ordinate is divided by its value for $a = 0.999$. These graphs are given in the right panels of figs. 4.6–4.9 for comparison with the unnormalized graph. For lower inclinations dependence on the spin is very weak.

Finally, the normalized graphs are supplemented by fig. 4.12, the right panel, that has been constructed just for the fixed value of $a = 0.999$. It allows us to read the normalization factor and to reconstruct the absolute values of the extremal shift in previous plots. We also have plotted the graphs, figs. 4.10–4.12, for other values of $a$ than $a = 0.999$ to compare the values of extremal energy shifts when the spin is fixed.

In fig. 4.13, we compare the graphs for $a = 0.10$ from fig. 4.10, $a = 0.80$ from fig. 4.11, and $a = 0.999$ from fig. 4.12 to see the difference of the behavior how $g_{\rm min}$ and $g_{\rm max}$ depend on the parameters $a$, $\theta_{\rm o}$ and $r_{\rm em}$. The transverse lines describe the energy shifts for the same emitting radii, lengthwise lines belong to the same inclination angles and the color marks the value of the spin. We could see from figs. 4.6–4.9, and fig. 4.13 also confirms, that the extremal energy shifts do not depend on the spin of a black hole between 0 and 60 deg, for higher inclination the difference is more evident. The value of $g_{\rm min}$ increases with increasing radii and will reach $g = 1$ at infinity for fixed spin and angle; $g_{\rm max}$ can increase over $g = 1$ and then decreases to one at infinity or it can only increase or decrease to $g = 1$, the behavior is more complicate and depends on the spin and view angle. The minimum of the energy shift always decreases with greater inclination, on the other side the maximum increases.

### 4.2.4 Notes on numerical calculations

Eqs. in (4.18) provide an iterative method to gain the seeked $\lambda$. However, we need to know an initial seed and calculate $\Delta q_{\rm n}^2$ and $\Delta\lambda_{\rm n}$ via eqs. (4.16) and (4.17). These eqs. (4.16) and (4.17) combine Carter's equation (4.10) and its first and second derivatives. Because the integrals in (4.10) can be expressed in the

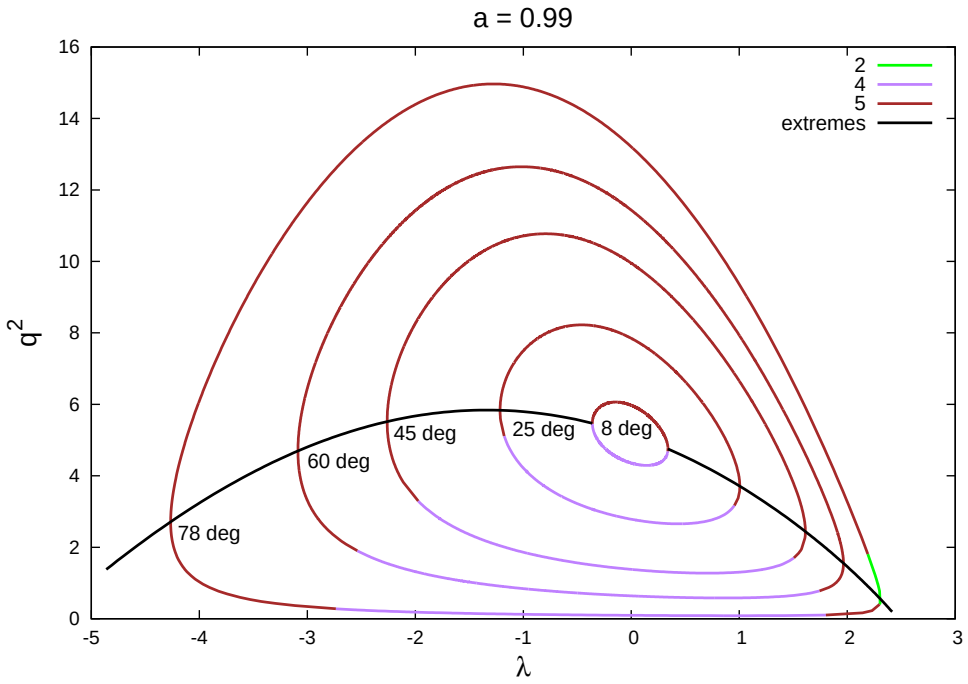


Figure 4.4: The solutions of Carter's equations for different view angles and fixed spin ($a = 0.99$) and emitting radius ($r_{\rm em} = r_{\rm ms}$). The black line represents extremal values of $\lambda$.

form of elliptical integrals, their derivatives could be easily found in the mathematical literature (Gradshteyn & Ryzhik, 1971). The derivatives are presented in Appendix B that is divided on derivatives belonging to radial and latitudinal directions. Appendix A contains the derivatives of the roots of $R\left(r, \lambda, q^2\right)$ and $\Theta\left(r, \lambda, q^2\right)$ polynomials and they are needed to quantify the derivatives in Appendix B.

The initial seed $[\lambda, q^2]$ was determined as extremal values of $\lambda$ from the case with specific black hole spin, its marginally stable orbit and $\cos\theta_{\rm o} = 0.99$ (we took approximate values near extremes from the graphs in figs. 3.2–3.5). The values of $[\lambda_{\rm min}, q_1^2]$, $[\lambda_{\rm max}, q_2^2]$ for $\cos\theta_{\rm o} = 0.99$ were then used as seeds to calculate new extremes for $\cos\theta_{\rm o} = 0.98$ with the same $a$ and $r_{\rm em}$. We continued with this process until we reached the view angle $\cos\theta_{\rm o} = 0.07$. Then we changed the emitting radius $r_{\rm em}^{\rm new} = r_{\rm em} + 0.01$, inserted the values from previous calculation with $\cos\theta_{\rm o} = 0.99$ as new seeds and repeated the procedure described above until the value $r_{\rm em} = 11$. The value of black hole was fixed. The black lines in figs. 4.4 and 4.5 represent the extremal values of $\lambda$ that were calculated via the iterative method, where we started from $\cos\theta_{\rm o} = 0.99$ ($\approx 8$ deg) to $\cos\theta_{\rm o} = 0.07$ ($\approx 86$ deg) (see fig. 4.4) and in fig. 4.5 we began from $r_{\rm em} = r_{\rm ms}$ to $r_{\rm em} = 11$.

The values were calculated via a program that was written in C/C++ and used procedures for elliptical integrals from Numerical Recipes (Press et al., 2007). The program calculated extremal values of $\lambda$ and $g(\lambda)$ for cosinus of $\theta_{\rm o}$ with step

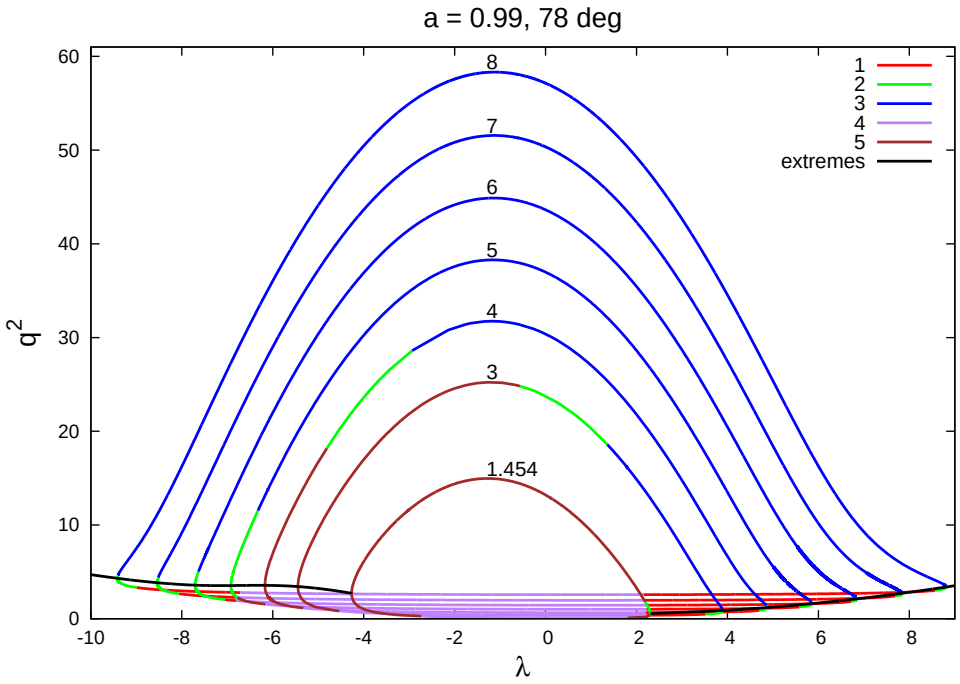


Figure 4.5: The solutions of Carter's equations for different emitting radii, fixed spin ($a = 0.99$) and view angle ($\theta_o = 78$ deg). The black line represents extremal values of $\lambda$.

0.01 from $\cos\theta_o = 0.99$ to $\cos\theta_o = 0.07$, for emitting radius, $r_{em}$, with step 0.01 from $r_{em} = r_{ms}$ to $r_{em} = 11$ and for spins $a \in (-0.99; 0.999)$ with step 0.01 (the last step was 0.009 from 0.99 to 0.999). The iterative process was repeated until the value of $g(\lambda)$ were not determined with accuracy of four decimal places. The results are plotted in contour graphs in figs. 4.6–4.12.

## 4.3 Discussion

Wings of the relativistic line become more complex when the outgoing signal is integrated over a finite range of radii. This is also the case of the aggregate line profile that has been frequently considered as originating from a radially extended zone of an accretion disk. According to the relativistic version of the standard disk model, the emissivity has a maximum near above the ISCO and it falls down towards the inner rim as well as towards infinity, however, the dissipation in a hot corona does not need to follow this law. Therefore, the line radial emissivity cannot be inferred solely from the standard disk model. Part of the information from the spectral profile is lost in the radially integrated spectrum.

It is interesting to compare our results with a similar scenario for the geometrical and kinematical properties of the reflection model by Pariev et al. (2001), who also based their discussion on the extreme frequency shifts of a spectral line, as determined by measured radiation fluxes in the iron line wings. In particular,

they show contour maps of the extremal redshift in two limiting cases – a non-rotating ($a = 0$, Schwarzschild) and the maximally co-rotating ($a = M$, Kerr) black hole. Our graphs are given while keeping the view angle $\theta_{\rm o}$ fixed, showing the expected energy of spectral-line wings as the black hole spin is varied (even to negative values).

How could the extremal shifts be used to reconstruct, at least in principle, the putative rings forming the spectral line radial emissivity profile? The main underlying assumption requires that the horns are resolved in the total observed profile. In fact, the right panel of fig. 1.7 exhibits the individual components that are summed to form the final line profile. Each of these partial constituents corresponds to one elementary ring, radius of which can be read from the $g_{\rm max}$ vs. $g_{\rm min}$ graph. In this way the observed profile can be decomposed into the components. The required time resolution of the method is of the order of orbital time at the innermost ring. We further assumed that an independent constraint on the disk inclination angle can be given. This can be based for example on the ratio of equivalent widths of the two horns. Then one will be able to read the emission radius and the black hole spin from our graphs. Or, instead of the graphical method, a fitting procedure can be employed using pre-computed tables of the energy shifts.

Naturally, this decomposition of an accretion disk into rings does not distinguish between the case of almost steady rings versus transient features that exist for a shorter period of time. The two cases should produce the same orbit-integrated profiles, so in this respect the assumption about the ring structure stands in the basis of our method. This was discussed in more detail by Czerny et al. (2004), who had developed an approximation for the mean spectra of transient flares, which they treat in terms of "belts" representing the time-averaged traces of the flares on the disk surface. This scheme produces the ring structure of the reflection spectra of the line emission fully consistent with the picture adopted in the thesis.

We note that another approach to the problem of constraining the radial emissivity of the iron line, by well-resolved time-independent spectral profiles, was discussed by Čadež et al. (2000), or by using the hot-spot scenario by Murphy et al. (2009). However, the currently available data do not allow us to achieve the high time resolution necessary to reveal the individual orbiting spots in AGNs; this would require to study time-scales of the order of $T_{\rm orb}$, which is for supermassive black holes typically $\sim 10^3$ sec and shorter. Therefore, significantly higher collecting area is needed. Alternatively one could apply this approach to accreting Galactic (stellar) black holes, which can be brighter. In fact, the relativistic iron line has been measured in several stellar black holes – e.g. the case of GRS 1915+105 microquasar (Martocchia et al., 2002b), or see the recent discussion of XTE J1550-564 microquasar (Steiner et al., 2010, and references cited therein). However, in the case of stellar-mass black holes the time-scales are expected to be shorter, as follows from the mass-scaling relation.

The above-mentioned approaches offer a potentially interesting application (though neither is useful in the context of present data). Either significantly higher

numbers of photon counts are required, or one needs to catch the accretion disk in a state when a very small number of well-separated annuli dominate the line emission, so that the two different annuli of the accretion disk can be distinguished from each other.

The results presented in this chapter are in full agreement with the `kyrline` code of Dovčiak et al. (2004b).

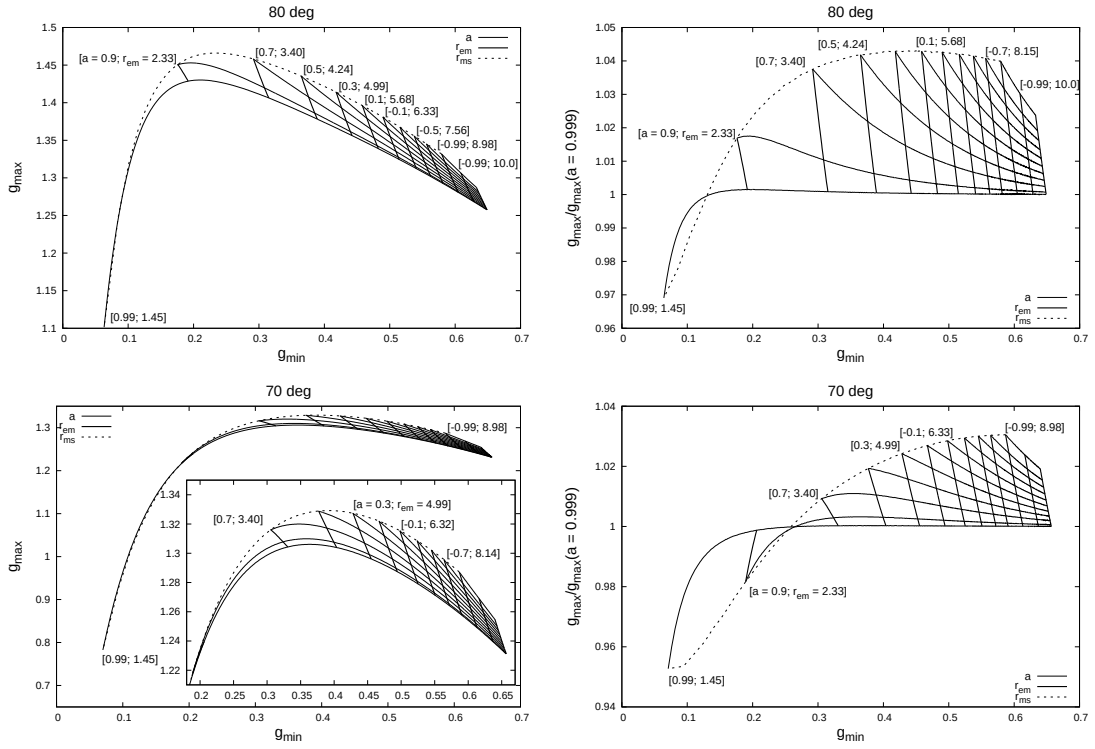


Figure 4.6: Extremal shifts of the observed photon energy for different view angles of the observer (given on top of each panel). Left panels: The magnitude of $g_{\max}$ versus $g_{\min}$. Right panels: As on the left but showing the normalized values on the ordinate (for better clarity of the plot, especially at lower inclinations). Each pair of $g_{\max}$, $g_{\min}$ values gives the corresponding emission radius $r_{\rm em}$ and the black hole spin $a$. Curves of constant $r_{\rm em}$ and the spin $a$ are distinguished by different line width (the values are written in brackets). The marginally orbit $r = r_{\rm ms}$ defines one boundary of the plot (dotted curve). By decreasing the inclination the dependency on the black hole spin becomes less prominent, and so the curves for different $a$ get closer to each other. Therefore, in the left column we show an inset where the relevant part of the plot is enlarged. See the text for details.

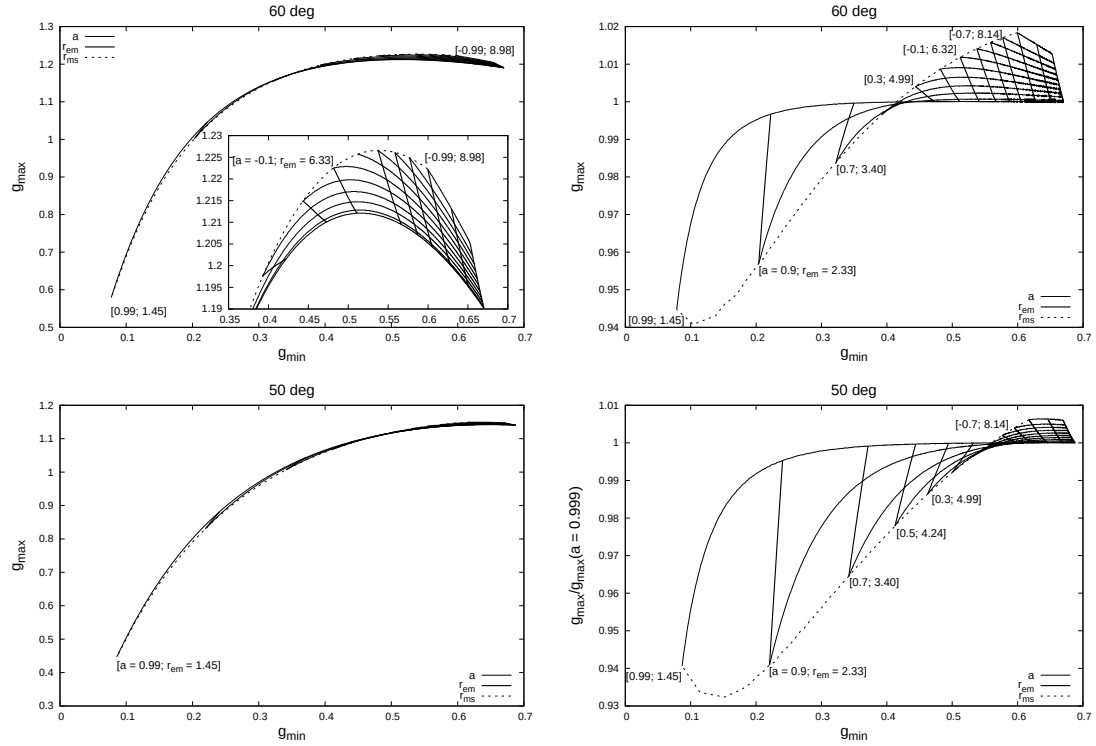


Figure 4.7: As in the previous figure, but for lower inclination angles.

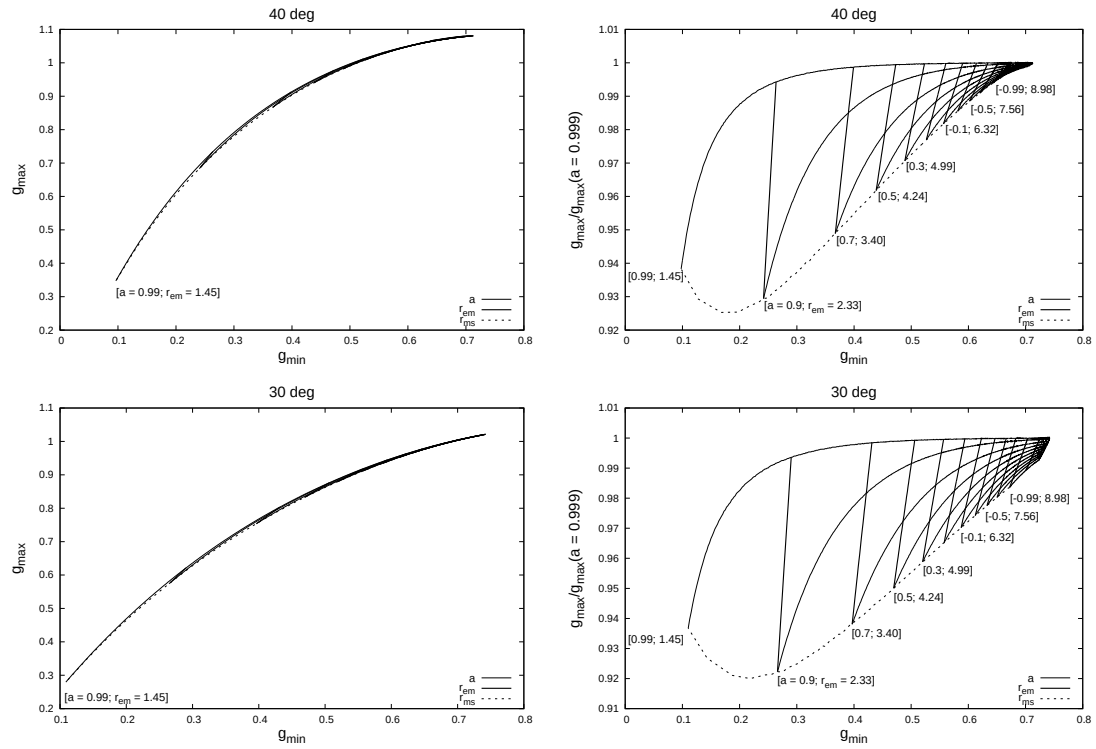


Figure 4.8: As in the previous figure, but for lower inclination angles.

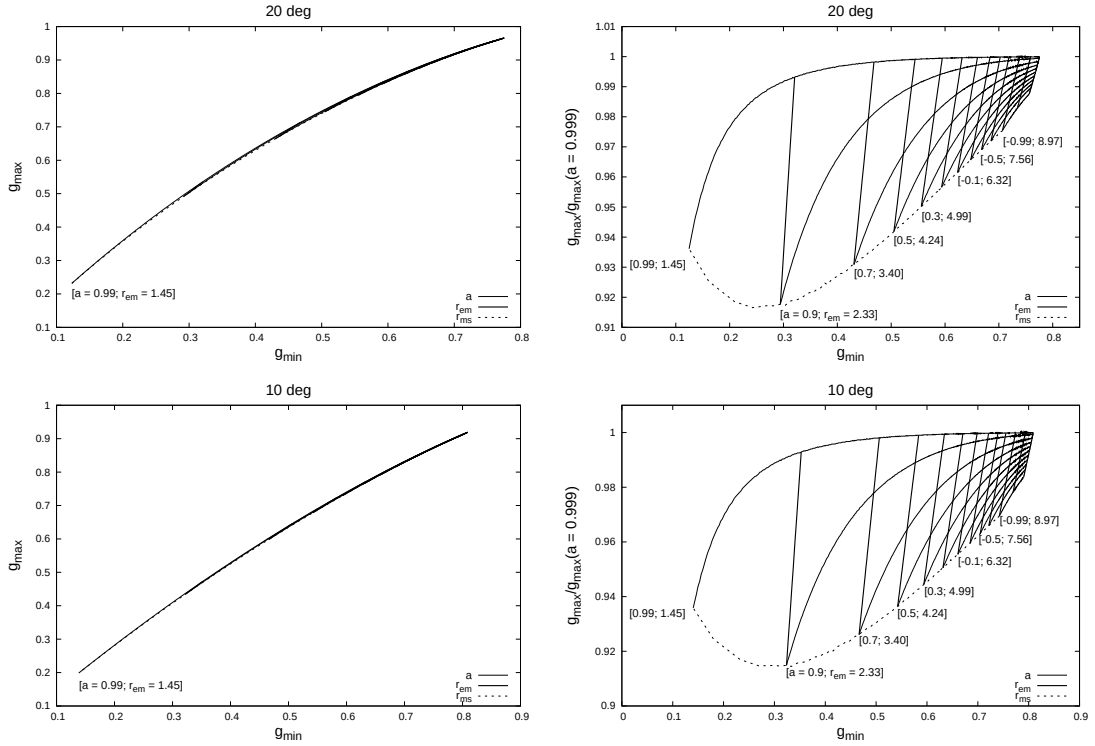


Figure 4.9: As in the previous figure, but for lower inclination angles.

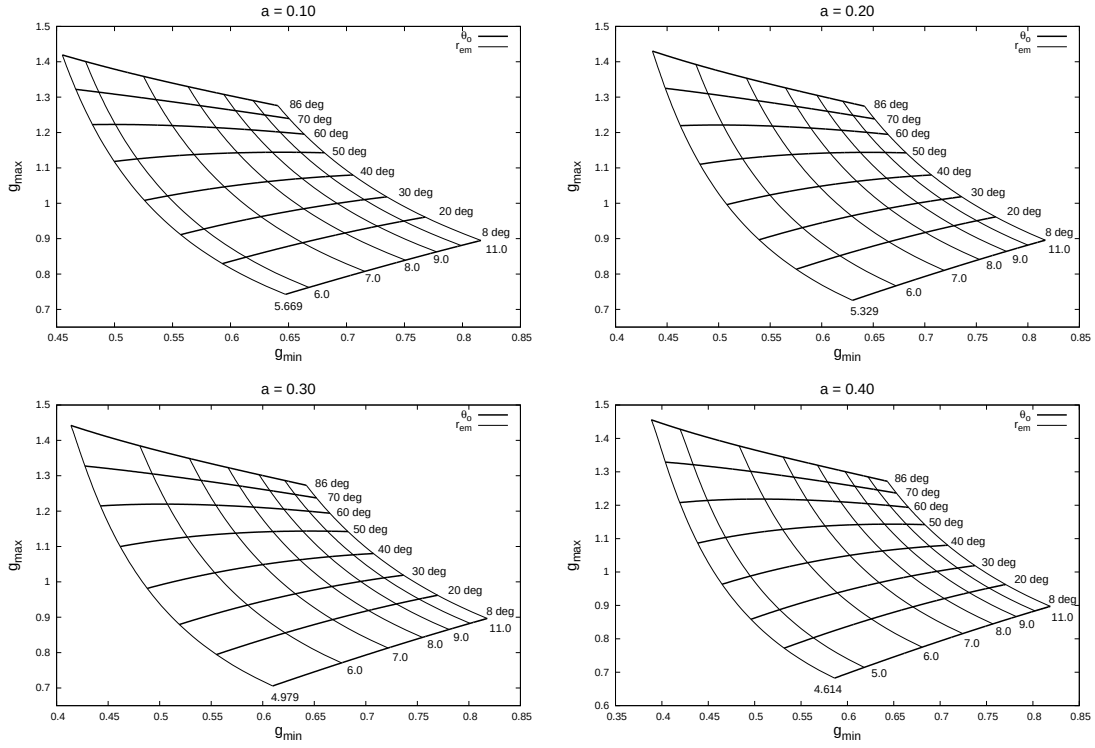


Figure 4.10: Extremal shifts for fixed $a = 0.10$, $a = 0.20$, $a = 0.30$ and $a = 0.40$.

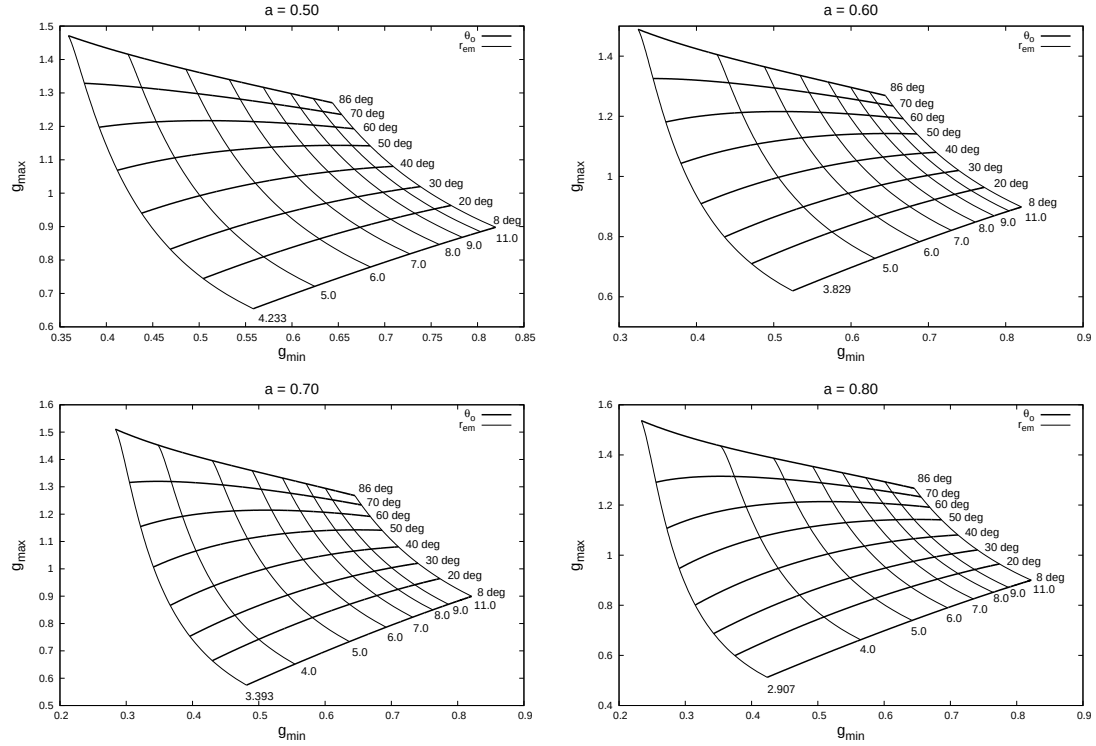


Figure 4.11: As in the previous figure, but for $a = 0.50$, $a = 0.60$, $a = 0.70$ and $a = 0.80$.

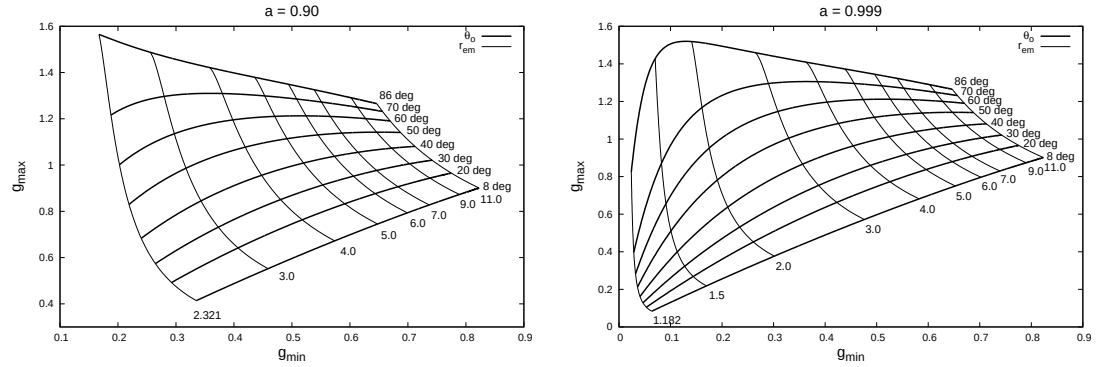


Figure 4.12: As in the previous figure, but for $a = 0.90$ and $a = 0.999$. Right plot gives the scaling factor $g_{\max}(a = 0.999)$ of the normalized graphs in figs. 4.6–4.9.

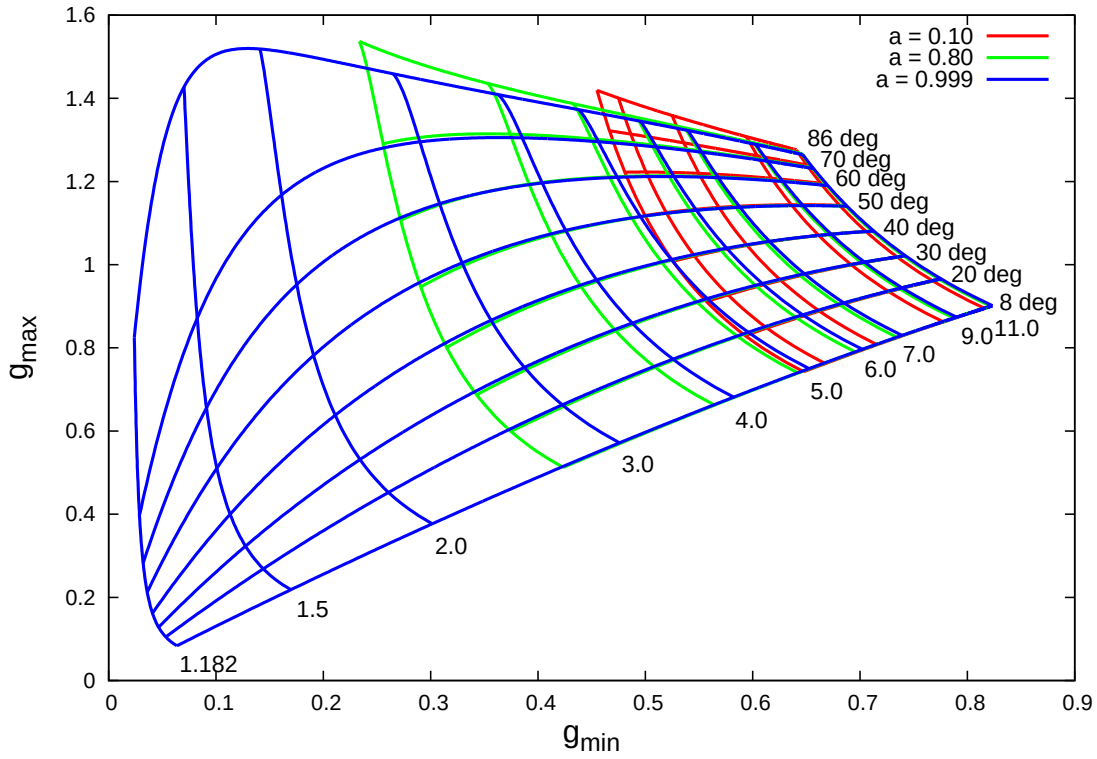


Figure 4.13: The combination of three color-coded contour graphs from figs. 4.10–4.12. The plot presents different behavior of extremal energy shifts depending on three parameters: spin, emitting radius and inclination. The overplotting of the three surfaces in the same plot allows us to compare the results for different spins. See text for more details.

# Chapter 5

# Reconstructing parameters from model spectrum

A simple prescription for the intrinsic emission of light allows us to explore the observed spectral features across the parameter space. We assume a power-law continuum (representing the primary X-rays originating from corona) plus a spectral line (representing the K$\alpha$ emission line of iron at 6.4 keV rest energy). The line is intrinsically narrow (in the local co-moving frame) of the line-producing ring, although it becomes subsequently broadened by relativistic effects. The line is produced in a range of radii over the inner disk, so the rings are just those radii where the line production is enhanced above the baseline model of the power-law component and the broad line. The mentioned components of the model spectrum give us an opportunity to test the procedure of reconstructing the source emissivity. Light rays propagate along null geodesics in the curved spacetime, which brings significant energy shifts to the final spectrum and it spreads the observed profile over the whole $\langle g_{\rm min}, g_{\rm max}\rangle$ interval with respect to the rest energy of the line.

We note that there is some unavoidable degeneracy among the model parameters. However, we will show that this degeneracy can be avoided in situations where the accretion disk emission is dominated by contributions from a small number of narrow rings located at well-defined radii. Because the gravitational redshift becomes increasingly important as the spin increases and the radius of the ring goes to $r_{\rm ms}$, the rings could be potentially revealed as features on the wing of the underlying relativistically broadened line.

In this chapter, we simulate artificial data from a bright active galactic nucleus and reconstruct parameters from the model spectrum. For this purpose we use a preliminary response matrix of LOFT (introduced in sec. 1.4).

## 5.1 Test case

The assumed source of reflection spectrum is a set of relatively narrow accretion rings or belts ($\Delta r \sim 0.5$) representing the emission excess above the standard

accretion disk spectral line around a rotating (Kerr) black hole. Thanks to the large effective area of the proposed detector (designed to reach $\simeq 10\,\mathrm{m}^2$, i.e. about two orders of magnitude greater than that of XMM-Newton near the iron line rest energy), as well as a sufficient energy resolution about 200–250 eV of LOFT mission, the accretion rings should be visible when setting realistic values of the model parameters in our test spectra. For the modeling purposes, as the worst case we assume 300 eV energy resolution.

In order to demonstrate the feasibility of the mentioned scenario we use a preliminary response matrix[1] as an example of presumed capability of a future large-collecting-area device. This will help us to assess the performance of XMM-Newton versus LOFT and our ability of constraining the model.

First, we produced the simulated spectrum by assuming the source flux of approximately 1.3 mCrab ($\simeq 3 \times 10^{-11}\,\mathrm{erg/cm^2s}$ in the energy range 2–10 keV), i.e. typical of a nearby bright Seyfert galaxy, such as MCG–6-30-15. We assumed a photo-absorbed power law continuum (photon index $\Gamma = 1.9$, hydrogen density $n_H = 4 \times 10^{21}\mathrm{cm}^{-2}$) on top of which the three rings produce a relativistically broadened spectral line (rest energy $E_{\mathrm{rest}} = 6.4$ keV).

We assumed the exposure time of 20 ks for the LOFT mission and compared the model spectrum with the same set-up for 100 ks of XMM-Newton spectrum. It is important to realize that the huge collecting area of LOFT will allow us to constrain the parameters on a significantly shorter observation time, roughly comparable with the orbital time at the corresponding radius. Therefore, the required exposure does not much exceed reasonable duration of the flares, whereas for XMM-Newton it had to be significantly longer.

The configuration of three rings is a reasonable (albeit somewhat arbitrary) trial assumption, where we can test the case of several, but not too many, radially confined excesses in the disk plane. Also the assumed duration of the observation is somewhat arbitrarily set to a value which appears to be reasonably long and realistically achievable at the same time.

We set the ring widths to be initially 0.5, i.e. comparable with the gravitational radius as a typical length-scale of the system. Other relevant model parameters were set to: $a = 0.93$ (rapidly spinning black hole in prograde rotation), $\theta_{\mathrm{o}} = 30$ deg (moderate inclination typical of a Seyfert 1 nucleus) as the initializing values. Our fiducial model is therefore `phabs*(powerlaw+4*kyrline)`, i.e. a photo-absorbed power-law continuum and four line components blurred by relativistic effects (we used XSPEC v. 12.6.0). One of the `kyrline` components originates over the entire disk surface and it has been fixed to its defaults parameters ($r_{\mathrm{ms}} \leq r \leq 400$, radial emissivity index $\alpha = 3$); it provides the main portion of the total line flux (we set about 60% for definiteness). The other components represent the emission excesses from three ring-type regions, each one giving a smaller fraction ($\simeq$10–15%) of the line flux. Naturally, diminishing the line flux produced by the rings relative to the mean flux of the entire disk and the power-law component makes the determination of $g_{\mathrm{max}}$, $g_{\mathrm{min}}$ harder and eventual-

[1] See `http://www.isdc.unige.ch/loft/` .

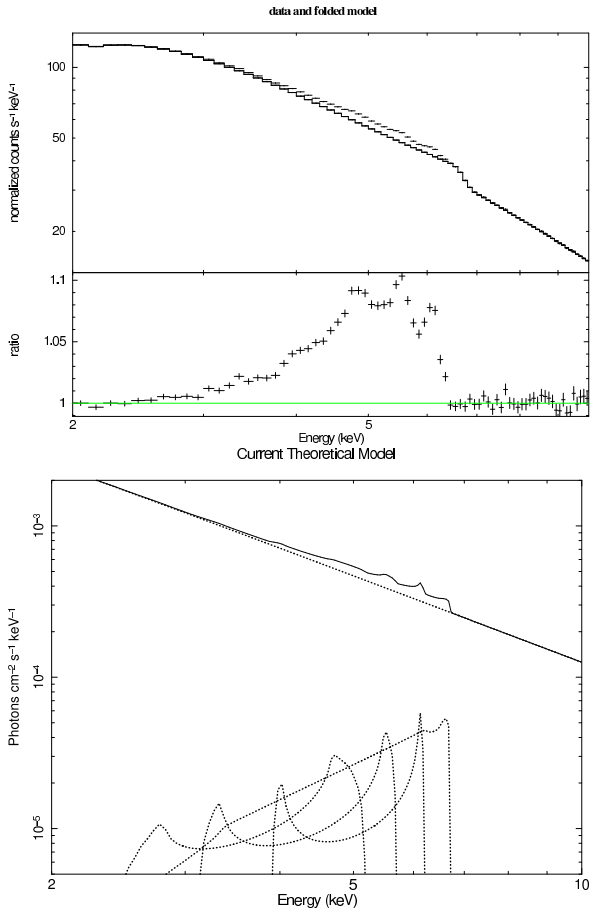


Figure 5.1: Top panel: Simulated data and the ratio to the the baseline model consisting of the power-law and the disk-line components (background subtracted). Residuals related to the three additional narrow rings are clearly visible. Bottom panel: The complete theoretical model and the model components: a power-law continuum and the individual line profiles from which the energy shifts of the components are derived.

ly impossible. We think, however, that the adopted level of the excess emissivity is realistically possible. Fig. 5.1 shows the data to model ratio for the fiducial spectrum. The geometrical location and other parameters of the model components will be now submitted to a standard rigorous fitting procedure.

One expects that a single ring would be easier to recognize in the observed spectrum, while with the growing number of rings and diminishing separation among them the total signal should resemble that of a spectral line smeared over the accretion disk. Can one estimate the model parameters directly, by locating the energy of the peaks in the spectrum?

There is a partial degeneracy of the parameter values. In our case this exhibits itself by the fact that, in order to obtain the red peaks of the line in right positions, the spin has to be greater than the lower limit of $a = 0.77$, however, the upper

| Ring | $g_{\rm min}$ | $g_{\rm max}$ | $r_{\rm in}$ | | $r_{\rm out}$ | |
|---|---|---|---|---|---|---|
| | | | $a = 0.77$ | $a = 1.00$ | $a = 0.77$ | $a = 1.00$ |
| 1 | 0.36 | 0.81 | 3.1 | 2.8 | 3.7 | 3.4 |
| 2 | 0.48 | 0.91 | 4.1 | 3.9 | 4.9 | 4.7 |
| 3 | 0.59 | 0.98 | 5.8 | 5.6 | 7.1 | 6.9 |

Table 5.1: Parameters of the model inferred from the energy positions of the spectral peaks in the test spectrum from fig. 5.1. We identified the visible features with the horns of the line components. We imposed the same inclination $\theta_{\rm o} = 30$ deg for all three rings and required the inferred spin values to be consistent with each other. The spin turns out to be constrained only partially, with the values from 0.77 up to 1.00 being consistent with the positions of peaks in the model spectrum when the radius is set appropriately. The fiducial test spectrum was generated for rings position at radii $r_{\rm in} = 3$, 4, and 6, respectively. The tabulated values demonstrate the accuracy of the fitting procedure. See the text for details.

bound remains undetermined (up to $a = 1$). For $0.77 \leq a \leq 1$, i.e. up to the maximum spin of the Kerr black hole, we can reproduce the peaks by rearranging the ring radii. This is shown in the table 5.1 by giving two possible values of $r_{\rm in}$ and $r_{\rm out}$ that are consistent simultaneously with the mention minimum and maximum values of spin. One can see that the uncertainty in the inferred radii is below 10%, while for spin the relative error represents about 25%.

Although the "visual" approach to infer the peaks of the line profile constrains the model quite well, it does not allow us to determine the errors and to perform the formal statistical confidence contours analysis, so that apparently accurate values of $g_{\rm max}$ and $g_{\rm min}$ cannot be assigned a proper meaning. The spectral fitting should result in a more reliable determination of the parameters because it employs the whole spectral shape. This appears to be important especially in the situation when the large effective area allows to resolve the broad line. On the other hand, the spectral fitting tends to be sensitive to the assumed spectral model. In order to clarify the situation we carry out the following test.

We subjected the fiducial model to the standard XSPEC fitting procedure with the aim of recovering the initial model parameters including their confidence contours. In particular, we tested if the assumed number of rings can be recovered with a significant confidence. In fig. 5.2 we show the best-fit residuals with respect to the continuum model, i.e., the plot was obtained by removing the `kyrline` component from the best-fit spectra (we show unbinned data because any definitive information about the future detector the quoted energy resolution is still preliminary at present). The number of rings was changed from the original $N = 3$ to $N = 2$ and $N = 1$. As free parameters we re-fitted the spin, $a$, view angle of an observer, $\theta_{\rm o}$, and the radial width of rings, $\Delta r$. The rest energy of the line was fixed (it was allowed to vary in subsequent tests). The position of the rings can be also allowed to change, although the procedure cannot start too far

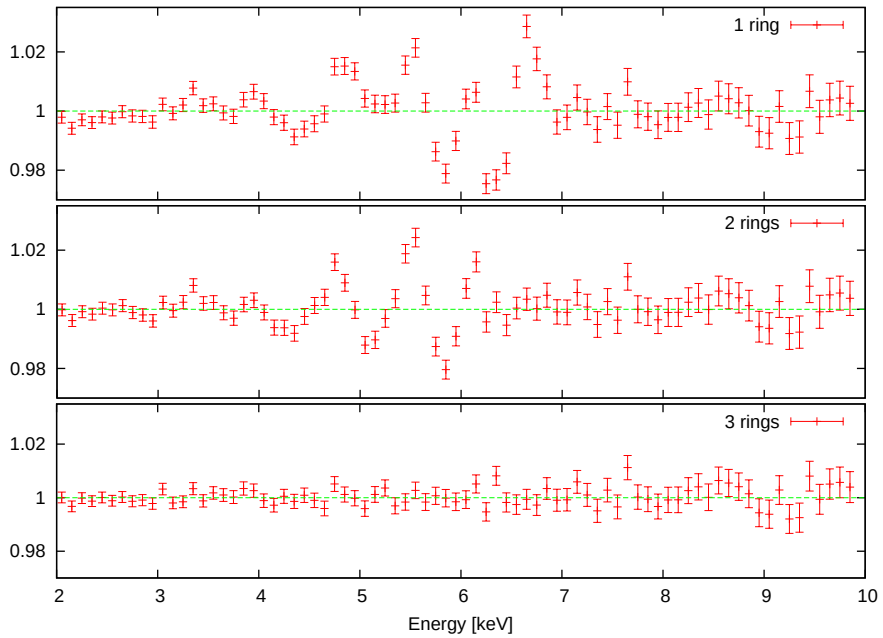


Figure 5.2: Residuals obtained by fitting the fiducial spectrum by models with a different assumption about the number $N$ of accretion rings. Clearly, $N = 1$ and $N = 2$ cases contain some unmodeled features which allow us to reject these models.

from correct values because of local minimum in the $\chi^2$ space.

By setting the number of rings to the fiducial number we recover correctly the initial values of the parameters as expected, while different numbers of rings produce worse fits and the parameters converging off the right values (or not converging at all). We examined also the case of the line emission spread over the entire disk surface (this represents the standard disk-line model), but the resulting fit was bad.

In order to compare the results expected from LOFT with those that can be reached with currently available data, we carried out the same procedure as described above also with the XMM-Newton response file of the EPIC-pn camera. Fig. 5.3 demonstrates the expected accuracy with which the model parameters are constrained. We plot the confidence contours for the inner ring radius versus the black hole spin. With the same exposure and the source brightness for both instruments, LOFT will allow us to set much tighter constraints on the best-fit values.

In fig. 5.4 we show the resulting best-fit $\chi^2_{\rm red}$ values. Decreasing the number of rings from the right value $N = 3$ obviously degrades goodness of the fit. For XMM-Newton the best-fit $\chi^2_{\rm red}$ values are lower, meaning that the model parameters are constrained at deteriorated confidence compared to LOFT. Both $N = 1$ and $N = 2$ tests give (wrongly) acceptable fits for XMM-Newton, while they can be clearly rejected with LOFT. Naturally, $N = 3$ gives a good fit because our artificial data

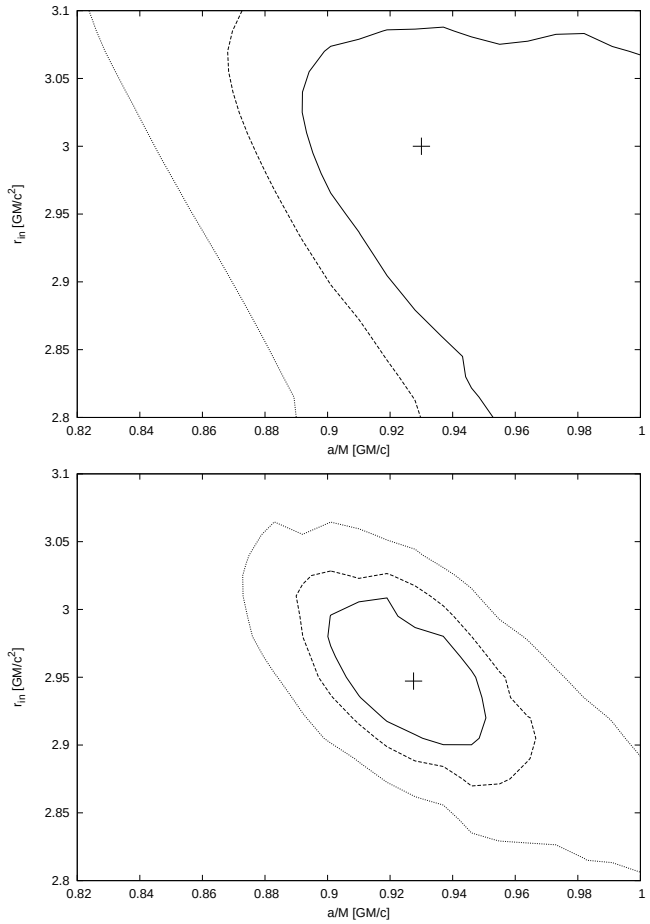


Figure 5.3: Constraints on the best-fit model parameters are derived from the simulation data. Confidence contours are shown (1, 2, and $3\sigma$) of the inner ring radius $r_{\rm in}$ vs. dimension-less spin $a$. Top panel: The best-fit case found using the XMM-Newton response matrix with 100 ksec exposure time. Bottom panel: The same analysis performed with the LOFT preliminary response matrix and 20 ksec exposure.

were created with this value, so we only reproduce the original input. Increasing the number of rings above $N = 3$ produces formally acceptable statistics, but the number of model parameters then exceeds the necessary minimum. This indicates an encouraging improvement that could be achieved for this particular problem with the improved sensitivity of LOFT.

## 5.2 Discussion

Parameter constraints could be improved also in our test case of XMM-Newton, if the observation duration can be made longer and the number of collected photons correspondingly larger. Because in practice one cannot prolong the duration above

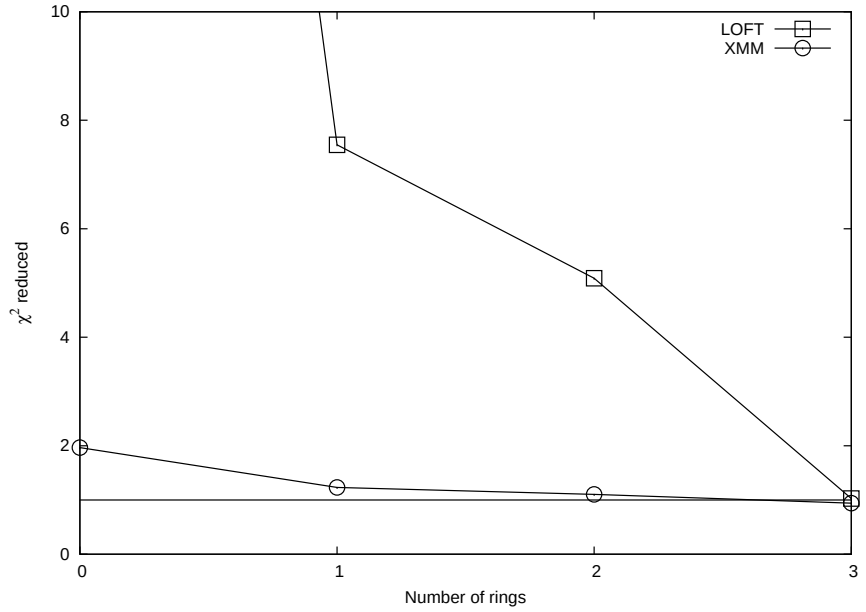


Figure 5.4: Reduced $\chi^2$ for different best fits to the fiducial model of $N = 3$ number of rings. Three cases are shown: $N = 2$ (two rings), $N = 1$ (one ring), and $N = 0$ (the line component produced only by the disk). Both $N = 1$ and $N = 2$ are statistically acceptable ($\chi^2_{\rm red} \sim 1$) with the XMM-Newton EPIC-pn response, but they can be excluded by LOFT. The following parameters were thawed for all rings during the fit procedure: $a$, $\theta_{\rm o}$, $r_{\rm in}$, $r_{\rm out}$. The following parameters were frozen: $E_{\rm rest}$, $\Gamma$, $n_H$.

some reasonable limit, the increase of the collecting area of the LOFT detector is the most important aspect which improves the parameter constraints. The energy resolution of the detector is a less critical factor because the effect of relativistic broadening causes the line width to be much broader than this limit by a significant margin.

We remark that the special choice of $N = 3$ was needed for illustration purposes described above, but it does not mean any crucial limitation that would be essential for the described idea or the method. Naturally, a lower number of rings is easier to be recognized in the spectrum and its parameters to be reconstructed correctly. On the other hand, in the case of large $N$ the magnitude of the resulting peaks above the baseline profile becomes relatively small and the situation turns into the problem discussed by Wilkins & Fabian (2011), i.e. the disk-line emission imagined as consisting of infinitesimal rings extending all the way from the inner to the outer rim of the disk.

We asked ourselves whether the energy position of the observed peaks determines the system parameters $r$, $\theta_{\rm o}$, and $a$ in any unique way, or if instead the proposed procedure of reconstructing the parameter values converges to several different results, depending on the initial guess of the parameter values. In fact, the latter is true. Therefore we need to set addition constraints in order to help

XSPEC to find the right answer. We can demonstrate this complication in another way, by plotting the observed energy difference $\delta g(r, a; \theta_o)$ of the line peaks in fig. 5.5: $\delta g \equiv g_{max} - g_{min}$. Notice that the dependence of $\delta g$ on spin is ambiguous in some parts of the parameter space.

In some situations – namely, for small radii and large spins – the energy separation of the two peaks the observed profile is not in one-to-one correspondence to model parameters; it is instead a double-valued quantity with respect to $a$ (as can be seen in the top left corner of fig. 5.5 top panel). Naturally, at large radii and small inclinations the spin dependence on $\delta g$ is weak, and so the practical use of the method becomes compromised. On the other hand, we do see the range of the parameter space (typically for radii between $r \simeq 4$ and $\simeq 12$), where the spin dependence is non-negligible and the possibility of reconstructing the parameters appears quite promising. We can also notice an interesting conspiracy when the contour-line takes almost straight vertical direction (e.g. in the same plot for $\theta_o \simeq 30$ deg, $r \simeq 5$), implying that spin is degenerate with respect to radius for that given inclination.

Also, a narrow Fe line – so ubiquitous in the X-ray spectra of type-1 AGN – will be unresolved by LOFT due to the poor energy resolution of its Large Area Detector (LAD). This could lead to confusion with the blue wing of the relativistic line if it happens to come close to the rest energy of the neutral line. However, it does not mean an insurmountable complication because these narrow features are thought to originate via scattering by a distant reflector (e.g. a torus of matter located at several thousand gravitational radii, or more). Therefore, the narrow component does not vary on short time-scales and its influence can be taken into account by estimating the flux from other, high-energy resolution spectroscopy, and including it in the model. Indeed, most of candidate objects for a relativistic line were already observed by XMM-Newton (Nandra et al., 2007; de la Calle Pérez et al., 2010), although a concurrent detection by LOFT together with another high-energy resolution mission would be the best strategy.

Naturally, the problem of confusion or non-uniqueness would appear if the broad line is produced farther out from ISCO (several tens of $r_g$ and more), so that the observed width is only moderate and comparable with the detector intrinsic energy resolution; for such cases the LOFT will not be suitable. We remark that the aforementioned simulations were performed for the response matrix resolution of 300 eV. It is currently expected that a better resolution of about 200–250 eV can be realistically achieved (Feroci et al., 2012), and so the obtained constraints should come out as even more favorable compared to the results presented here. As an example, we constructed the confidence contours of fig. 5.3, but with the energy resolution of 180 eV (an optimistic expectation), and we checked that the contour levels come out very similar to those shown for 300 eV resolution in the right panel. Both sets of best-fit values are consistent with each other.

The above-given simulations suggest that the mentioned features should be detectable around the iron line rest energy in bright accreting supermassive black holes. The foreseen energy resolution of the detector is sufficient to reveal moderately broad excesses emerging on top of the underlying continuum (unless the

resolution becomes significantly worse than the currently discussed value about 200 eV). The signal-to-noise level would be more of a concern especially if the background level were not determined with sufficient confidence. Our example demonstrates that bright AGNs (such as MCG–6-30-15 during a prominent flare of Ponti et al., 2004) should be accessible to this kind of study. To this end, the background model is required to be stable to approximately 5% accuracy.[2]

The expected signal from AGNs will be background dominated with LOFT. Therefore, for the applications discussed in this work, the precise determination of the background model is important, especially near the iron line rest energy. More detailed studies of the background impact are needed, however, currently available estimations (Feroci et al., 2012) suggest sufficient stability of the background model on the time-scales exceeding the orbital periods in the inner regions of AGN accretion disks. Promising targets can be picked up from the list by de Marco et al. (2009, and further references cited therein); these objects have already exhibited the presence of transient narrow-line features that could be relevant for our study.

Naturally, Galactic black holes in X-ray binaries represent another category of potential targets, assuming one can identify a suitable source with the flare-induced reflection signatures, similar to those seen in AGNs. According to the current specifications, the temporal resolution does not pose serious limitations (thanks to the large collecting area and sufficiently fast response time), even though the characteristic time-scale decreases proportionally to the mass, i.e., by 6–7 orders of magnitude shorter for Galactic black holes compared to supermassive black holes. On the other hand, high ionization levels are typical of Galactic black holes, and these may prevent successful detections despite the favorable source brightness that exceeds typical AGNs.

The adopted scenario has clearly an interesting potential to discriminate between the reflection model of spectral features from the case when the obscuration by intervening material and the resulting absorption are the main agents modulating the power-law continuum and shaping the observed spectrum.

In summary, we arrive at the conclusion that the fiducial values of the model parameters can be reconstructed with the anticipated capabilities of LOFT. Although in this work we considered the spectral features formed by azimuth-integrated rings, our preferred scenario of forming these rings is by orbital motion of spatially localized flares. We note that the LOFT mission is dedicated primarily to timing studies. Indeed, it should provide us with light curves of flares to much better time resolution than any of its predecessors. Temporal profiles of the flare onset and the subsequent decay exhibit some signatures of model parameters (see fig. 7 in Goosmann et al., 2007), but these are beyond current observational capabilities. Once resolved, they will give us a complementary information that can be compared against spectral studies discussed in the thesis.

[2]We tested the expected impact of background contamination by applying `corrnorm` to the background file in XSPEC. Randomizing the background at 3, 5, and 10% levels, respectively, we checked that the parameters of our fiducial model are well-reproduced in the first two cases, while the 10% inaccuracy of the background would seriously degrade the best fit constraints.

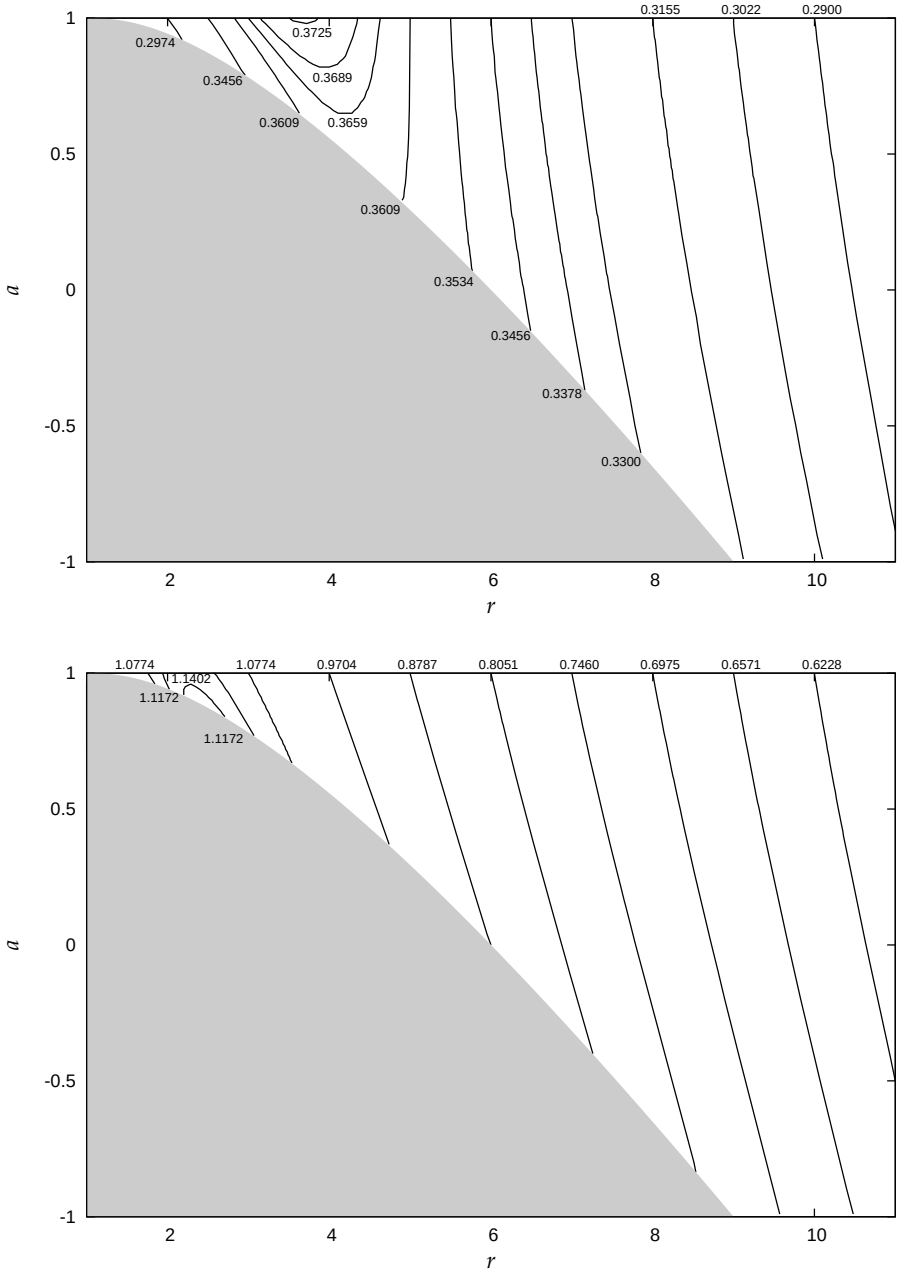


Figure 5.5: Contours of the energy difference $\delta g(r, a; \theta_o)$ of the Doppler peaks of the observed spectral line profile, as a function of the dimension-less radius $r$ of the ring and the spin $a$ of the black hole. $\delta g(r, a; \theta_o)$ defines the factor of relativistic broadening of the line. Top panel: view angle $\theta_o = 30$ deg; bottom panel: $\theta_o = 75$ deg. Although the role of spin generally increases as the distance gets smaller, we notice that $\delta g(r, a; \theta_o)$ becomes insensitive to $a$ at a certain distance. The shaded area represents the region below ISCO.

# Chapter 6

# Conclusion

In this thesis, we studied the emission line profiles and the spectral features that are specific for accretion rings in strong gravity. We examined the possibility of reconstructing the radial emissivity profile of an inner accretion disk near a rotating black hole. We considered both prograde and retrograde sense of rotation.

In chap. 3, we discussed a mathematical solution of Carter's equations and its graphical representation in figs. 3.2–3.5. We considered photons rays going directly to an observer at infinity and not crossing the equatorial plane. Photons can reach an observer on four different geodesics (fig. 3.1). In our case, only three of them appeared: without turning points; with turning point in latitudinal direction; and with turning points in both, radial and latitudinal, directions. The geodesic with turning point only in radial direction does not suit any case. The reason could be in the selection of photons because we chose view angles in range $\approx 8 - 86$ deg and did not study extreme cases when photons move only in equatorial plane ($\theta_{\rm o} = 90$ deg) or along rotating axis of a black hole ($\theta_{\rm o} = 0$ deg) due to small probability of observation of these cases. It is also interesting that photons with minimal and maximal value of $\lambda$ (corresponding to $g_{\rm min}$ and $g_{\rm max}$) always move on geodesics with turning point in the latitudinal direction.

Calculation of the extremal energy shifts in chap. 4 and their graphical representation in figs 4.6–4.12 are among the main results of the thesis. There is presented the whole process to achieve the extremal values for which we need to know the derivatives of elliptical integrals that can be found in Appendix of the thesis.

The principal assumption of the proposed application is about discrete rings forming the line emission. Knowing the extremal shifts can be useful also in another context, namely, the narrow (emission) lines produced by orbiting transient flares and spots on the accretion disk surface (Dovčiak et al., 2004a; de Marco et al., 2009). Given the intrinsic emission energy, the extremal energy shifts define the range where these spectral features can appear in the observed spectrum.

We examined theoretical profiles of the relativistic spectral line emerging from a set of concentric narrow rings which, as a whole, form a radially extended zone of an inner accretion disk. In particular we developed a systematic approach to determine the maximum and minimum energy shifts of the observed line as a func-

tion of the model parameters. As a motivation for our study we have mentioned non-monotonic radial profiles of emissivity that are consistent with intermittent episodes of accretion, and models of magnetized plasma rings with radially periodic structure.

We constrained our calculations to photons arriving along direct light rays, i.e., we ignored the higher-order images that could arise by rays making several revolutions around the black hole. This constraint is well-substantiated: firstly because the flux in these indirect images decreases exponentially with the image order ($n = 2, 3, \ldots$), and secondly these images are anyway blocked by the accretion disk.

We also neglected some other complications, such as the role of obscuration, the impact of geometrically thick (non-planar) shape of the accretion disk, or its warping. We expect that for example the role of source covering by intervening clouds along the line of sight (Karas et al., 2000) will not affect the results although it could make the proposed method more difficult by enhancing the fluctuations of the observed signal. In case of AGN, the role of accretion disk self-gravity can be important as it can significantly affects the vertical height of the outer regions of the disk (Karas et al., 2004). These effects should be considered in a future work.

We explored a possibility of studying relatively indistinct excesses on top of the relativistically broadened spectral line profile. Unlike the main body of the broad line, thought to originate from a whole extended region of the accretion disk, we modeled these features as the emission-line components arising in well-confined radial distance in the accretion disk. We also suggested that some energetically narrow features could be explained as a signature of spatially localized irradiation by magnetic reconnection flares above the underlying accretion disk. Because of prevailing rotational motion of the accreted material and unavoidably prolonged duration of observations necessary to collect enough photons, even such localized events should reveal themselves in the observed spectrum as emission rings.

We discussed in chap. 4 that available data from present X-ray missions do not allow us to reveal such debated structures in spectra. Therefore, we produced a model spectrum (chap. 5) and reconstructed parameters from it with preliminary response matrix for LOFT.

We found that the presence of about 10–15% excess emission of the line flux originating from a ring of a moderate width (typically a fraction of gravitational radius) close to the black hole could be tested by the proposed LOFT satellite. The effective area of this mission is designed to be large enough to allow the model parameters to be constrained despite its limited energy resolution. This will significantly reduce the degeneracy of the model parameters – a notorious obstacle complicating interpretations of the current data. One needs to note that the ability of converging to the correct parameter values could be compromised if the background level is significantly increased above our default estimation, so this issue will need further investigation. In fact, bright Galactic stellar-mass black-hole candidates may be more suitable sources, as AGN will be always dominated by the background.

In the thesis we concentrated ourselves to the supermassive black hole especially because in this case the base-line model can be assumed in a relatively simple form and the iron-line complex has been commonly detected in AGN, nevertheless, bright Galactic binaries with accurately modeled spectral components may be eventually a more suitable category of targets. At this stage we could only verify that the anticipated background level does not pose a serious limitation for the example described above, assuming that the background model is itself known with the sufficient accuracy. This issue will need further investigation especially because the background level is expected to vary with energy, and so, in principle, inaccuracy of the background model could arise.

A typical double-horn profile gives us an opportunity to determine the parameters by measuring the energy shifts of the features within the broad spectral line wings. The observed energy of these features is well-defined (assuming a sufficiently narrow radial extent of the rings). Naturally, the inferred parameters from different rings should be consistent with each other (e.g. the same spin of the black hole and the same inclination of different rings, assuming that the rings reside in the equatorial plane). This will help us to distinguish the disk–line geometry of the line emitting region from alternative options, such as the lines originating in outflows and jets (Wang et al., 2000), spiral waves (Hartnoll & Blackmann, 2002), or geometrically thick non-Keplerian tori (Fuerst & Wu, 2007).

Even in situations when the contribution of rings is only moderate and the energy shifts cannot be determined immediately from the secondary peaks merely by inspecting the spectrum, the fitting procedure can be employed to reconstruct the model parameters. This requires employing a physically substantiated model of the spectrum and using the entire profile of the broad line and the continuum. Naturally, in the latter case the assumptions about the intrinsic spectrum are essential.

The concept seems to be well suited to study the effects which are often coined as “strong gravity” in the astrophysical context. Despite a limited energy resolution and various convergence issues of the spectral fitting procedure discussed in chap. 5, the large effective area offers a significant progress over what can be presently achieved with XMM-Newton not only in the case of timing studies but also for the spectroscopy of truly broad relativistic spectral features.

# Chapter 7

# Future perspective

In future, we would like to study a transient accretion disk formed after a tidal disruption of a star passing too close to a supermassive black hole (SMBH). This idea was occurred in early works (Hills, 1975; Young et al., 1977), where the authors assumed that active galactic nuclei are fueled by accreting debris from such tidal disruption events (TDEs) and as an explanation of a bright flares in quiescent galaxies (Rees, 1988).

TDEs are observed in the optical, UV, and X-rays. Several candidates were discovered in the UV by the Galaxy Evolution Explorer (GALEX) with their optical counterparts, found by the Canada-France-Hawaii Telescope legacy Survey and Panoramic Survey Telescope and Rapid Response System (Pan-STARRS) Medium Deep Survey (Gezari et al., 2006, 2008, 2012). The Roentgen satellite (ROSAT) observed a flare in soft X-rays in NGC 5905, a galaxy with no previous indication of a nuclear activity (Bade et al., 1996). Another TDE candidates in X-rays were discovered by the XMM-Newton Slew Survey (Esquej et al., 2007). TDEs in hard X-rays are observed if they launch jets pointed towards us. The events Sw J1644+57 (Burrows et al., 2011; Levan et al., 2011; Bloom et al., 2011) and Sw J2058+05 (Cenko et al., 2012) discovered by the Burst Alert Telescope on the Swift satellite are assumed to be such relativistic tidal disruption flares.

The upper limit for the mass of the black hole for a disrupted main sequence star with mass $\sim 1\ M_\odot$ and a non-spinning black hole is $M_{\rm bh} \lesssim 10^7\ M_\odot$, and for a rapidly spinning black hole, $M_{\rm bh} \lesssim 10^8\ M_\odot$ (Rees, 1988). Main sequence stars are the best candidates for the disruption close enough to a black hole .

At first we can assume a ring formed from the debris of a tidally disrupted star in the equatorial plane. The ring is gradually circularized and spreading due the viscous processes and a transient disk forms. It is important to investigate the parameters of such a disk (e. g. viscosity parameter, thickness, type of the disk, temperature etc.) and how they change the evolution. Then we could determine the time scale when matter reaches the marginally stable orbit.

After that we will examine the flares in hard X-rays. What could be the theoretical models of iron lines and how they evolve in time. One of the results will be simulated spectra. The study of TDEs in hard X-rays is a new opportunity to understand physical processes ongoing around black holes.

# Appendix A

# Derivatives of roots, $r_1$, $r_2$, $r_3$, $r_4$, from $R(r;\lambda,q^2)$, and $\mu_1$, $\mu_2$ from $\Theta(\mu;\lambda,q^2)$ polynomials with respect to $\lambda$ and $q^2$

In this appendix, we give useful explicit expressions for derivatives of roots defined in eqs. (2.60) and (2.69) that are needed to express of derivatives of elliptical integrals in Appendix B.

The upper indexes $f^{\lambda}$, $f^{q^2}$ represent the partial derivatives with respect to $\lambda$ or $q^2$: $f^{\lambda} \equiv \frac{\partial f}{\partial \lambda}$, $f^{q^2} \equiv \frac{\partial f}{\partial q^2}$, $f^{q^2\lambda} \equiv \frac{\partial^2 f}{\partial q^2 \partial \lambda}$, $f^{q^2q^2} \equiv \frac{\partial^2 f}{\partial q^2 \partial q^2}$. The notation $f'$ and $f''$ signifies the general derivatives that are identical for $\lambda$ and $q^2$.

Before we write first and second derivatives of the roots, eqs. (2.60) and (2.69), we denote the derivatives of auxilliary expressions, eqs. (2.61)–(2.68):

$$A^{\lambda} = -2\lambda, \tag{A.1}$$
$$A^{q^2} = -1, \tag{A.2}$$
$$A^{q^2\lambda} = 0, \tag{A.3}$$
$$A^{q^2q^2} = 0, \tag{A.4}$$

$$B^{\lambda} = -2(a-\lambda), \tag{A.5}$$
$$B^{q^2} = 1, \tag{A.6}$$
$$B^{q^2\lambda} = 0, \tag{A.7}$$
$$B^{q^2q^2} = 0, \tag{A.8}$$

$$C^{\lambda} = -4A\lambda, \tag{A.9}$$
$$C^{q^2} = -2A - 12a^2, \tag{A.10}$$
$$C^{q^2\lambda} = 4\lambda, \tag{A.11}$$
$$C^{q^2q^2} = 2, \tag{A.12}$$

$$D^{\lambda} = -12A^2\lambda - 144a^2q^2\lambda - 432B(a-\lambda), \tag{A.13}$$
$$D^{q^2} = -6A^2 + 72a^2A - 72a^2q^2 + 216B, \tag{A.14}$$
$$D^{q^2\lambda} = 24A\lambda - 144a^2\lambda - 432(a-\lambda), \tag{A.15}$$
$$D^{q^2q^2} = 12A - 144a^2 + 216. \tag{A.16}$$

For $-4C^3 + D^2 > 0$:

$$Z' = \frac{-6C^2C' + DD'}{Z}, \tag{A.17}$$
$$Z^{q^2\lambda} = \frac{-12CC^{q^2}C^{\lambda} - 6C^2C^{q^2\lambda} + D^{q^2}D^{\lambda} + DD^{q^2\lambda} - Z^{q^2}Z^{\lambda}}{Z}, \tag{A.18}$$
$$Z'' = \frac{-12C(C')^2 - 6C^2C'' + (D')^2 + DD'' - (Z')^2}{Z}, \tag{A.19}$$

$$E' = \frac{1}{9\sqrt[3]{2}}\left[\frac{D'-Z'}{(D-Z)^{2/3}} + \frac{D'+Z'}{(D+Z)^{2/3}}\right], \tag{A.20}$$
$$E^{q^2\lambda} = \frac{1}{9\sqrt[3]{2}}\left[\frac{D^{q^2\lambda}-Z^{q^2\lambda}}{(D-Z)^{2/3}} + \frac{D^{q^2\lambda}+Z^{q^2\lambda}}{(D+Z)^{2/3}}\right. \tag{A.21}$$
$$\left. - \frac{2}{3}\frac{(D^{q^2}-Z^{q^2})(D^{\lambda}-Z^{\lambda})}{(D-Z)^{5/3}} - \frac{2}{3}\frac{(D^{q^2}+Z^{q^2})(D^{\lambda}+Z^{\lambda})}{(D+Z)^{5/3}}\right],$$
$$E'' = \frac{1}{9\sqrt[3]{2}}\left[\frac{D''-Z''}{(D-Z)^{2/3}} + \frac{D''+Z''}{(D+Z)^{2/3}} - \frac{2}{3}\frac{(D'-Z')^2}{(D-Z)^{5/3}}\right. \tag{A.22}$$
$$\left. - \frac{2}{3}\frac{(D'+Z')^2}{(D+Z)^{5/3}}\right];$$

for $-4C^3 + D^2 < 0$:

$$Z' = \frac{6C^2C' - DD'}{Z}, \tag{A.23}$$
$$Z^{q^2\lambda} = \frac{12CC^{q^2}C^{\lambda} + 6C^2C^{q^2\lambda} - D^{q^2}D^{\lambda} - DD^{q^2\lambda}}{Z} - \frac{Z^{q^2}Z^{\lambda}}{Z}, \tag{A.24}$$
$$Z'' = \frac{12C(C')^2 + 6C^2C'' - (D')^2 - DD''}{Z} - \frac{(Z')^2}{Z}, \tag{A.25}$$

$$
\begin{aligned}
E' &= \frac{2}{9\sqrt[3]{2}(D^2+Z^2)^{5/6}}\left[(DD'+ZZ')\cos\varphi_a\right. && \text{(A.26)}\\
&\left.+\,(D'Z-DZ')\sin\varphi_a\right],\\
E^{q^2\lambda} &= -\frac{5}{3}\frac{(DD^\lambda+ZZ^\lambda)E^{q^2}}{D^2+Z^2} && \text{(A.27)}\\
&+\frac{2}{9\sqrt[3]{2}(D^2+Z^2)^{5/6}}\left[\left(D^{q^2}D^\lambda+DD^{q^2\lambda}+Z^{q^2}Z^\lambda+ZZ^{q^2\lambda}\right)\cos\varphi_a\right.\\
&+\left(D^{q^2\lambda}Z+D^{q^2}Z^\lambda-D^\lambda Z^{q^2}-DZ^{q^2\lambda}\right)\sin\varphi_a\\
&+\frac{(DD^{q^2}+ZZ^{q^2})(D^\lambda Z-DZ^\lambda)}{3(D^2+Z^2)}\sin\varphi_a\\
&\left.-\frac{(D^{q^2}Z-DZ^{q^2})(D^\lambda Z-DZ^\lambda)}{3(D^2+Z^2)}\cos\varphi_a\right],\\
E'' &= -\frac{5}{3}\frac{(DD'+ZZ')E'}{D^2+Z^2} && \text{(A.28)}\\
&+\frac{2}{9\sqrt[3]{2}(D^2+Z^2)^{5/6}}\left\{\left[(D')^2+DD''+(Z')^2+ZZ''\right]\cos\varphi_a\right.\\
&+(D''Z-DZ'')\sin\varphi_a+\frac{(DD'+ZZ')(D'Z-DZ')}{3(D^2+Z^2)}\sin\varphi_a\\
&\left.-\frac{(D'Z-DZ')^2}{3(D^2+Z^2)}\cos\varphi_a\right\};
\end{aligned}
$$

$$F' = \frac{-\frac{2}{3}A'+E'}{2F}, \qquad \text{(A.29)}$$

$$F^{q^2\lambda} = \frac{-\frac{2}{3}A^{q^2\lambda}+E^{q^2\lambda}-2F^{q^2}F^\lambda}{2F}, \qquad \text{(A.30)}$$

$$F'' = \frac{-\frac{2}{3}A''+E''-2(F')^2}{2F}, \qquad \text{(A.31)}$$

$$G^\lambda = 2\lambda, \qquad \text{(A.32)}$$

$$G^{q^2} = 1, \qquad \text{(A.33)}$$

$$G^{q^2\lambda} = 0, \qquad \text{(A.34)}$$

$$G^{q^2q^2} = 0, \qquad \text{(A.35)}$$

$$
\begin{aligned}
D'_\pm &= -\frac{4}{3}A' - E' \pm \frac{4B'F-4BF'}{F^2}, && \text{(A.36)}\\
D^{q^2\lambda}_\pm &= -\frac{4}{3}A^{q^2\lambda} - E^{q^2\lambda} \pm 4\frac{B^{q^2\lambda}F+B^{q^2}F^\lambda-B^\lambda F^{q^2}-BF^{q^2\lambda}}{F^2} && \text{(A.37)}\\
&\mp 8\frac{B^{q^2}F-BF^{q^2}}{F^3}F^\lambda,\\
D''_\pm &= -\frac{4}{3}A'' - E'' \pm \frac{4B''F-4BF''}{F^2} \mp 2\frac{4B'F-4BF'}{F^3}F'. && \text{(A.38)}
\end{aligned}
$$

## A.1 $R(r, \lambda, q^2)$ polynomial

The derivatives of the roots, eqs. in (2.60), are

$$r_1' = \frac{1}{2}F' + \frac{1}{4}\frac{D_-'}{(D_-)^{1/2}}, \tag{A.39}$$

$$r_1^{q^2\lambda} = \frac{1}{2}F^{q^2\lambda} + \frac{1}{4}\frac{D_-^{q^2\lambda}}{(D_-)^{1/2}} - \frac{1}{8}\frac{D_-^{q^2}D_-^{\lambda}}{(D_-)^{3/2}}, \tag{A.40}$$

$$r_1'' = \frac{1}{2}F'' + \frac{1}{4}\frac{D_-''}{(D_-)^{1/2}} - \frac{1}{8}\frac{(D_-')^2}{(D_-)^{3/2}}, \tag{A.41}$$

$$r_2' = \frac{1}{2}F' - \frac{1}{4}\frac{D_-'}{(D_-)^{1/2}}, \tag{A.42}$$

$$r_2^{q^2\lambda} = \frac{1}{2}F^{q^2\lambda} - \frac{1}{4}\frac{D_-^{q^2\lambda}}{(D_-)^{1/2}} + \frac{1}{8}\frac{D_-^{q^2}D_-^{\lambda}}{(D_-)^{3/2}}, \tag{A.43}$$

$$r_2'' = \frac{1}{2}F'' - \frac{1}{4}\frac{D_-''}{(D_-)^{1/2}} + \frac{1}{8}\frac{(D_-')^2}{(D_-)^{3/2}}, \tag{A.44}$$

$$r_3' = -\frac{1}{2}F' + \frac{1}{4}\frac{D_+'}{(D_+)^{1/2}}, \tag{A.45}$$

$$r_3^{q^2\lambda} = -\frac{1}{2}F^{q^2\lambda} + \frac{1}{4}\frac{D_+^{q^2\lambda}}{(D_+)^{1/2}} - \frac{1}{8}\frac{D_+^{q^2}D_+^{\lambda}}{(D_+)^{3/2}}, \tag{A.46}$$

$$r_3'' = -\frac{1}{2}F'' + \frac{1}{4}\frac{D_+''}{(D_+)^{1/2}} - \frac{1}{8}\frac{(D_+')^2}{(D_+)^{3/2}}, \tag{A.47}$$

$$r_4' = -\frac{1}{2}F' - \frac{1}{4}\frac{D_+'}{(D_+)^{1/2}}, \tag{A.48}$$

$$r_4^{q^2\lambda} = -\frac{1}{2}F^{q^2\lambda} - \frac{1}{4}\frac{D_+^{q^2\lambda}}{(D_+)^{1/2}} - \frac{1}{8}\frac{D_+^{q^2}D_+^{\lambda}}{(D_+)^{3/2}}, \tag{A.49}$$

$$r_4'' = -\frac{1}{2}F'' - \frac{1}{4}\frac{D_+''}{(D_+)^{1/2}} + \frac{1}{8}\frac{(D_+')^2}{(D_+)^{3/2}}. \tag{A.50}$$

## A.2 $\Theta(\mu, \lambda, q^2)$ polynomial

The derivatives of the roots, eqs. in (2.69), are

$$\mu_{\pm}^{\lambda} = \frac{1}{4a^2\mu_{\pm}}\left[\frac{GG^{\lambda}}{(G^2+4a^2q^2)^{1/2}} \mp G^{\lambda}\right], \tag{A.51}$$

$$\mu_{\pm}^{q^2} = \frac{1}{4a^2\mu_{\pm}}\left[\frac{GG^{q^2}+2a^2}{(G^2+4a^2q^2)^{1/2}} \mp G^{q^2}\right], \tag{A.52}$$

$$\begin{aligned}\mu_{\pm}^{\lambda q^2} &= -\frac{\mu_{\pm}^{q^2}\mu_{\pm}^{\lambda}}{\mu_{\pm}} \\ &\quad + \frac{1}{4a^2\mu_{\pm}}\left[\frac{G^{q^2}G^{\lambda}+GG^{\lambda q^2}}{(G^2+4a^2q^2)^{1/2}} - \frac{GG^{\lambda}(GG^{q^2}+2a^2)}{(G^2+4a^2q^2)^{3/2}} \mp G^{\lambda q^2}\right]\end{aligned} \tag{A.53}$$

$$\begin{aligned}\mu_{\pm}^{q^2q^2} &= -\frac{\left(\mu_{\pm}^{q^2}\right)^2}{\mu_{\pm}} \\ &\quad + \frac{1}{4a^2\mu_{\pm}}\left[\frac{G^{q^2}G^{q^2}+GG^{q^2q^2}}{(G^2+4a^2q^2)^{1/2}} - \frac{(GG^{q^2}+2a^2)^2}{(G^2+4a^2q^2)^{3/2}} \mp G^{q^2q^2}\right].\end{aligned} \tag{A.54}$$

# Appendix B

# Derivatives of elliptical integrals for determination of extremal energy shifts

We define an elliptical integral of the first kind as

$$F(\varphi,k)=\int\limits_0^{\varphi}\frac{\mathrm{d}\vartheta}{\sqrt{1-k\sin^2\vartheta}}, \tag{B.1}$$

and its derivative

$$\begin{aligned}F'(\varphi,k) &= \left[-\frac{F(\varphi,k)}{2k}-\frac{E(\varphi,k)}{2k(k-1)}+\frac{\sin 2\varphi}{4(k-1)\left(1-k\sin^2\varphi\right)^{1/2}}\right]k' \\ &+\frac{\varphi'}{\left(1-k\sin^2\varphi\right)^{1/2}}.\end{aligned} \tag{B.2}$$

A complete elliptical integral of the first kind is defined as

$$F\left(\frac{\pi}{2},k\right)=K(k)=\int\limits_0^{\frac{\pi}{2}}\frac{\mathrm{d}\vartheta}{\sqrt{1-k\sin^2\vartheta}}, \tag{B.3}$$

and its derivative

$$K'(k)=\frac{1}{2}\left[\frac{E(k)}{k(1-k)}-\frac{K(k)}{k}\right]k'. \tag{B.4}$$

An elliptical integral of the second kind has form

$$E(\varphi,k)=\int\limits_0^{\varphi}\sqrt{1-k\sin^2\vartheta}\mathrm{d}\vartheta, \tag{B.5}$$

and its derivative is

$$E'(\varphi,k)=\frac{1}{2}\left[E(\varphi,k)-F(\varphi,k)\right]\frac{k'}{k}+\varphi'\left(1-k\sin^2\varphi\right)^{1/2}. \tag{B.6}$$

A complete elliptical integral of the second kind is defined as

$$E\left(\frac{\pi}{2},k\right)=E(k)=\int_0^{\frac{\pi}{2}}\sqrt{1-k\sin^2\theta}\mathrm{d}\theta, \tag{B.7}$$

and its derivative

$$E'(k)=\frac{1}{2}\left[E(k)-K(k)\right]\frac{k'}{k}. \tag{B.8}$$

The notation is different than in Abramowitz & Stegun (1965), Byrd & Friedman (1971) and Gradshteyn & Ryzhik (1971) for compliance with used procedures in the computational program. In next sections, we present derivatives of expressions defined in sections 3.1–3.3 to gain the derivatives of elliptical integrals with respect to $\lambda$ and $q^2$.

## B.1 Radial direction, four real roots

The derivatives of $g_r(\lambda,q^2)$ in eq. (3.7) are

$$g_r'=-\frac{g_r}{2}\left[\frac{(r_1'-r_3')}{(r_1-r_3)}+\frac{(r_2'-r_4')}{(r_2-r_4)}\right], \tag{B.9}$$

$$\begin{aligned} g_r^{q^2\lambda} &= \frac{g_r^{q^2}g_r^{\lambda}}{g_r}-\frac{g_r}{2}\left[\frac{(r_1^{q^2\lambda}-r_3^{q^2\lambda})}{(r_1-r_3)}+\frac{(r_2^{q^2\lambda}-r_4^{q^2\lambda})}{(r_2-r_4)}\right. \\ &\quad \left.-\frac{(r_1^{q^2}-r_3^{q^2})(r_1^{\lambda}-r_3^{\lambda})}{(r_1-r_3)^2}-\frac{(r_2^{q^2}-r_4^{q^2})(r_2^{\lambda}-r_4^{\lambda})}{(r_2-r_4)^2}\right], \end{aligned} \tag{B.10}$$

$$\begin{aligned} g_r'' &= \frac{(g_r')^2}{g_r}-\frac{1}{2}g_r\left[\frac{(r_1''-r_3'')}{(r_1-r_3)}+\frac{(r_2''-r_4'')}{(r_2-r_4)}\right. \\ &\quad \left.-\frac{(r_1'-r_3')^2}{(r_1-r_3)^2}-\frac{(r_2'-r_4')^2}{(r_2-r_4)^2}\right]. \end{aligned} \tag{B.11}$$

The derivatives of $F(\varphi_e, k_r)$ in eq. (3.11) are

$$F'(\varphi_e, k_r) = \left[-\frac{F(\varphi_e, k_r)}{2k_r} - \frac{E(\varphi_e, k_r)}{2k_r(k_r-1)} + \frac{\sin 2\varphi_e}{4(k_r-1)\left(1-\beta_2\right)^{1/2}}\right] k_r' + \frac{\varphi_e'}{\left(1-\beta_2\right)^{1/2}}, \tag{B.12}$$

$$\begin{aligned} F^{q^2\lambda}(\varphi_e, k_r) = & \left[-\frac{F(\varphi_e, k_r)}{2k_r} - \frac{E(\varphi_e, k_r)}{2k_r(k_r-1)}\right]^{\lambda} k_r^{q^2} \\ & + \left[\frac{\sin 2\varphi_e}{4(k_r-1)\left(1-\beta_2\right)^{1/2}}\right]^{\lambda} k_r^{q^2} \\ & + \left[\frac{\varphi_e^{q^2}}{\left(1-\beta_2\right)^{1/2}}\right]^{\lambda} \\ & + \left[-\frac{F(\varphi_e, k_r)}{2k_r} - \frac{E(\varphi_e, k_r)}{2k_r(k_r-1)} + \frac{\sin 2\varphi_e}{4(k_r-1)\left(1-\beta_2\right)^{1/2}}\right] k_r^{q^2\lambda}, \end{aligned} \tag{B.13}$$

$$\begin{aligned} F''(\varphi_e, k_r) = & \left[-\frac{F(\varphi_e, k_r)}{2k_r} - \frac{E(\varphi_e, k_r)}{2k_r(k_r-1)}\right]' k_r' \\ & + \left[\frac{\sin 2\varphi_e}{4(k_r-1)\left(1-\beta_2\right)^{1/2}}\right]' k_r' \\ & + \left[\frac{\varphi_e'}{\left(1-\beta_2\right)^{1/2}}\right]' \\ & + \left[-\frac{F(\varphi_e, k_r)}{2k_r} - \frac{E(\varphi_e, k_r)}{2k_r(k_r-1)} + \frac{\sin 2\varphi_e}{4(k_r-1)\left(1-\beta_2\right)^{1/2}}\right] k_r'', \end{aligned} \tag{B.14}$$

where

$$\begin{aligned} \left[-\frac{F(\varphi_e, k_r)}{2k_r} - \frac{E(\varphi_e, k_r)}{2k_r(k_r-1)}\right]' = & -\frac{F'(\varphi_e, k_r)}{2k_r} - \frac{E'(\varphi_e, k_r)}{2k_r(k_r-1)} \\ & + \left[\frac{F(\varphi_e, k_r)}{2k_r^2} + \frac{E(\varphi_e, k_r)(2k_r-1)}{2k_r^2(k_r-1)^2}\right] k_r', \end{aligned} \tag{B.15}$$

$$\begin{aligned} \left[\frac{\sin 2\varphi_e}{4(k_r-1)\left(1-\beta_2\right)^{1/2}}\right]' = & \frac{\varphi_e' \cos 2\varphi_e}{2(k_r-1)\left(1-\beta_2\right)^{1/2}} \\ & - \frac{\sin 2\varphi_e(2k_r' - 2k_r'\beta_2 - k_r\beta_2' + \beta_2')}{8(k_r-1)^2\left(1-\beta_2\right)^{3/2}}, \end{aligned} \tag{B.16}$$

$$\left[\frac{\varphi_e^{q^2}}{\left(1-\beta_2\right)^{1/2}}\right]^{\lambda} = \frac{\varphi_e^{q^2\lambda}}{\left(1-\beta_2\right)^{1/2}} + \frac{\varphi_e^{q^2}\beta_2^{\lambda}}{2\left(1-\beta_2\right)^{3/2}}, \tag{B.17}$$

$$\left[\frac{\varphi_e'}{\left(1-\beta_2\right)^{1/2}}\right]' = \frac{\varphi_e''}{\sqrt{1-\beta_2}} + \frac{\varphi_e'\beta_2'}{2\left(1-\beta_2\right)^{3/2}} \tag{B.18}$$

and the derivative of the elliptical integral of the second kind $E(\varphi_{\rm e}, k_r)$ is

$$E'(\varphi_{\rm e}, k_r) = \frac{1}{2}\left[E(\varphi_{\rm e}, k_r) - F(\varphi_{\rm e}, k_r)\right]\frac{k_r'}{k_r} + \varphi_{\rm e}'\left(1-\beta_2\right)^{1/2}. \tag{B.19}$$

We determined new expressions in the derivatives above, $\beta_1$ and $\beta_2$

$$\beta_1 = \frac{(r_2 - r_4)(r_e - r_1)}{(r_1 - r_4)(r_e - r_2)}, \tag{B.20}$$

$$k_r\beta_1 = \beta_2 = \frac{(r_2 - r_3)(r_e - r_1)}{(r_1 - r_3)(r_e - r_2)} \tag{B.21}$$

and their derivatives are

$$\beta_1' = \left[-\frac{(r_1' - r_4')}{(r_1 - r_4)} + \frac{(r_2' - r_4')}{(r_2 - r_4)} - \frac{r_1'}{(r_e - r_1)} + \frac{r_2'}{(r_e - r_2)}\right]\beta_1, \tag{B.22}$$

$$\begin{aligned}\beta_1^{q^2\lambda} &= \frac{\beta_1^{q^2}\beta_1^{\lambda}}{\beta_1} + \beta_1\left[-\frac{(r_1^{q^2\lambda} - r_4^{q^2\lambda})}{(r_1 - r_4)} + \frac{(r_2^{q^2\lambda} - r_4^{q^2\lambda})}{(r_2 - r_4)}\right. \\ &- \frac{r_1^{q^2\lambda}}{(r_e - r_1)} + \frac{r_2^{q^2\lambda}}{(r_e - r_2)} + \frac{(r_1^{\lambda} - r_4^{\lambda})(r_1^{q^2} - r_4^{q^2})}{(r_1 - r_4)^2} \\ &\left.- \frac{(r_2^{\lambda} - r_4^{\lambda})(r_2^{q^2} - r_4^{q^2})}{(r_2 - r_4)^2} - \frac{r_1^{\lambda}r_1^{q^2}}{(r_e - r_1)^2} + \frac{r_2^{\lambda}r_2^{q^2}}{(r_e - r_2)^2}\right],\end{aligned} \tag{B.23}$$

$$\begin{aligned}\beta_1'' &= \frac{(\beta_1')^2}{\beta_1} + \beta_1\left[-\frac{(r_1'' - r_4'')}{(r_1 - r_4)} + \frac{(r_2'' - r_4'')}{(r_2 - r_4)}\right. \\ &- \frac{r_1''}{(r_e - r_1)} + \frac{r_2''}{(r_e - r_2)} + \frac{(r_1' - r_4')^2}{(r_1 - r_4)^2} \\ &\left.- \frac{(r_2' - r_4')^2}{(r_2 - r_4)^2} - \frac{(r_1')^2}{(r_e - r_1)^2} + \frac{(r_2')^2}{(r_e - r_2)^2}\right]\end{aligned} \tag{B.24}$$

and

$$\beta_2' = \left[-\frac{(r_1' - r_3')}{(r_1 - r_3)} + \frac{(r_2' - r_3')}{(r_2 - r_3)} - \frac{r_1'}{(r_e - r_1)} + \frac{r_2'}{(r_e - r_2)}\right]\beta_1 = k_r'\beta_1 + k_r\beta_1'. \tag{B.25}$$

The derivatives of arguments in $F(\varphi_{\rm e}, k_r)$ are

$$k_r' = \left[-\frac{r_1' - r_3'}{r_1 - r_3} + \frac{r_2' - r_3'}{r_2 - r_3} + \frac{r_1' - r_4'}{r_1 - r_4} - \frac{r_2' - r_4'}{r_2 - r_4}\right]k_r, \tag{B.26}$$

$$\begin{aligned}k_r^{q^2\lambda} &= \frac{(k_r')^2}{k_r} + k_r\left[-\frac{r_1^{q^2\lambda} - r_3^{q^2\lambda}}{r_1 - r_3} + \frac{r_2^{q^2\lambda} - r_3^{q^2\lambda}}{r_2 - r_3}\right. \\ &+ \frac{r_1^{q^2\lambda} - r_4^{q^2\lambda}}{r_1 - r_4} - \frac{r_2^{q^2\lambda} - r_4^{q^2\lambda}}{r_2 - r_4} \\ &+ \frac{(r_1^{\lambda} - r_3^{\lambda})(r_1^{q^2} - r_3^{q^2})}{(r_1 - r_3)^2} - \frac{(r_2^{\lambda} - r_3^{\lambda})(r_2^{q^2} - r_3^{q^2})}{(r_2 - r_3)^2} \\ &\left.+ -\frac{(r_1^{\lambda} - r_4^{\lambda})(r_1^{q^2} - r_4^{q^2})}{(r_1 - r_4)^2} + \frac{(r_2^{\lambda} - r_4^{\lambda})(r_2^{q^2} - r_4^{q^2})}{(r_2 - r_4)^2}\right],\end{aligned} \tag{B.27}$$

$$k_r'' = \frac{(k_r')^2}{k_r} + k_r \left[ -\frac{r_1'' - r_3''}{r_1 - r_3} + \frac{r_2'' - r_3''}{r_2 - r_3} + \frac{r_1'' - r_4''}{r_1 - r_4} - \frac{r_2'' - r_4''}{r_2 - r_4} + \frac{(r_1' - r_3')^2}{(r_1 - r_3)^2} - \frac{(r_2' - r_3')^2}{(r_2 - r_3)^2} - \frac{(r_1' - r_4')^2}{(r_1 - r_4)^2} + \frac{(r_2' - r_4')^2}{(r_2 - r_4)^2} \right] \tag{B.28}$$

and

$$\varphi_{\rm e}' = \frac{\beta_1'}{2\left[\beta_1\left(1-\beta_1\right)\right]^{1/2}}, \tag{B.29}$$

$$\varphi_{\rm e}^{q^2\lambda} = \frac{\beta_1^{q^2\lambda}}{2\left[\beta_1\left(1-\beta_1\right)\right]^{1/2}} - \frac{\beta_1^{q^2}\beta_1^{\lambda}(1-2\beta_1)}{4\left[\beta_1\left(1-\beta_1\right)\right]^{3/2}}, \tag{B.30}$$

$$\varphi_{\rm e}'' = \frac{\beta_1''}{2\left[\beta_1\left(1-\beta_1\right)\right]^{1/2}} - \frac{(\beta_1')^2(1-2\beta_1)}{4\left[\beta_1\left(1-\beta_1\right)\right]^{3/2}}. \tag{B.31}$$

The derivatives of $F(\varphi_{\rm o}, k_r)$ in eq. (3.11) are

$$F'(\varphi_{\rm o}, k_r) = \left[ -\frac{F(\varphi_{\rm o}, k_r)}{2k_r} - \frac{E(\varphi_{\rm o}, k_r)}{2k_r(k_r-1)} + \frac{\sin 2\varphi_{\rm o}}{4(k_r-1)\left(1-\gamma_2\right)^{1/2}} \right] k_r' + \frac{\varphi_{\rm o}'}{\left(1-\gamma_2\right)^{1/2}}, \tag{B.32}$$

$$F^{q^2\lambda}(\varphi_{\rm o}, k_r) = \left[ -\frac{F(\varphi_{\rm o}, k_r)}{2k_r} - \frac{E(\varphi_{\rm o}, k_r)}{2k_r(k_r-1)} \right]^{\lambda} k_r^{q^2} + \left[ \frac{\sin 2\varphi_{\rm o}}{4(k_r-1)\left(1-\gamma_2\right)^{1/2}} \right]^{\lambda} k_r^{q^2} + \left[ \frac{\varphi_{\rm o}^{q^2}}{\left(1-\gamma_2\right)^{1/2}} \right]^{\lambda} + \left[ -\frac{F(\varphi_{\rm o}, k_r)}{2k_r} - \frac{E(\varphi_{\rm o}, k_r)}{2k_r(k_r-1)} + \frac{\sin 2\varphi_{\rm o}}{4(k_r-1)\left(1-\gamma_2\right)^{1/2}} \right] k_r^{q^2\lambda}, \tag{B.33}$$

$$F''(\varphi_{\rm o}, k_r) = \left[ -\frac{F(\varphi_{\rm o}, k_r)}{2k_r} - \frac{E(\varphi_{\rm o}, k_r)}{2k_r(k_r-1)} \right]' k_r' + \left[ \frac{\sin 2\varphi_{\rm o}}{4(k_r-1)\left(1-\gamma_2\right)^{1/2}} \right]' k_r' + \left[ \frac{\varphi_{\rm o}'}{\left(1-\gamma_2\right)^{1/2}} \right]' + \left[ -\frac{F(\varphi_{\rm o}, k_r)}{2k_r} - \frac{E(\varphi_{\rm o}, k_r)}{2k_r(k_r-1)} + \frac{\sin 2\varphi_{\rm o}}{4(k_r-1)\left(1-\gamma_2\right)^{1/2}} \right] k_r'', \tag{B.34}$$

where

$$\left[-\frac{F(\varphi_o,k_r)}{2k_r}-\frac{E(\varphi_o,k_r)}{2k_r(k_r-1)}\right]' = -\frac{F'(\varphi_o,k_r)}{2k_r}-\frac{E'(\varphi_o,k_r)}{2k_r(k_r-1)} + \left[\frac{F(\varphi_o,k_r)}{2k_r^2}+\frac{E(\varphi_o,k_r)(2k_r-1)}{2k_r^2(k_r-1)^2}\right]k_r', \tag{B.35}$$

$$\left[\frac{\sin 2\varphi_o}{4(k_r-1)\left(1-\gamma_2\right)^{1/2}}\right]' = \frac{\varphi_o'\cos 2\varphi_o}{2(k_r-1)\left(1-\gamma_2\right)^{1/2}} - \frac{\sin 2\varphi_o(2k_r'-2k_r'\gamma_2-k_r\gamma_2'+\gamma_2')}{8(k_r-1)^2\left(1-\gamma_2\right)^{3/2}}, \tag{B.36}$$

$$\left[\frac{\varphi_o^{q^2}}{\left(1-\gamma_2\right)^{1/2}}\right]^{\lambda} = \frac{\varphi_o^{q^2\lambda}}{\left(1-\gamma_2\right)^{1/2}}+\frac{\varphi_o^{q^2}\gamma_2^{\lambda}}{2\left(1-\gamma_2\right)^{3/2}}, \tag{B.37}$$

$$\left[\frac{\varphi_o'}{\sqrt{1-\gamma_2}}\right]' = \frac{\varphi_o''}{\left(1-\gamma_2\right)^{1/2}}+\frac{\varphi_o'\gamma_2'}{2\left(1-\gamma_2\right)^{3/2}} \tag{B.38}$$

and

$$E'(\varphi_o,k_r)=\frac{1}{2}\left[E(\varphi_o,k_r)-F(\varphi_o,k_r)\right]\frac{k_r'}{k_r}+\varphi_o'\left(1-\gamma_2\right)^{1/2}. \tag{B.39}$$

We determined new expressions in the derivatives above, $\gamma_1$ and $\gamma_2$

$$\gamma_1=\frac{r_2-r_4}{r_1-r_4}, \tag{B.40}$$

$$k_r\gamma_1=\gamma_2=\frac{r_2-r_3}{r_1-r_3} \tag{B.41}$$

and their derivatives are

$$\gamma_1' = \left[-\frac{(r_1'-r_4')}{(r_1-r_4)}+\frac{(r_2'-r_4')}{(r_2-r_4)}\right]\gamma_1, \tag{B.42}$$

$$\gamma_1^{q^2\lambda} = \frac{\gamma_1^{q^2}\gamma_1^{\lambda}}{\gamma_1}+\left[-\frac{(r_1^{q^2\lambda}-r_4^{q^2\lambda})}{(r_1-r_4)}+\frac{(r_2^{q^2\lambda}-r_4^{q^2\lambda})}{(r_2-r_4)} + \frac{(r_1^{\lambda}-r_4^{\lambda})(r_1^{q^2}-r_4^{q^2})}{(r_1-r_4)^2}-\frac{(r_2^{\lambda}-r_4^{\lambda})(r_2^{q^2}-r_4^{q^2})}{(r_2-r_4)^2}\right]\gamma_1, \tag{B.43}$$

$$\gamma_1'' = \frac{(\gamma_1')^2}{\gamma_1}+\left[-\frac{(r_1''-r_4'')}{(r_1-r_4)}+\frac{(r_2''-r_4'')}{(r_2-r_4)} + \frac{(r_1'-r_4')^2}{(r_1-r_4)^2}-\frac{(r_2'-r_4')^2}{(r_2-r_4)^2}\right]\gamma_1 \tag{B.44}$$

and

$$\gamma_2'=\left[-\frac{(r_1'-r_3')}{(r_1-r_3)}+\frac{(r_2'-r_3')}{(r_2-r_3)}\right]\gamma_1=k_r'\gamma_1+k_r\gamma_1'. \tag{B.45}$$

The derivatives of argument, $\varphi_o$ in $F(\varphi_o,k_r)$ are

$$\varphi_o'=\frac{\gamma_1'}{2\left[\gamma_1\left(1-\gamma_1\right)\right]^{1/2}}, \tag{B.46}$$

$$\varphi_{\rm o}^{q^2\lambda} = \frac{\gamma_1^{q^2\lambda}}{2\left[\gamma_1\left(1-\gamma_1\right)\right]^{1/2}} - \frac{\gamma_1^{q^2}\gamma_1^{\lambda}(1-2\gamma_1)}{2\left[\gamma_1\left(1-\gamma_1\right)\right]^{3/2}}, \tag{B.47}$$

$$\varphi_{\rm o}'' = \frac{\gamma_1''}{2\left[\gamma_1\left(1-\gamma_1\right)\right]^{1/2}} - \frac{(\gamma_1')^2(1-2\gamma_1)}{2\sqrt{\gamma_1^3}\left[\gamma_1\left(1-\gamma_1\right)\right]^{3/2}}. \tag{B.48}$$

## B.2 Radial direction, two complex roots

The derivatives of $g_{rc}(\lambda, q^2)$ in (3.12) are

$$g_{rc}' = -\frac{g_{rc}}{2}\left[\frac{A_{\rm c}'}{A_{\rm c}} + \frac{B_{\rm c}'}{B_{\rm c}}\right], \tag{B.49}$$

$$g_{\rm rc}^{q^2\lambda} = \frac{g_{rc}^{q^2} g_{rc}^{\lambda}}{g_{rc}} - \frac{g_{rc}}{2}\left[\frac{A_{\rm c}^{q^2\lambda}}{A_{\rm c}} + \frac{B_{\rm c}^{q^2\lambda}}{B_{\rm c}} - \frac{A_{\rm c}^{q^2}A_{\rm c}^{\lambda}}{A_{\rm c}^2} - \frac{B_{\rm c}^{q^2}B_{\rm c}^{\lambda}}{B_{\rm c}^2}\right], \tag{B.50}$$

$$g_{rc}'' = \frac{(g_{rc}')^2}{g_{rc}} - \frac{g_{rc}}{2}\left[\frac{A_{\rm c}''}{A_{\rm c}} + \frac{B_{\rm c}''}{B_{\rm c}} - \frac{(A_{\rm c}')^2}{A_{\rm c}^2} - \frac{(B_{\rm c}')^2}{B_{\rm c}^2}\right]. \tag{B.51}$$

The derivatives of $F(\varphi_{\rm ec}, k_{\rm rc})$ in (3.12) are

$$\begin{aligned} F'(\varphi_{\rm ec}, k_{\rm rc}) \;=\; & \left\{-\frac{F(\varphi_{\rm ec}, k_{\rm rc})}{2k_{rc}} - \frac{E(\varphi_{\rm ec}, k_{\rm rc})}{2k_{\rm rc}(k_{\rm rc}-1)}\right\} k_{\rm rc}' \\ & + \left\{\frac{\sin 2\varphi_{\rm ec}}{4(k_{\rm rc}-1)\left[1-k_{\rm rc}(1-\sigma^2)\right]^{1/2}}\right\} k_{\rm rc}' \\ & + \frac{\varphi_{\rm ec}'}{\left[1-k_{\rm rc}(1-\sigma^2)\right]^{1/2}}, \end{aligned} \tag{B.52}$$

$$\begin{aligned} F^{q^2\lambda}(\varphi_{\rm ec}, k_{\rm rc}) \;=\; & \left\{-\frac{F(\varphi_{\rm ec}, k_{\rm rc})}{2k_{rc}} - \frac{E(\varphi_{\rm ec}, k_{\rm rc})}{2k_{\rm rc}(k_{\rm rc}-1)}\right\}^{\lambda} k_{\rm rc}^{q^2} \\ & + \left\{\frac{\sin 2\varphi_{\rm ec}}{4(k_{\rm rc}-1)\left[1-k_{\rm rc}(1-\sigma^2)\right]^{1/2}}\right\}^{\lambda} k_{\rm rc}^{q^2} \\ & + \left\{\frac{\varphi_{\rm ec}^{q^2}}{\left[1-k_{\rm rc}(1-\sigma^2)\right]^{1/2}}\right\}^{\lambda} \\ & + \left\{-\frac{F(\varphi_{\rm ec}, k_{\rm rc})}{2k_{rc}} - \frac{E(\varphi_{\rm ec}, k_{\rm rc})}{2k_{\rm rc}(k_{\rm rc}-1)}\right. \\ & \left. + \frac{\sin 2\varphi_{\rm ec}}{4(k_{\rm rc}-1)\left[1-k_{\rm rc}(1-\sigma^2)\right]^{1/2}}\right\} k_{\rm rc}^{q^2\lambda}, \end{aligned} \tag{B.53}$$

$$
\begin{aligned}
F''(\varphi_{\rm ec},k_{\rm rc}) &= \left\{-\frac{F(\varphi_{\rm ec},k_{\rm rc})}{2k_{\rm rc}}-\frac{E(\varphi_{\rm ec},k_{\rm rc})}{2k_{\rm rc}(k_{\rm rc}-1)}\right\}' k'_{\rm rc} \\
&+\left\{\frac{\sin 2\varphi_{\rm ec}}{4(k_{\rm rc}-1)\sqrt{1-k_{\rm rc}(1-\sigma^2)}}\right\}' k'_{\rm rc} \\
&+\left\{\frac{\varphi'_{\rm ec}}{\left[1-k_{\rm rc}(1-\sigma^2)\right]^{1/2}}\right\}' \\
&+\left\{-\frac{F(\varphi_{\rm ec},k_{\rm rc})}{2k_{\rm rc}}-\frac{E(\varphi_{\rm ec},k_{\rm rc})}{2k_{\rm rc}(k_{\rm rc}-1)}\right. \\
&\left.+\frac{\sin 2\varphi_{\rm ec}}{4(k_{\rm rc}-1)\left[1-k_{\rm rc}(1-\sigma^2)\right]^{1/2}}\right\} k''_{\rm rc},
\end{aligned}
\tag{B.54}
$$

where

$$
\begin{aligned}
&\left\{-\frac{F(\varphi_{\rm ec},k_r)}{2k_{\rm rc}}-\frac{E(\varphi_{\rm ec},k_{\rm rc})}{2k_{\rm rc}(k_{\rm rc}-1)}\right\}' = -\frac{F'(\varphi_{\rm ec},k_{\rm rc})}{2k_{\rm rc}}-\frac{E'(\varphi_{\rm ec},k_{\rm rc})}{2k_{\rm rc}(k_{\rm rc}-1)} \\
&+\left[\frac{F(\varphi_{\rm ec},k_{\rm rc})}{2k_{\rm rc}^2}+\frac{E(\varphi_{\rm ec},k_{\rm rc})(2k_{\rm rc}-1)}{2k_{\rm rc}^2(k_{\rm rc}-1)^2}\right] k'_{\rm rc},
\end{aligned}
\tag{B.55}
$$

$$
\begin{aligned}
&\left\{\frac{\sin 2\varphi_{\rm ec}}{4(k_{\rm rc}-1)\left[1-k_{\rm rc}(1-\sigma^2)\right]^{1/2}}\right\}' = \frac{\varphi'_{\rm ec}\cos 2\varphi_{\rm ec}}{2(k_{\rm rc}-1)\left[1-k_{\rm rc}(1-\sigma^2)\right]^{1/2}} \\
&-\frac{\sin 2\varphi_{\rm ec}(3k'_{\rm rc}(1-k_{\rm rc}+k_{\rm rc}\sigma^2)+2k_{\rm rc}\sigma\sigma'(k_{\rm rc}-1)-k'_{\rm rc}\sigma^2)}{8(k_{\rm rc}-1)^2\left[1-k_{\rm rc}(1-\sigma^2)\right]^{3/2}},
\end{aligned}
\tag{B.56}
$$

$$
\begin{aligned}
\left\{\frac{\varphi_{\rm ec}^{q^2}}{\sqrt{1-k_{\rm rc}(1-\sigma^2)}}\right\}^{\lambda} &= \frac{\varphi_{\rm ec}^{q^2\lambda}}{\left[1-k_{\rm rc}(1-\sigma^2)\right]^{1/2}} \\
&-\frac{1}{2}\frac{\varphi_{\rm ec}^{q^2}(-k_{\rm rc}^{\lambda}+k_{\rm rc}^{\lambda}\sigma^2+2k_{\rm rc}\sigma\sigma^{\lambda})}{\left[1-k_{\rm rc}(1-\sigma^2)\right]^{3/2}},
\end{aligned}
\tag{B.57}
$$

$$
\begin{aligned}
\left\{\frac{\varphi'_{\rm ec}}{\sqrt{1-k_{\rm rc}(1-\sigma^2)}}\right\}' &= \frac{\varphi''_{\rm ec}}{\left[1-k_{\rm rc}(1-\sigma^2)\right]^{1/2}} \\
&-\frac{1}{2}\frac{\varphi'_{\rm ec}(-k'_{\rm rc}+k'_{\rm rc}\sigma^2+2k_{\rm rc}\sigma\sigma')}{\left[1-k_{\rm rc}(1-\sigma^2)\right]^{3/2}}
\end{aligned}
\tag{B.58}
$$

and

$$
E'(\varphi_{\rm ec},k_{\rm rc}) = \frac{1}{2}\left[E(\varphi_{\rm ec},k_{\rm rc})-F(\varphi_{\rm ec},k_{\rm rc})\right]\frac{k'_{\rm rc}}{k_{\rm rc}}+\varphi'_{\rm ec}\left[1-k_{\rm rc}(1-\sigma^2)\right]^{1/2}. \tag{B.59}
$$

We determined new expression in the derivatives above, $\sigma$

$$
\sigma = \frac{(A_{\rm c}-B_{\rm c})r_{\rm e}+B_{\rm c}r_3-A_{\rm c}r_4}{(A_{\rm c}+B_{\rm c})r_{\rm e}-B_{\rm c}r_3-A_{\rm c}r_4} \tag{B.60}
$$

and its derivatives are

$$\begin{aligned}
\sigma' &= \left[\frac{(A'_{\rm c}-B'_{\rm c})r_{\rm e}+B'_{\rm c}r_3+B_{\rm c}r'_3-A'_{\rm c}r_4-A_{\rm c}r'_4}{(A_{\rm c}-B_{\rm c})r_{\rm e}+B_{\rm c}r_3-A_{\rm c}r_4}\right. \\
&\quad \left.-\frac{(A'_{\rm c}+B'_{\rm c})r_{\rm e}-B'_{\rm c}r_3-B_{\rm c}r'_3-A'_{\rm c}r_4-A_{\rm c}r'_4}{(A_{\rm c}+B_{\rm c})r_{\rm e}-B_{\rm c}r_3-A_{\rm c}r_4}\right]\sigma, \qquad \text{(B.61)}\\
\sigma^{q^2\lambda} &= \frac{\sigma^{\lambda}\sigma^{q^2}}{\sigma}+\sigma\left\{\frac{(A_{\rm c}^{q^2\lambda}-B_{\rm c}^{q^2\lambda})r_{\rm e}+B_{\rm c}^{q^2\lambda}r_3+B_{\rm c}^{q^2}r_3^{\lambda}+B_{\rm c}^{\lambda}r_3^{q^2}+B_{\rm c}r_3^{q^2\lambda}}{(A_{\rm c}-B_{\rm c})r_{\rm e}+B_{\rm c}r_3-A_{\rm c}r_4}\right. \\
&\quad +\frac{-A_{\rm c}^{q^2\lambda}r_4-A_{\rm c}^{q^2}r_4^{\lambda}-A_{\rm c}^{\lambda}r_4^{q^2}-A_{\rm c}r_4^{q^2\lambda}}{(A_{\rm c}-B_{\rm c})r_{\rm e}+B_{\rm c}r_3-A_{\rm c}r_4} \qquad \text{(B.62)}\\
&\quad -\left[(A_{\rm c}^{q^2}-B_{\rm c}^{q^2})r_{\rm e}+B_{\rm c}^{q^2}r_3+B_{\rm c}r_3^{q^2}-A_{\rm c}^{q^2}r_4-A_{\rm c}r_4^{q^2}\right] \\
&\quad {\rm x}\frac{\left[(A_{\rm c}^{\lambda}-B_{\rm c}^{\lambda})r_{\rm e}+B_{\rm c}^{\lambda}r_3+B_{\rm c}r_3^{\lambda}-A_{\rm c}^{\lambda}r_4-A_{\rm c}r_4^{\lambda}\right]}{\left[(A_{\rm c}-B_{\rm c})r_{\rm e}+B_{\rm c}r_3-A_{\rm c}r_4\right]^2} \\
&\quad -\frac{(A_{\rm c}^{q^2\lambda}+B_{\rm c}^{q^2\lambda})r_{\rm e}-B_{\rm c}^{q^2\lambda}r_3-B_{\rm c}^{q^2}r_3^{\lambda}-B_{\rm c}^{\lambda}r_3^{q^2}-B_{\rm c}r_3^{q^2\lambda}}{(A_{\rm c}+B_{\rm c})r_{\rm e}-B_{\rm c}r_3-A_{\rm c}r_4} \\
&\quad +\frac{-A_{\rm c}^{q^2\lambda}r_4-A_{\rm c}^{q^2}r_4^{\lambda}-A_{\rm c}^{\lambda}r_4^{q^2}-A_{\rm c}r_4^{q^2\lambda}}{(A_{\rm c}+B_{\rm c})r_{\rm e}-B_{\rm c}r_3-A_{\rm c}r_4} \\
&\quad +\left[(A_{\rm c}^{q^2}+B_{\rm c}^{q^2})r_{\rm e}-B_{\rm c}^{q^2}r_3-B_{\rm c}r_3^{q^2}-A_{\rm c}^{q^2}r_4-A_{\rm c}r_4^{q^2}\right] \\
&\quad \left.{\rm x}\frac{\left[(A_{\rm c}^{\lambda}+B_{\rm c}^{\lambda})r_{\rm e}-B_{\rm c}^{\lambda}r_3-B_{\rm c}r_3^{\lambda}-A_{\rm c}^{\lambda}r_4-A_{\rm c}r_4^{\lambda}\right]}{\left[(A_{\rm c}+B_{\rm c})r_{\rm e}-B_{\rm c}r_3-A_{\rm c}r_4\right]^2}\right\}. \\
\sigma'' &= \frac{(\sigma')^2}{\sigma}+\sigma\left\{\frac{(A''_{\rm c}-B''_{\rm c})r_{\rm e}+B''_{\rm c}r_3+2B'_{\rm c}r'_3+B_{\rm c}r''_3}{(A_{\rm c}-B_{\rm c})r_{\rm e}+B_{\rm c}r_3-A_{\rm c}r_4}\right. \qquad \text{(B.63)}\\
&\quad -\frac{A''_{\rm c}r_4+2A'_{\rm c}r'_4+A_{\rm c}r''_4}{(A_{\rm c}-B_{\rm c})r_{\rm e}+B_{\rm c}r_3-A_{\rm c}r_4} \\
&\quad -\frac{\left[(A'_{\rm c}-B'_{\rm c})r_{\rm e}+B'_{\rm c}r_3+B_{\rm c}r'_3-A'_{\rm c}r_4-A_{\rm c}r'_4\right]^2}{\left[(A_{\rm c}-B_{\rm c})r_{\rm e}+B_{\rm c}r_3-A_{\rm c}r_4\right]^2} \\
&\quad -\frac{(A''_{\rm c}+B''_{\rm c})r_{\rm e}-B''_{\rm c}r_3-2B'_{\rm c}r'_3-B_{\rm c}r''_3-A''_{\rm c}r_4-2A'_{\rm c}r'_4-A_{\rm c}r''_4}{(A_{\rm c}+B_{\rm c})r_{\rm e}-B_{\rm c}r_3-A_{\rm c}r_4} \\
&\quad \left.+\frac{\left[(A'_{\rm c}+B'_{\rm c})r_{\rm e}-B'_{\rm c}r_3-B_{\rm c}r'_3-A'_{\rm c}r_4-A_{\rm c}r'_4\right]^2}{\left[(A_{\rm c}+B_{\rm c})r_{\rm e}-B_{\rm c}r_3-A_{\rm c}r_4\right]^2}\right\}.
\end{aligned}$$

The derivatives of arguments in $F(\varphi_{\rm ec}, k_{rc})$ are

$$k'_{\rm rc}=\left[-(\frac{A'_{\rm c}}{A_{\rm c}}+\frac{B'_{\rm c}}{B_{\rm c}})+\frac{2(A_{\rm c}+B_{\rm c})(A'_{\rm c}+B'_{\rm c})-2(r_3-r_4)(r'_3-r'_4)}{(A_{\rm c}+B_{\rm c})^2-(r_3-r_4)^2}\right]k_{rc}, \qquad \text{(B.64)}$$

$$
\begin{aligned}
k_{rc}^{q^2\lambda} &= \frac{k_{rc}^{q^2}k_{rc}^{\lambda}}{k_{rc}} + k_{rc}\left[-\frac{A_c^{q^2\lambda}}{A_c} - \frac{B_c^{q^2\lambda}}{B_c} + \frac{A_c^{q^2}A_c^{\lambda}}{A_c^2} + \frac{B_c^{q^2}B_c^{\lambda}}{B_c^2}\right. \qquad \text{(B.65)}\\
&\quad - \left[2(A_c+B_c)(A_c^{q^2}+B_c^{q^2}) - 2(r_3-r_4)(r_3^{q^2}-r_4^{q^2})\right]\\
&\quad \text{x}\frac{\left[2(A_c+B_c)(A_c^{\lambda}+B_c^{\lambda}) - 2(r_3-r_4)(r_3^{\lambda}-r_4^{\lambda})\right]}{\left[(A_c+B_c)^2-(r_3-r_4)^2\right]^2}\\
&\quad + \frac{2(A_c^{q^2}+B_c^{q^2})(A_c^{\lambda}+B_c^{\lambda}) + 2(A_c+B_c)(A_c^{q^2\lambda}+B_c^{q^2\lambda})}{(A_c+B_c)^2-(r_3-r_4)^2}\\
&\quad \left. + \frac{-2(r_3^{q^2}-r_4^{q^2})(r_3^{\lambda}-r_4^{\lambda}) - 2(r_3-r_4)(r_3^{q^2\lambda}-r_4^{q^2\lambda})}{(A_c+B_c)^2-(r_3-r_4)^2}\right],\\
k_{rc}'' &= \frac{(k_{rc}')^2}{k_{rc}} + k_{rc}\left\{-\left[\frac{A_c''}{A_c} + \frac{B_c''}{B_c} - \frac{(A_c')^2}{A_c^2} - \frac{(B_c')^2}{B_c^2}\right]\right. \qquad \text{(B.66)}\\
&\quad - \left[\frac{2(A_c+B_c)(A_c'+B_c') - 2(r_3-r_4)(r_3'-r_4')}{(A_c+B_c)^2-(r_3-r_4)^2}\right]^2\\
&\quad + \frac{2(A_c'+B_c')^2 + 2(A_c+B_c)(A_c''+B_c'')}{(A_c+B_c)^2-(r_3-r_4)^2}\\
&\quad \left. + \frac{-2(r_3'-r_4')^2 - 2(r_3-r_4)(r_3''-r_4'')}{(A_c+B_c)^2-(r_3-r_4)^2}\right\},
\end{aligned}
$$

where

$$
\begin{aligned}
A_c' &= \frac{(r_3-u)(r_3'-u') + vv'}{A_c}, \qquad \text{(B.67)}\\
A_c^{q^2\lambda} &= \frac{(r_3^{q^2}-u^{q^2})(r_3^{\lambda}-u^{\lambda}) + (r_3-u)(r_3^{q^2\lambda}-u^{q^2\lambda})}{A_c} \qquad \text{(B.68)}\\
&\quad + \frac{v^{q^2}v^{\lambda} + vv^{q^2\lambda} - A_c^{q^2}A_c^{\lambda}}{A_c},\\
A_c'' &= \frac{(r_3'-u')^2 + (r_3-u)(r_3''-u'') + (v')^2 + vv'' - (A_c')^2}{A_c}, \qquad \text{(B.69)}
\end{aligned}
$$

$$
\begin{aligned}
B_c' &= \frac{(r_4-u)(r_4'-u') + vv'}{B_c}, \qquad \text{(B.70)}\\
B_c^{q^2\lambda} &= \frac{(r_4^{q^2}-u^{q^2})(r_4^{\lambda}-u^{\lambda}) + (r_4-u)(r_4^{q^2\lambda}-u^{q^2\lambda})}{B_c} \qquad \text{(B.71)}\\
&\quad + \frac{v^{q^2}v^{\lambda} + vv^{q^2\lambda} - B_c^{q^2}B_c^{\lambda}}{B_c}\\
B_c'' &= \frac{(r_4'-u')^2 + (r_4-u)(r_4''-u'') + (v')^2 + vv'' - (B_c')^2}{B_c}; \qquad \text{(B.72)}
\end{aligned}
$$

and

$$\varphi'_{\rm ec} = \frac{-\sigma'}{(1-\sigma^2)^{1/2}}, \tag{B.73}$$

$$\varphi^{q^2\lambda}_{\rm ec} = \frac{-\sigma^{q^2\lambda}}{(1-\sigma^2)^{1/2}} - \frac{\sigma^{q^2}\sigma^{\lambda}\sigma}{(1-\sigma^2)^{3/2}}, \tag{B.74}$$

$$\varphi''_{\rm ec} = \frac{-\sigma''}{(1-\sigma^2)^{1/2}} - \frac{(\sigma')^2\sigma}{(1-\sigma^2)^{3/2}}. \tag{B.75}$$

The derivatives of $F(\varphi_{\rm oc}, k_{\rm rc})$ in (3.12) are

$$\begin{aligned} F'(\varphi_{\rm oc}, k_{\rm rc}) &= \left[-\frac{F(\varphi_{\rm oc}, k_{\rm rc})}{2k_{\rm rc}} - \frac{E(\varphi_{\rm oc}, k_{\rm rc})}{2k_{\rm rc}(k_{\rm rc}-1)}\right] k'_{\rm rc} \\ &+ \left[\frac{\sin 2\varphi_{\rm oc}}{4(k_{\rm rc}-1)\sqrt{1-k_{\rm rc}(1-\omega^2)}}\right] k'_{\rm rc} \\ &+ \frac{\varphi'_{\rm oc}}{[1-k_{\rm rc}(1-\omega^2)]^{1/2}}, \end{aligned} \tag{B.76}$$

$$\begin{aligned} F^{q^2\lambda}(\varphi_{\rm oc}, k_{\rm rc}) &= \left\{-\frac{F(\varphi_{\rm oc}, k_{\rm rc})}{2k_{\rm rc}} - \frac{E(\varphi_{\rm oc}, k_{\rm rc})}{2k_{\rm rc}(k_{\rm rc}-1)}\right\}^{\lambda} k_{\rm rc}^{q^2} \\ &+ \left\{\frac{\sin 2\varphi_{\rm oc}}{4(k_{\rm rc}-1)\left[1-k_{\rm rc}(1-\omega^2)\right]^{1/2}}\right\}^{\lambda} k_{\rm rc}^{q^2} \\ &+ \left\{\frac{\varphi_{\rm oc}^{q^2}}{\left[1-k_{\rm rc}(1-\omega^2)\right]^{1/2}}\right\}^{\lambda} \\ &+ \left\{-\frac{F(\varphi_{\rm oc}, k_{\rm rc})}{2k_{\rm rc}} - \frac{E(\varphi_{\rm oc}, k_{\rm rc})}{2k_{\rm rc}(k_{\rm rc}-1)}\right\} k_{\rm rc}^{q^2\lambda} \\ &+ \left\{\frac{\sin 2\varphi_{\rm oc}}{4(k_{\rm rc}-1)\left[1-k_{\rm rc}(1-\omega^2)\right]^{1/2}}\right\} k_{\rm rc}^{q^2\lambda}, \end{aligned} \tag{B.77}$$

$$\begin{aligned} F''(\varphi_{\rm oc}, k_{\rm rc}) &= \left\{-\frac{F(\varphi_{\rm oc}, k_{\rm rc})}{2k_{\rm rc}} - \frac{E(\varphi_{\rm oc}, k_{\rm rc})}{2k_{\rm rc}(k_{\rm rc}-1)}\right\}' k'_{\rm rc} \\ &+ \left\{\frac{\sin 2\varphi_{\rm oc}}{4(k_{\rm rc}-1)\left[1-k_{\rm rc}(1-\omega^2)\right]^{1/2}}\right\}' k'_{\rm rc} \\ &+ \left\{\frac{\varphi'_{\rm oc}}{\left[1-k_{\rm rc}(1-\omega^2)\right]^{1/2}}\right\}' \\ &+ \left\{-\frac{F(\varphi_{\rm oc}, k_{\rm rc})}{2k_{\rm rc}} - \frac{E(\varphi_{\rm oc}, k_{\rm rc})}{2k_{\rm rc}(k_{\rm rc}-1)}\right\} k''_{\rm rc} \\ &+ \left\{\frac{\sin 2\varphi_{\rm oc}}{4(k_{\rm rc}-1)\left[1-k_{\rm rc}(1-\omega^2)\right]^{1/2}}\right\} k''_{\rm rc}, \end{aligned} \tag{B.78}$$

where

$$\left\{-\frac{F(\varphi_{\rm oc},k_{\rm rc})}{2k_{\rm rc}}-\frac{E(\varphi_{\rm oc},k_{\rm rc})}{2k_{\rm rc}(k_{\rm rc}-1)}\right\}'=-\frac{F'(\varphi_{\rm oc},k_{\rm rc})}{2k_{\rm rc}} \\ -\frac{E'(\varphi_{\rm oc},k_{\rm rc})}{2k_{\rm rc}(k_{\rm rc}-1)}+\left[\frac{F(\varphi_{\rm oc},k_{\rm rc})}{2k_{\rm rc}^2}+\frac{E(\varphi_{\rm oc},k_{\rm rc})(2k_{\rm rc}-1)}{2k_{\rm rc}^2(k_{\rm rc}-1)^2}\right]k'_{\rm rc}, \tag{B.79}$$

$$\left\{\frac{\sin 2\varphi_{\rm oc}}{4(k_{\rm rc}-1)\left[1-k_{\rm rc}(1-\omega^2)\right]^{1/2}}\right\}'=\frac{\varphi'_{\rm oc}\cos 2\varphi_{\rm oc}}{2(k_{\rm rc}-1)\left[1-k_{\rm rc}(1-\omega^2)\right]^{1/2}} \\ -\frac{\sin 2\varphi_{\rm oc}\left[3k'_{\rm rc}(1-k_{\rm rc}+k_{\rm rc}\omega^2)+2k_{\rm rc}\omega\omega'(k_{\rm rc}-1)-k'_{\rm rc}\omega^2\right]}{8(k_{\rm rc}-1)^2\left[1-k_{\rm rc}(1-\omega^2)\right]^{3/2}}, \tag{B.80}$$

$$\left\{\frac{\varphi'_{\rm oc}}{\left[1-k_{\rm rc}(1-\omega^2)\right]^{1/2}}\right\}' = \frac{\varphi''_{\rm oc}}{\left[1-k_{\rm rc}(1-\omega^2)\right]^{1/2}} \\ -\frac{1}{2}\frac{\varphi'_{\rm oc}(-k'_{\rm rc}+k'_{\rm rc}\omega^2+2k_{\rm rc}\omega\omega')}{\left[1-k_{\rm rc}(1-\omega^2)\right]^{3/2}} \tag{B.81}$$

and

$$E'(\varphi_{\rm oc},k_{\rm rc})=\frac{1}{2}\left[E(\varphi_{\rm oc},k_{\rm rc})-F(\varphi_{\rm oc},k_{\rm rc})\right]\frac{k'_{\rm rc}}{k_{\rm rc}}+\varphi'_{\rm oc}\left[1-k_{\rm rc}(1-\omega^2)\right]^{1/2}. \tag{B.82}$$

We determined new expression in the derivatives above, $\omega$

$$\omega=\frac{(A_{\rm c}-B_{\rm c})}{(A_{\rm c}+B_{\rm c})}, \tag{B.83}$$

and its derivatives are

$$\omega'=\left[\frac{A'_{\rm c}-B'_{\rm c}}{A_{\rm c}-B_{\rm c}}-\frac{A'_{\rm c}+B'_{\rm c}}{A_{\rm c}+B_{\rm c}}\right]\omega, \tag{B.84}$$

$$\omega^{q^2\lambda} = \frac{\omega^{q^2}\omega^{\lambda}}{\omega}+\omega\left[\frac{A_{\rm c}^{q^2\lambda}-B^{q^2\lambda}}{A_{\rm c}-B_{\rm c}}-\frac{A_{\rm c}^{q^2\lambda}+B_{\rm c}^{q^2\lambda}}{A_{\rm c}+B_{\rm c}}\right. \\ \left.-\frac{(A_{\rm c}^{q^2}-B_{\rm c}^{q^2})(A_{\rm c}^{\lambda}-B_{\rm c}^{\lambda})}{(A_{\rm c}-B_{\rm c})^2}+\frac{(A_{\rm c}^{q^2}+B_{\rm c}^{q^2})(A_{\rm c}^{\lambda}+B_{\rm c}^{\lambda})}{(A_{\rm c}+B_{\rm c})^2}\right], \tag{B.85}$$

and

$$\omega''=\frac{(\omega')^2}{\omega}+\omega\left[\frac{A''_{\rm c}-B''_{\rm c}}{A_{\rm c}-B_{\rm c}}-\frac{A''_{\rm c}+B''_{\rm c}}{A_{\rm c}+B_{\rm c}}-\frac{(A'_{\rm c}-B'_{\rm c})^2}{(A_{\rm c}-B_{\rm c})^2}+\frac{(A'_{\rm c}+B'_{\rm c})^2}{(A_{\rm c}+B_{\rm c})^2}\right], \tag{B.86}$$

The derivatives of argument, $\varphi_{\rm oc}$ in $F(\varphi_{\rm oc}, k_{rc})$ are

$$\varphi'_{\rm oc} = \frac{-\omega'}{(1-\omega^2)^{1/2}}, \tag{B.87}$$

$$\varphi^{q^2\lambda}_{\rm oc} = \frac{-\omega^{q^2\lambda}}{(1-\omega^2)^{1/2}} - \frac{\omega^{q^2}\omega^{\lambda}\omega}{(1-\omega^2)^{3/2}}, \tag{B.88}$$

$$\varphi''_{\rm oc} = \frac{-\omega''}{(1-\omega^2)^{1/2}} - \frac{(\omega')^2\omega}{(1-\omega^2)^{3/2}}. \tag{B.89}$$

## B.3 Latitudinal direction

The derivatives of $g_\mu(\lambda, q^2)$ in eq. (3.21) are

$$g'_\mu = -g_\mu \frac{\mu_-\mu'_- + \mu_+\mu'_+}{\mu_-^2 + \mu_+^2}, \tag{B.90}$$

$$\begin{aligned} g^{q^2\lambda}_\mu &= \frac{g^{q^2}_\mu g^{\lambda}_\mu}{g_\mu} - g_\mu \left[ \frac{\mu_-^{q^2}\mu_-^{\lambda} + \mu_-\mu_-^{q^2\lambda} + \mu_+^{q^2}\mu_+^{\lambda} + \mu_+\mu_+^{\lambda}}{\mu_-^2 + \mu_+^2} \right. \\ &\quad \left. - \frac{2(\mu_-\mu_-^{q^2} + \mu_+\mu_+^{q^2})(\mu_-\mu_-^{\lambda} + \mu_+\mu_+^{\lambda})}{(\mu_-^2 + \mu_+^2)^2} \right], \end{aligned} \tag{B.91}$$

$$\begin{aligned} g''_\mu &= \frac{(g'_\mu)^2}{g_\mu} - g_\mu \left[ \frac{(\mu'_-)^2 + \mu_-\mu''_- + (\mu'_+)^2 + \mu_+\mu''_+}{\mu_-^2 + \mu_+^2} \right. \\ &\quad \left. - \frac{2(\mu_-\mu'_- + \mu_+\mu'_+)^2}{(\mu_-^2 + \mu_+^2)^2} \right]. \end{aligned} \tag{B.92}$$

The derivatives of $F(\psi, k_\mu)$ in eq. (3.20) are

$$\begin{aligned} F'(\psi, k_\mu) &= \left[ -\frac{F(\psi, k_\mu)}{2k_\mu} - \frac{E(\psi, k_\mu)}{2k_\mu(k_\mu - 1)} + \frac{\sin 2\psi}{4(k_\mu - 1)(1-\delta_2)^{1/2}} \right] k'_\mu \\ &\quad + \frac{\psi'}{(1-\delta_2)^{1/2}}, \end{aligned} \tag{B.93}$$

$$\begin{aligned} F^{q^2\lambda}(\psi, k_\mu) &= \left[ -\frac{F(\psi, k_\mu)}{2k_\mu} - \frac{E(\psi, k_\mu)}{2k_\mu(k_\mu - 1)} + \frac{\sin 2\psi}{4(k_\mu - 1)(1-\delta_2)^{1/2}} \right]^{\lambda} k_\mu^{q^2} \\ &\quad + \left[ \frac{\psi^{q^2}}{(1-\delta_2)^{1/2}} \right]^{\lambda} \\ &\quad + \left[ -\frac{F(\psi, k_\mu)}{2k_\mu} - \frac{E(\psi, k_\mu)}{2k_\mu(k_\mu - 1)} + \frac{\sin 2\psi}{4(k_\mu - 1)(1-\delta_2)^{1/2}} \right] k_\mu^{q^2\lambda}, \end{aligned} \tag{B.94}$$

$$
\begin{aligned}
F''(\psi,k_\mu) &= \left[-\frac{F(\psi,k_\mu)}{2k_\mu}-\frac{E(\psi,k_\mu)}{2k_\mu(k_\mu-1)}+\frac{\sin 2\psi}{4(k_\mu-1)(1-\delta_2)^{1/2}}\right]' k'_\mu \qquad \text{(B.95)}\\
&+\left[\frac{\psi'}{(1-\delta_2)^{1/2}}\right]'\\
&+\left[-\frac{F(\psi,k_\mu)}{2k_\mu}-\frac{E(\psi,k_\mu)}{2k_\mu(k_\mu-1)}+\frac{\sin 2\psi}{4(k_\mu-1)(1-\delta_2)^{1/2}}\right] k''_\mu,
\end{aligned}
$$

where

$$
\begin{aligned}
\left[-\frac{F(\psi,k_\mu)}{2k_\mu}-\frac{E(\psi,k_\mu)}{2k_\mu(k_\mu-1)}\right]' &= -\frac{F'(\psi,k_\mu)}{2k_\mu}-\frac{E'(\psi,k_\mu)}{2k_\mu(k_\mu-1)} \qquad \text{(B.96)}\\
&+\left[\frac{F(\psi,k_\mu)}{2k_\mu^2}+\frac{E(\psi,k_\mu)(2k_\mu-1)}{2k_\mu^2(k_\mu-1)^2}\right] k'_\mu,\\
\left[\frac{\sin 2\psi}{4(k_\mu-1)(1-\delta_2)^{1/2}}\right]' &= \frac{\psi'\cos 2\psi}{2(k_\mu-1)(1-\delta_2)^{1/2}} \qquad \text{(B.97)}\\
&-\frac{\sin 2\psi(2k'_\mu-2k'_\mu\delta_2-k_\mu\delta'_2+\delta'_2)}{8(k_\mu-1)^2(1-\delta_2)^{3/2}},
\end{aligned}
$$

$$
\begin{aligned}
\left[\frac{\psi q^2}{(1-\delta_2)^{1/2}}\right]^\lambda &= \frac{\psi q^{2\lambda}}{(1-\delta_2)^{1/2}}+\frac{\psi q^2\delta_2^\lambda}{2(1-\delta_2)^{3/2}}, \qquad \text{(B.98)}\\
\left[\frac{\psi'}{(1-\delta_2)^{1/2}}\right]' &= \frac{\psi''}{(1-\delta_2)^{1/2}}+\frac{\psi'\delta'_2}{2(1-\delta_2)^{3/2}} \qquad \text{(B.99)}
\end{aligned}
$$

and

$$
E'(\psi,k_\mu)=\frac{1}{2}\left[E(\psi,k_\mu)-F(\psi,k_\mu)\right]\frac{k'_\mu}{k_\mu}+\psi'(1-\delta_2)^{1/2}. \qquad \text{(B.100)}
$$

We determined new expressions in the derivatives above, $\delta_1$ and $\delta_2$

$$
\delta_1=\frac{\mu_{\rm o}^2(\mu_-^2+\mu_+^2)}{\mu_+^2(\mu_-^2+\mu_{\rm o}^2)}, \qquad \text{(B.101)}
$$

$$
k_\mu\delta_1=\delta_2=\frac{\mu_{\rm o}^2}{\mu_-^2+\mu_{\rm o}^2} \qquad \text{(B.102)}
$$

and their derivatives are

$$\delta_1' = 2\left[-\frac{\mu_-\mu_-'}{\mu_\mathrm{o}^2+\mu_-^2} - \frac{\mu_+'}{\mu_+} + \frac{\mu_-\mu_-' + \mu_+\mu_+'}{\mu_-^2+\mu_+^2}\right]\delta_1, \tag{B.103}$$

$$\begin{aligned}\delta_1^{q^2\lambda} = {} & \frac{\delta_1^{q^2}\delta_1^{\lambda}}{\delta_1} + 2\delta_1\left[-\frac{\mu_-^{q^2}\mu_-^{\lambda} + \mu_-\mu_-^{q^2\lambda}}{\mu_\mathrm{o}^2+\mu_-^2}\right. \\ & + \frac{2\mu_-^2\mu_-^{q^2}\mu_-^{\lambda}}{(\mu_\mathrm{o}^2+\mu_-^2)^2} - \frac{\mu_+^{q^2\lambda}}{\mu_+} + \frac{\mu_+^{q^2}\mu_+^{\lambda}}{\mu_+^2} \\ & + \frac{\mu_-^{q^2}\mu_-^{\lambda} + \mu_-\mu_-^{q^2\lambda} + \mu_+^{q^2}\mu_+^{\lambda} + \mu_+\mu_+^{q^2\lambda}}{\mu_-^2+\mu_+^2} \\ & \left. - \frac{2(\mu_-\mu_-^{q^2} + \mu_+\mu_+^{q^2})(\mu_-\mu_-^{\lambda} + \mu_+\mu_+^{\lambda})}{(\mu_-^2+\mu_+^2)^2}\right],\end{aligned} \tag{B.104}$$

$$\begin{aligned}\delta_1'' = {} & \frac{(\delta_1')^2}{\delta_1} + 2\delta_1\left[-\frac{(\mu_-')^2 + \mu_-\mu_-''}{\mu_\mathrm{o}^2+\mu_-^2} + \frac{2(\mu_-\mu_-')^2}{(\mu_\mathrm{o}^2+\mu_-^2)^2} - \frac{\mu_+''}{\mu_+} + \frac{(\mu_+')^2}{\mu_+^2}\right. \\ & \left. + \frac{(\mu_-')^2 + \mu_-\mu_-'' + (\mu_+')^2 + \mu_+\mu_+''}{\mu_-^2+\mu_+^2} - \frac{2(\mu_-\mu_-' + \mu_+\mu_+')^2}{(\mu_-^2+\mu_+^2)^2}\right]\end{aligned} \tag{B.105}$$

and

$$\delta_2' = 2\frac{\mu_-\mu_-'}{\mu_-^2+\mu_\mathrm{o}^2}\delta_2 = k_\mu'\delta_1 + k_\mu\delta_1'. \tag{B.106}$$

The derivatives of arguments in $F(\varphi_\mathrm{e}, k_r)$ are

$$k_\mu' = 2\left[\frac{\mu_+'}{\mu_+} - \frac{\mu_-\mu_-' + \mu_+\mu_+'}{\mu_+^2+\mu_-^2}\right]k_\mu, \tag{B.107}$$

$$\begin{aligned}k_\mu^{q^2\lambda} = {} & \frac{k_\mu^{q^2}k_\mu^{\lambda}}{k_\mu} + 2k_\mu\left[\frac{\mu_+^{q^2\lambda}}{\mu_+} - \frac{\mu_+^{q^2}\mu_+^{\lambda}}{\mu_+^2}\right. \\ & - \frac{\mu_-^{q^2}\mu_-^{\lambda} + \mu_-\mu_-^{q^2\lambda} + \mu_+^{q^2}\mu_+^{\lambda} + \mu_+\mu_+^{q^2\lambda}}{\mu_-^2+\mu_+^2} \\ & \left. + \frac{2(\mu_-\mu_-^{q^2} + \mu_+\mu_+^{q^2})(\mu_-\mu_-^{\lambda} + \mu_+\mu_+^{\lambda})}{(\mu_-^2+\mu_+^2)^2}\right],\end{aligned} \tag{B.108}$$

$$\begin{aligned}k_\mu'' = {} & \frac{(k_\mu')^2}{k_\mu} + 2k_\mu\left[\frac{\mu_+''}{\mu_+} - \frac{(\mu_+')^2}{\mu_+^2}\right. \\ & \left. - \frac{(\mu_-')^2 + \mu_-\mu_-'' + (\mu_+')^2 + \mu_+\mu_+''}{\mu_-^2+\mu_+^2} + \frac{2(\mu_-\mu_-' + \mu_+\mu_+')^2}{(\mu_-^2+\mu_+^2)^2}\right]\end{aligned} \tag{B.109}$$

and

$$\psi' = \frac{\delta_1'}{2\left[\delta_1(1-\delta_1)\right]^{1/2}}, \tag{B.110}$$

$$\psi^{q^2\lambda} = \frac{\delta_1^{q^2\lambda}}{2\left[\delta_1(1-\delta_1)\right]^{1/2}} - \frac{\delta_1^{q^2}\delta_1^{\lambda}(1-2\delta_1)}{4\left[\delta_1(1-\delta_1)\right]^{3/2}}. \tag{B.111}$$

$$\psi'' = \frac{\delta_1''}{2\left[\delta_1(1-\delta_1)\right]^{1/2}} - \frac{(\delta_1')^2(1-2\delta_1)}{4\left[\delta_1(1-\delta_1)\right]^{3/2}}. \tag{B.112}$$

The derivatives of $K(k_\mu)$ in eq. (3.20) are

$$K'(k_\mu) = \frac{1}{2}\left[\frac{E(k_\mu)}{k_\mu(1-k_\mu)} - \frac{K(k_\mu)}{k_\mu}\right]k_\mu', \tag{B.113}$$

$$\begin{aligned} K^{q^2\lambda}(k_\mu) &= \frac{1}{2}\left[\frac{E^{\lambda}(k_\mu)}{k_\mu(1-k_\mu)} - \frac{K^{\lambda}(k_\mu)}{k_\mu} - \frac{E(k_\mu)(1-2k_\mu)}{k_\mu^2(1-k_\mu)^2}k_\mu^{\lambda}\right. \\ &\quad \left. + \frac{K(k_\mu)}{k_\mu^2}k_\mu^{\lambda}\right]k_\mu^{q^2} + K^{q^2}(k_\mu)\frac{k_\mu^{q^2\lambda}}{k_\mu^{q^2}}, \end{aligned} \tag{B.114}$$

$$\begin{aligned} K''(k_\mu) &= \frac{1}{2}\left[\frac{E'(k_\mu)}{k_\mu(1-k_\mu)} - \frac{K'(k_\mu)}{k_\mu} - \frac{E(k_\mu)(1-2k_\mu)}{k_\mu^2(1-k_\mu)^2}k_\mu'\right. \\ &\quad \left. + \frac{K(k_\mu)}{k_\mu^2}k_\mu'\right]k_\mu' + K'(k_\mu)\frac{k_\mu''}{k_\mu'}. \end{aligned} \tag{B.115}$$

# Bibliography


Abramowicz M. A., Jaroszyński M., Kato S., Lasota J.-P., Różańska A., Sadowski A. (2010). Leaving the innermost stable circular orbit: the inner edge of a black-hole accretion disk at various luminosities. *A&A*, **521**, A15.

Abramowitz M., Stegun I. A. (1965). *Handbook of Mathematical Functions*. Dover, New York.

Agol E. & Krolik J. H. (2000). Magnetic Stress at the Marginally Stable Orbit: Altered Disk Structure, Radiation, and Black Hole Spin Evolution. *ApJ*, **528**, 161.

Artymowicz P., Lin D. N. C., Wampler E. J. (1993). Star trapping and metallicity enrichment in quasars and active galactic nuclei. *ApJ*, **409**, 592.

Bade N., Komossa S., Dahlem M. (1996). Detection of an extremely soft X-ray outburst in the HII-like nucleus of NGC 5905. *A&A*, **309**, L35.

Ballantyne D. R., McDuffie J. R., Rusin J. S. (2011). A Correlation between the Ionization State of the Inner Accretion Disk and the Eddington Ratio of Active Galactic Nuclei. *ApJ*, **734**, id. 112.

Bao G., Wiita P. J., Hadrava P. (1996). Energy-Dependent Polarization Variability as a Black Hole Signature. *Phys. Rev. Lett.*, **77**, 1215.

Bardeen J. M., Press W. H. & Teukolsky S. A. (1972). Rotating Black Holes: Locally Nonrotating Frames, Energy Extraction, and Scalar Synchrotron Radiation. *ApJ*, **178**, 347.

Beckwith K. & Done C. (2004). Iron line profiles in strong gravity. *MNRAS*, **352**, 353.

Beckwith K., Hawley J. F., Krolik J. H. (2008). Where is the radiation edge in magnetized black hole accretion discs? *ApJ*, **390**, 21.

Bloom J. S., Giannois D., Metzger B. D. et al. (2011). A Possible Relativistic Jetted Outburst from a Massive Black Hole Fed by a Tidally Disrupted Star. *Science*, **333**, 203.

Bolton C. T. (1972). Cygnus X-1 - Dimensions of the system. *Nature*, **240**, 124.

Boyer R. H. & Lindquist R. W. (1967). Maximal Analytic Extension of the Kerr Metric. *J. Math. Phys.*, **8**, 265.

Brenneman L. W. & Reynolds C. S. (2006). Constraining Black Hole Spin via X-Ray Spectroscopy. *ApJ*, **652**, 1028.

Burrows D. N., Kennea J. A., Ghisellini G. et al. (2011). Relativistic jet activity from the tidal disruption of a star by a massive black hole. *Nature*, **476**, 421.

Byrd P. F., Friedman M. D. (1971). *Handbook of Elliptic Integrals for Engineers and Scientists*. Springer-Verlag, New York.

Čadež A., Fanton C., Calvani M. (1998). Line emission from accretion discs around black holes: the analytic approach. *New Astronomy*, **3**, 647.

Čadež A., Calvani M., di Giacomo C., Marziani P. (2000). On the radial dependence of the disk FeKalpha line emissivity in active galactic nuclei. *New Astronomy*, **5**, 69.

Campana R., Feroci M., Del Monte E. et al. (2012). The LOFT (Large Observatory for X-ray Timing) background simulations. *Proceedings of SPIE*, **8443**. arXiv:1209.1661.

Carter B. (1968). Global Structure of the Kerr Family of Gravitational Fields. *Phys. Rev.*, **174**, 1559.

Cenko S. B., Krimm H. A., Horesh A. et al. (2012). Swift J2058.4+0516: Discovery of a Possible Second Relativistic Tidal Disruption Flare? *ApJ*, **753**, 77.

Chandrasekhar S. (2004). Kerr Metric. In *The Mathematical Theory of Black Holes*, from p. 273. Oxford University Press, Oxford.

Connors P. A., Piran T., Stark R. F. (1980). Polarization features of X-ray radiation emitted near black holes. *ApJ*, **235**, 224.

Coppi B., & Rousseau F. (2006). Plasma Disks and Rings with "High" Magnetic Energy Densities. *ApJ*, **641**, 458.

Cuadra J., Armitage P. J., Alexander R. D., Begelman M. C. (2009). Massive black hole binary mergers within subparsec scale gas discs. *MNRAS*, **393**, 1423.

Cunningham C. T., & Bardeen J. M. (1973). The Optical Appearance of a Star Orbiting an Extreme Kerr Black Hole. *ApJ*, **183**, 273.

Czerny B., Różańska A., Dovčiak M., Karas V., Dumont A.-M. (2004). The structure and radiation spectra of illuminated accretion disks in AGN. II. Flare/spot model of X-ray variability. *A&A*, **420**, 1.

de La Calle Pérez I., Longinotti A. L., Guainazzi M., Bianchi S., Dovčiak M. et al. (2010). FERO: Finding extreme relativistic objects. I. Statistics of relativistic Fe K$\alpha$ lines in radio-quiet Type 1 AGN. *A&A*, **524**, A50.

de Marco B., Iwasawa K., Cappi M., Dadina M., Tombesi F. et al. (2009). Probing variability patterns of the Fe K line complex in bright nearby AGNs. *A&A*, **507**, 159.

Dovčiak M., Karas V., Yaqoob T. (2004a). An Extended Scheme for Fitting X-Ray Data with Accretion Disk Spectra in the Strong Gravity Regime. *ApJSS*, **153**, 205.

Dovčiak M., Karas V., Matt G. (2004b). Polarization signatures of strong gravity in active galactic nuclei accretion discs. *MNRAS*, **355**, 1005.

Dovčiak M., Muleri F., Goosmann R. W., Karas V., Matt G. (2008). Thermal disc emission from a rotating black hole: X-ray polarization signatures. *MNRAS*, **391**, 32.

Esquej P., Saxton R. D., Freyberg M. J. et al. (2007). Candidate tidal disruption events from the XMM-Newton slew survey. *A&A*, **462**, L49.

Fabian A. C., Rees M. J., Stella L., White N. E. (1989). X-ray fluorescence from the inner disc in Cygnus X-1. *MNRAS*, **238**, 729.

Fabian A. C., Iwasawa K., Reynolds C. S., Young A. J. (2000). Broad Iron Lines in Active Galactic Nuclei. *PASP*, **112**, 1145.

Fabian A. C., Vaughan S., Nandra K., Iwasawa K., Ballantyne D. R. et al. (2002). A long hard look at MCG-6-30-15 with XMM-Newton. *MNRAS*, **335**, L1.

Fabian C. & Vaughan S. (2003). The iron line in MCG-6-30-15 from XMM-Newton: evidence for gravitational light bending? *MNRAS*, **340**, L28.

Fabian A. C., Pounds K. A., Blandford R. D. (2004). *Frontiers of X-Ray Astronomy*. Cambridge University Press, Cambridge.

Fanton C., Calvani M., de Felice F., Čadež A. (1997). Detecting Accretion Disks in Active Galactic Nuclei. *PASJ*, **49**, 159.

Feroci M., Costa E., Soffitta P. et al. (2007). SuperAGILE: the hard X-ray Imager for the AGILE space mission. *Nuclear Instruments and Methods in Physics Research A*, **581**, 728.

Feroci M., Stella L., Vacchi A., Labanti C., Rapisarda M. et al. (2010). LOFT - a Large Observatory For x-ray Timing. *Proc. SPIE*, **7732-66** (arXiv:1008.1009).

Feroci M. and the LOFT Consortium (2012). The Large Observatory for X-ray Timing (LOFT). *Experimental Astronomy*, **34**, 415.

Fuerst S. W., Wu Kinwah (2007). Line emission from optically thick relativistic accretion tori. *A&A*, **474**, 55.

Fukumura K. & Kazanas D. (2008). Light Echoes in Kerr Geometry: A Source of High-Frequency QPOs from Random X-Ray Bursts. *ApJ*, **679**, 1413.

Galeev A. A., Rosner R., Vaiana G. S. (1979). Structured coronae of accretion disks. *ApJ*, **229**, 318.

Gezari S., Martin D. C., Milliard B., Basa S., Halpern J. P. et al. (2006). Ultraviolet Detection of the Tidal Disruption of a Star by a Supermassive Black Hole. *ApJ*, **653**, L25.

Gezari S., Basa S., Martin D. C. et al. (2008). UV/Optical Detections of Candidate Tidal Disruption Events by GALEX and CFHTLS. *ApJ*, **676**, 944.

Gezari S., Chornock R., Rest A. et al. (2012). An ultraviolet-optical flare from the tidal disruption of a helium-rich stellar core. *Nature*, **485**, 217.

Guainazzi M., Matt G., Molendi S., Orr A., Fiore F. (1999). BeppoSAX confirms extreme relativistic effects in the X-ray spectrum of MCG-6-30-15. *A&A*, **341**, L27.

Guainazzi M. (2003). The history of the iron K$\alpha$ line profile in the Piccinotti AGN ESO 198-G24. *A&A*, **401**, 903.

Goosmann R. W., Mouchet M., Czerny B., Dovčiak M., Karas V., Różańska A., Dumont A.-M. (2007). Iron lines from transient and persisting hot spots on AGN accretion disks. *A&A*, **475**, 155.

Gradshteyn I. S., Ryzhik I. M. (1971). *Tables of integrals, sums, series and products, 5th edition*. Nauka, Moscow.

Haardt F. & Maraschi L. (1991). A two-phase model for the X-ray emision from Seyfert galaxies. *ApJ*, **380**, 51.

Haardt F., Maraschi L., Ghisellini G. (1994). A model for X-ray and ultraviolet emission from Seyfert galaxies and galactic black holes. *ApJ*, **432**, 95.

Hartnoll S. A., Blackmann E. G. (2001). Iron line profiles from black hole accretion discs with spiral velocity structure. *MNRAS*, **332**, L1.

Hills J. G. (1975). Possible power source of Seyfert galaxies and QSOs. *Nature*, **254**, 295.

Iwasawa K., Fabian A. C., Reynolds C. S., Nandra K., Otani C. et al. (1996). The variable iron K emission line in MCG-6-30-15. *MNRAS*, **282**, 1038.

Karas V., Vokrouhlický D., Polnarev A. G. (1992). In the vicinity of a rotating black hole - A fast numerical code for computing observational effects. *MNRAS*, **259**, 569.

Karas V., Czerny B., Abrassart A., Abramowicz M. A. (2000). A cloud model of active galactic nuclei: the iron K$\alpha$ line diagnostics. *MNRAS*, **318**, 547.

Karas V. & Šubr L. (2001). Orbital decay of satellites crossing an accretion disc. *A&A*, **376**, 686.

Karas V., Huré J.-M., Semerák O. (2004). TOPICAL REVIEW: Gravitating discs around black holes. *Classical and Quantum Gravity*, **21**, R1.

Karas V. (2006). Theoretical aspects of relativistic spectral features. *Astronomische Nachrichten*, **327**, 961.

Karas V. & Sochora V. (2010). Extremal Energy Shifts of Radiation from a Ring Near a Rotating Black Hole. *ApJ*, **725**, 1507.

Kato S., Fujue J., Mineshige S. (1998). *Black-Hole Accretion Disks*. Kyoto University Press, Kyoto.

Kerr R. P. (1963). Gravitational Field of a Spinning Mass as an Example of Algebraically Special Metric. *Phys. Rev. Lett.*, **11**, 237.

King A. R., Pringle J. E. (2006). Growing supermassive black holes by chaotic accretion. *MNRAS*, **373**, L90.

Kojima, Y. (1991). The effects of black hole rotation on line profiles from accretion discs. *MNRAS*, **250**, 629.

Laor A. (1991). Line profiles from a disk around a rotating black hole. *ApJ*, **376**, 90.

Levan A. J., Tanvir N. R., Cenko S. B. et al. (2011). An Extremely Luminous Panchromatic Outburst from the Nucleus of a Distant Galaxy. *Science*, **333**, 199.

Martocchia A., Karas V., Matt G. (2000). Effects of Kerr space-time on spectral features from X-ray illuminated accretion discs. *MNRAS*, **312**, 817.

Martocchia A., Matt G., Karas V. (2002a). On the origin of the broad, relativistic iron line of MCG-6-30-15 observed by XMM-Newton. *A&A*, **383**, 23.

Martocchia A., Matt G., Karas V., Belloni T., Feroci M. (2002b). Evidence for a relativistic iron line in GRS 1915+105. *A&A*, **387**, 215.

Matt G., Perola G. C., Stella L. (1993). Multiple-peaked line profiles from relativistic disks at high inclination angles. *A&A*, **267**, 643.

McClintock J. E., Remillard R. A. (2006). *Compact Stellar X-ray Sources*, eds. W. Lewin & M. van der Klis, p. 157–213. Cambridge University Press, Cambridge.

Miller J. M., Fabian A. C., Wijnands R., Remillard R. A., Wojdowski P. et al. (2002). Resolving the Composite Fe K$\alpha$ Emission Line in the Galactic Black Hole Cygnus X-1 with Chandra. *ApJ*, **578**, 348.

Miller J. M. (2007). Relativistic X-Ray Lines from the Inner Accretion Disks Around Black Holes. *ARA&A*, **45**, 441.

Miller L., Turner T. J., Reeves J. N. (2009). The absorption-dominated model for the X-ray spectra of typeI active galaxies: MCG-6-30-15. *MNRAS*, **399**, L69.

Misner C. W., Thorne K. S., Wheeler J. A. (1973). *Gravitation*. W. H. Freeman & Co, New York.

Murphy K. D., Yaqoob T., Karas V., Dovčiak M. (2009). On the Prospect of Constraining Black Hole Spin Through X-ray Spectroscopy of Hotspots. *ApJ*, **701**, 635.

Nandra K., O'Neill P. M., George I M., Reeves J. N. (2007). An XMM-Newton survey of broad iron lines in Seyfert galaxies. *MNRAS*, **382**, 194.

Nandra K., Barret D., Barcons X. at al. (2013). The Hot and Energetic Universe: A White Paper presenting the science theme motivating the Athena+ mission. arXiv:1306.2307.

Noble S. C., Krolik J. H., Hawley J. F. (2009). Direct Calculation of the Radiative Efficiency of an Accretion Disk Around a Black Hole. *ApJ*, **692**, 411.

Novikov I. D., Thorne K. S. (1973). In *Black Holes*, p. 343. Gordon and Breach Publishers, New York.

Page D. N. & Thorne K. S. (1974). Disk-Accretion onto a Black Hole. Time-Averaged Structure of Accretion Disk. *ApJ*, **499**, 191.

Pariev V. I., Bromley B. C., Miller W. A. (2001). Estimation of Relativistic Accretion Disk Parameters From Iron Line Emission. *ApJ*, **547**, 649.

Pecháček T., Karas V., Czerny B. (2008). Hot-spot model for accretion disc variability as random process. *A&A*, **487**, 815.

Ponti G., Cappi M., Dadina M., Malaguti G. (2004). Mapping the inner regions of MCG-6-30-15 with XMM-Newton. *A&A*, **417**, 451.

Press W. H., Teukolsky S. A., Vetterling W. T., Flannerry B. P. (2007). In *Numerical Recipes, 3rd edition*, p. 309 and 456. Cambridge University Press, Cambridge.

Rauch K. P. & Blandford R. D. (1994). Optical Caustics in a Kerr Spacetime and the Origin of Rapid X-Ray Variability in Active Galactic Nuclei. *ApJ*, **421**, 46.

Rees M. J. (1988). Tidal disruption of stars by black holes of 10 to the 6th-10 to the 8th solar masses in nearby galaxies. *Nature*, **333**, 523.

Reynolds C. S. (1996). Ph.D. thesis, Univ. of Cambridge.

Reynolds C. S. & Begelman M. C. (1997). Iron Fluorescence from within the Innermost Stable Orbit of Black Hole Accretion Disks. *ApJ*, **488**, 109.

Reynolds C. S. & Nowak M. A. (2003). Fluorescent iron lines as a probe of astrophysical black hole systems. *Phys. Rep.*, **377**, 389.

Reynolds C. S. & Fabian A. C. (2008). Broad Iron-K$\alpha$ Emission Lines as a Diagnostic of Black Hole Spin. *ApJ*, **675**, 1048.

Schee J., Stuchlík Z., Jurán J. (2005). Light escape cones and raytracing in Kerr geometry. *Proceedings of RAGtime 6/7: Workshops on black holes and neutron stars*. Silesian University in Opava, Opava.

Schnittman J., Krolik J. H., Hawley J. F. (2006). Light Curves from an MHD Simulation of a Black Hole Accretion Disk. *ApJ*, **651**, 1031.

Shapiro S. L., Teukolsky S. A. (1983). *Black Holes, White Dwarfs, and Neutron Stars*. John Wiley & Sons, Inc, USA.

Silantev N. A. & Gnedin Y. N. (2008). Polarization of radiation of point-like source reflected from turbulent magnetized atmosphere. *A&A*, **481**, 217.

Sochora V. & Karas V. (2010a). Extremal Energy Shifts from a Radiating Ring near a Rotating Black Hole. *Proceedings of the 19th Annual Conference of Doctoral Students, Part III - Physics*. MATFYZPRESS, Prague.

Sochora V. & Karas V. (2010b). Energy shifts of spectral lines from accretion discs near a black hole with negative spin. *Proceedings of the 25th Texas Symposium on Relativistic Astrophysics*. Published online.

Sochora V., Karas V., Svoboda J., Dovčiak M. (2011). Black hole accretion rings revealed by future X-ray spectroscopy. *MNRAS*, **418**, 276.

Steiner J. F., Reis R. C., McClintock J. E., Narayan R., Remillard R. A. et al. (2010). The spin of the black hole microquasar XTE J1550-564 via the continuum-fitting and Fe-line methods. *MNRAS*, **416**, 941.

Svoboda J., Guainazzi M., Karas V. (2010). Warm absorber and truncated accretion disc in IRAS 05078+1626. *A&A*, **512**, A62.

Tagger P. & Varnière P. (2006). Accretion-Ejection Instability, MHD Rossby Wave Instability, Diskoseismology, and the High-Frequency QPOs of Microquasars. *ApJ*, **652**, 1457.

Tanaka Y., Nandra K., Fabian A. C., Inoue H., Otani C. et al. (1995). Gravitationally redshifted emission implying an accretion disk and massive black hole in the active galaxy MCG-6-30-15. *Nature*, **375**, 659.

Thorne K. S. & Price R. H. (1975). Cygnus X-1 - an interpretation of the spectrum and its variability. *ApJ*, **195**, 101.

Turner T. J., Miller L., George I. M., Reeves J. N. (2006). Evidence for orbital motion of material close to the central black hole of Mrk 766. *A&A*, **445**, 59.

Turner T. J., Miller L., Reeves J. N., Lobban A., Braito V., Kraemer S. B., Crenshaw D. M. (2010). Significant X-ray Line Emission in the 5-6 keV Band of NGC 4051. *ApJ*, **712**, 209.

Urry C. M. & Padovani P. (1995). Unified Schemes for Radio-Loud Active Galactic Nuclei. *PASP*, **107**, 803.

Uzdensky D. A. & Goodman J. (2008). Statistical Description of a Magnetized Corona above a Turbulent Accretion Disk. *ApJ*, **682**, 608.

Wang J.-M., Zhou Y.-Y., Yuan Y.-F., Cao X., Wu M. (2000). Profile of an Emission Line from Relativistic Outflows around a Black Hole. *ApJ*, **544**, 381.

Webster B. L. & Murdin P. (1972). Cygnus X-1 - a Spectroscopic Binary with a Heavy Companion? *Nature*, **235**, 37.

Wellin P. R., Gaylord R. J., Kamin S. N. (2005). *An Introduction to Programming with Mathematica*. Cambridge University Press, Cambridge.

Wilkins D. R. & Fabian A. C. (2011). Determination of the X-ray reflection emissivity profile of 1H 0707-495. *MNRAS*, **414**, 1269.

Wilms J., Reynolds C. S., Begelman M. C., Reeves J., Molendi S. et al. (2001). XMM-EPIC observation of MCG-6-30-15: direct evidence for the extraction of energy from a spinning black hole? *MNRAS*, **328**, L27.

Young P. J., Shields G. A., Wheeler J. C. (1977). The black tide model of QSOs. *ApJ*, **212**, 367.

Zakharov A. F., Ma Z., Bao Y. (2004). The iron K$\alpha$ lines as a tool for magnetic field estimations in non-flat accretion flows. *New Astronomy*, **9**, 663.

# List of author's publications

## Publications in refereed journals

Sochora V., Karas V., Svoboda J., Dovčiak M. (2011). Black hole accretion rings revealed by future X-ray spectroscopy. *MNRAS*, **418**, 276.

Karas V. & Sochora V. (2010). Extremal Energy Shifts of Radiation from a Ring Near a Rotating Black Hole. *ApJ*, **725**, 1507.

## Publications in conference proceedings

Sochora V., Karas V., Svoboda J., Dovčiak M. (2013). Beyond the standard model of the disc-line spectral profiles from black hole accretion discs. *Proceedings of 10th INTEGRAL/BART Workshop*, submitted.

Feroci M., ..., Sochora V. et al. (2012). LOFT: the Large Observatory For X-ray Timing. *Space Telescopes and Instrumentation 2012: Ultraviolet to Gamma Ray. Proceedings of the SPIE*, **8443**, article id. 84432D, 16 pp.

Sochora V. & Karas V. (2010). Energy shifts of spectral lines from accretion discs near a black hole with negative spin. *Proceedings of the 25th Texas Symposium on Relativistic Astrophysics.*
Published online, http://pos.sissa.it/cgi-bin/reader/conf.cgi?confid=123.

Sochora V. & Karas V. (2010). Extremal Energy Shifts from a Radiating Ring near a Rotating Black Hole. *Proceedings of the 19th Annual Conference of Doctoral Students, Part III - Physics.* MATFYZPRESS, Prague.